Analysis of Hydrokinetic Turbines in Open Channel Flows

Arshiya Hoseyni Chime

A thesis submitted in partial fulfillment of the requirements for the degree of

Master of Science in Mechanical Engineering

University of Washington

2013

Committee:

Philip C. Malte
James J. Riley
Igor V. Novosselov

Program Authorized to Offer Degree:
Department of Mechanical Engineering

Table of Contents

List of Figures

List of Tables

Chapter 1
Introduction

1.1 Background

The latest US Geological Survey shows that about 410,000 million gallons per day of water was withdrawn for use in the United States in 2005 (the next survey will be published in 2014) [1]. Thermoelectric power and irrigation attributed to the largest withdrawals. Water withdrawal in California, Texas, Idaho, and Florida accounted for one-forth of the net water withdrawn in 2005. Figure 1.1 shows the total water withdrawals of each state in 2005 colored by the different water-usage categories.

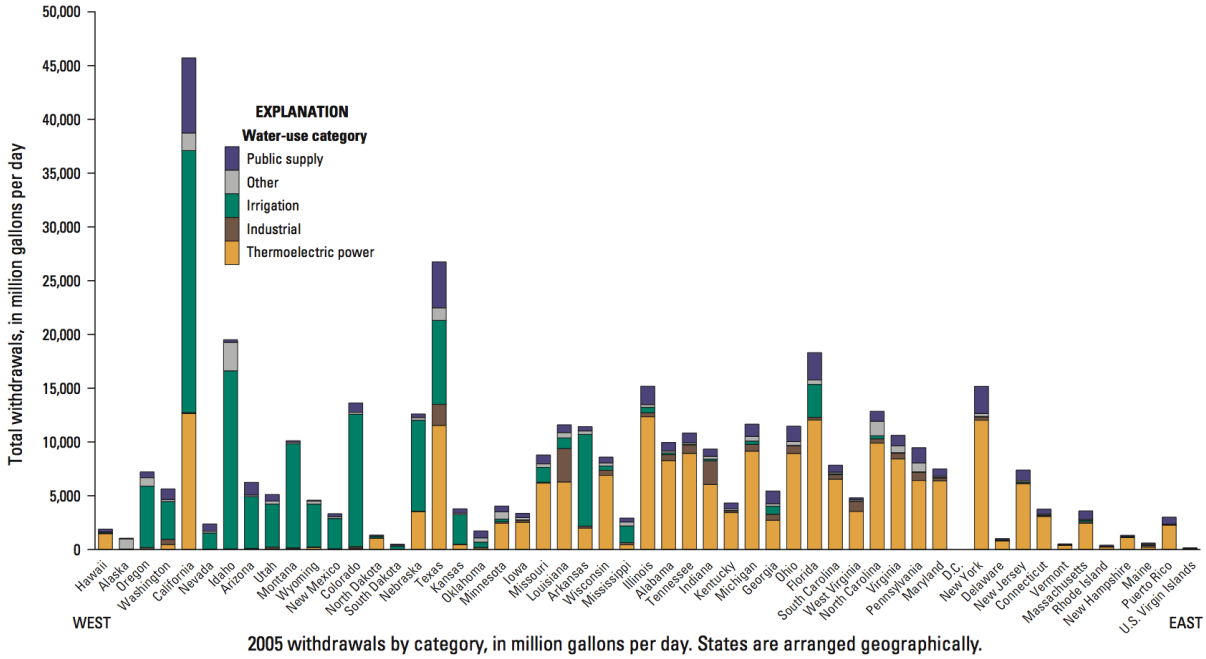

Figure 1.1- Total water withdrawals of each state in 2005 based on water-usage category [1].

This plot shows the extent to which water is moved within the US and the importance of waterways on power generation and farming. Water is moved mostly for irrigation

purposes in the western US and for thermoelectric power plants in the eastern US. About 80% of the total water withdrawal is from surface water, which is referred to as Open Channel Flows in literature. California, Idaho, and Colorado are among states that withdraw the most amounts of water for irrigation purposes. These states contain 10, 6, and 3 million acres of irrigation farmlands respectively. From an international perspective, Europe withdraws 44% of surface water for thermoelectric power plants and 21% for irrigation purposes. About 85%, 63%, and 67% of water withdrawal is mostly contributed to irrigation in Middle East, South America and East Asia respectively [2], [3], [4].

The US Bureau of Reclamation manages more than 47,000 miles of canals, laterals, drains, and tunnels according to the 2012 progress report [5]. This report identified 373 existing Bureau of Reclamation canals and conduits that have the potential of generating an additional 365,219 megawatt-hours of low-head hydropower annually in addition to energy production of the dams [5]. The low-head hydropower refers to power extraction from moving water at locations that have at least 5 feet drop and operate at least four months of the year.

The Columbia Basin Project in central Washington state is one of the largest water reclamation projects in the US, owing to the Grand Coulee hydroelectric dam. This project serves as a water source for over 671,000 acres of farms using over 6,000 miles of channels[6]. The Columbia Basin Irrigation System is formed when water is diverted from the Columbia River into the Banks Lake Reservoir at the Grand Coulee dam. The water from this reservoir is then channeled through the Dry Falls Dam and into the Main Canal. The

Main Canal then runs south before splitting between the East and West Canals near Soap Lake, Washington as shown in Figure 1.2.

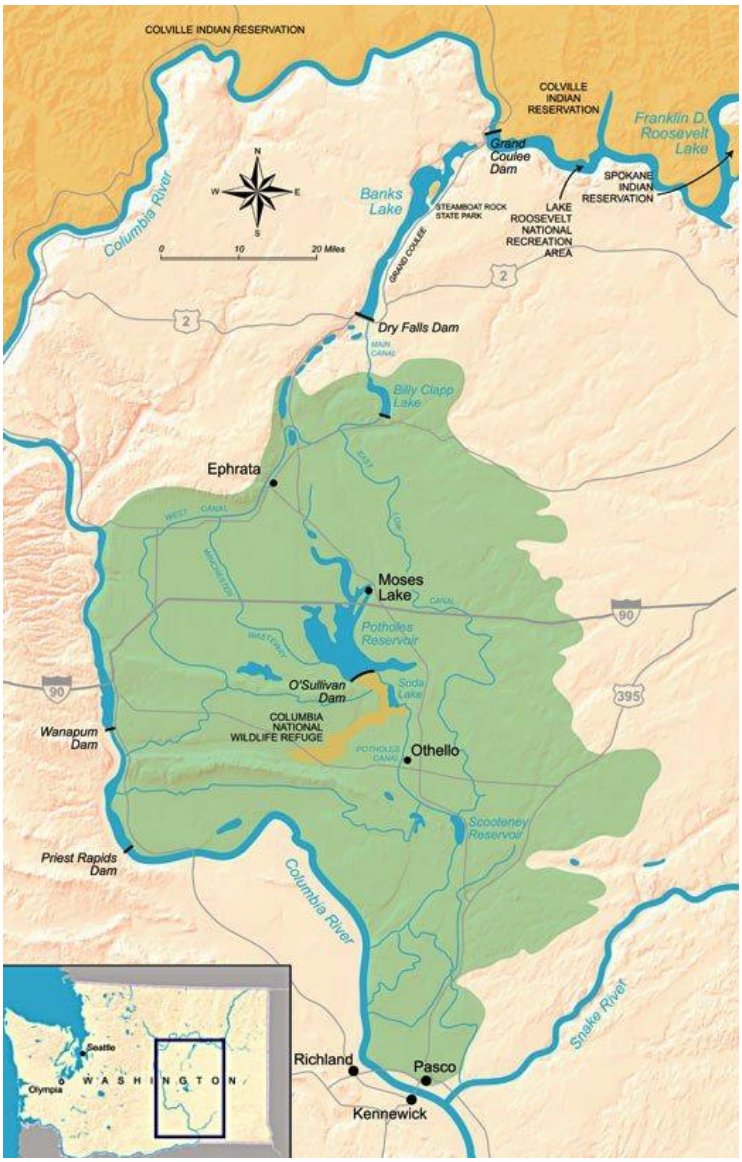

Figure 1.2- Columbia Basin Project map [6]

While most of the channels in the Columbia Basin Project consist of laterals and drainage channels that carry relatively small amounts of water, there are over 300 miles of “main” canals, which have flow rate capacities of between 3,400 cfs to 19,300 cfs [6].

In order to control the flow in such irrigation canals, traditional gates such as Sluice and Tainter gates are used to dissipate energy of the water. The main purpose of these gates is to maintain a proper flow rate by means of creating a blockage to the flow. Water flow accelerates as it passes through the restricted opening of the gate and often becomes supercritical. This unstable flow tends to transition to subcritical flow by going through a very dissipative hydraulic jump. A hydraulic jump is the abrupt change of the flow from high velocity (low depth) to a low velocity (higher depth) open channel flow. This process is accompanied by a significant head loss (energy loss) due to interaction of strong turbulent rollers with free surface leading to air entrainment, vortices, kinetic energy dissipation, and a bubbly two-phase flow structure (i.e. white water) [7].

This reduction in the energy of the flow cannot be made using low-head or conventional hydropower methods since the slope of the channel is too small at the location of most of these gates and capital cost of corresponding facilities is quite high. As a result, hydrokinetic turbines may be better options for capturing the energy of the flow. An analysis must be made to understand the amount of power that can be extracted by the turbines and the mixing loss of the slow and fast moving streams of water in the turbine wakes, in addition to analyzing the ability of such devices to control the flow.

1.2 Motivation and Objective

Taking the High Hills gates in the West Canal of the Columbia Basin Project as an example, open channel flow analysis can be performed to calculate the energy loss of the flow due to these gates. The nominal flow rate in this canal is about 5000 cfs (141 $\frac{m^3}{s}$). The cross-sectional area of the West Canal is a trapezoid with a bottom width of 16m, a height of

5.1m, and a slope ratio of 1.5:1 on the sides. The flow is controlled using three Tainter gates by raising or lowering them as shown in Figure 1.3.

Figure 1.3-High Hills gates in the West Canal located in Columbia River Irrigation District. (Photo: Courtesy of Professor Philip Malte)

An open channel flow analysis is performed and presented in Appendix A to calculate the power dissipation of flow due to blockage of the gates. Based on this analysis, as the gate opening is lowered, a hydraulic jump occurs due to supercritical flow outflowing the gate as shown in Figure 1.4. The power dissipation varies from 170 kW to about 1.67 MW. At gate opening of 2m (in the 5m deep flow), 1MW of power is dissipated from the flow due to the hydraulic jump of the flow passing through the gate.

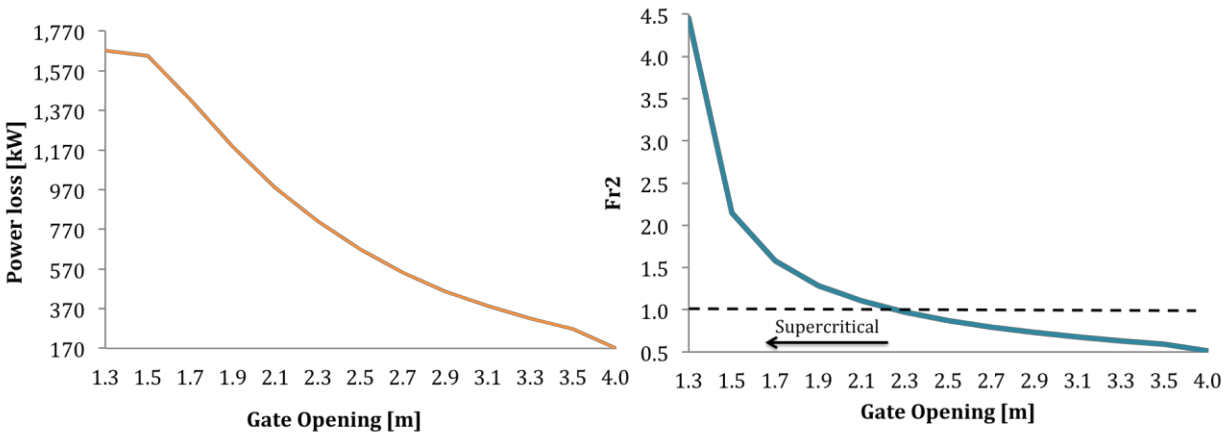

Figure 1.4- Power loss of the flow due to gates at different gate openings (left), Froude number at the minimum depth of the gate outflow at different gate openings (Right)

The dissipation of power occurs in terms of heat and interaction of strong turbulent rollers with the free surface leading to air entrainment, vortices, and a bubbly two-phase flow structure [7]. Figure 1.5 shows the top view of the section of West Canal that includes High Hills gates. The white water shown in the wake of the gates represents this bubbly two-phase flow structure with high kinetic energy loss.

Figure 1.5- Top view of the High Hills gates using Google map.

Given that this dissipated power is wasted using this traditional method, it is desirable to capture this energy. Hydrokinetic turbines are possible candidates for replacing traditional gates to not only control the flow, but also to generate power. In order to investigate this potential, three different methods are utilized in this thesis including a one-dimensional linear momentum theory, a three-dimensional Actuator Disc Model (ADM), and a Virtual Blade Model (VBM) developed in the commercial Computational Fluid Dynamic (CFD) code ANSYS Fluent. Comparison between these 3 different models is used to determine the potential of these tools in performing analysis on hydrokinetic turbines in Open Channel Flows at high blockage ratios.

Chapter 2
Literature Review

2.1 Actuator Disc Model (ADM)

A relatively simple theoretical model can be used to calculate the axial force acting on the turbine rotor. The power associated with this axial force represents the limiting (i.e., maximum) power that can be generated by the turbine. Numerical computations with the actuator disk model (ADM) can then be used to study the effect of the turbine on the flow field [8]. The theoretical ADM is based on the one-dimensional streamtube analysis of the flow as discussed in detail in Section 3.1.2. In this analysis, the turbine rotor is replaced by a force equal and opposite to the thrust, which is the force of the fluid on the turbine. Then, conservation laws are used to determine flow characteristics at desired locations. Numerical ADM relies on using CFD software to solve Reynolds-Average Navier-Stokes (RANS) equations along with additional two turbulence equations to solve for flow field. This numerical method models the turbine as a porous disk, which represents axial force inserted by the turbine on the flow or the pressure drop caused by power extraction of the turbine. This is fully explained in Section 3.2.4.2. ADM is useful where large-scale flow characteristics are of interest, such as the far wake, free surface effects, or installation of multi-turbine arrays [9].

2.1.1 One-Dimensional Theory

Power generation of hydro turbines in unconstrained channels is analogous to wind turbines. The extracted power by the turbine can be found using Equation 2.1 [10].

$$P_{extracted} = \frac{1}{2}\rho A {u_0}^3 \eta_e = \frac{1}{2}\rho A {u_0}^3\, 4a(1-a)^2 \qquad 2.1$$

Where $\eta_e = C_p$ is the extraction efficiency or power coefficient, ρ is the fluid density, A is the area, u_0 is the upstream, undisturbed speed of the flow, and a is the induction factor. Induction factor represents fractional decrease in flow velocity between free stream and turbine velocity, u_2.

$$a = 1 - \frac{u_2}{u_0} \qquad 2.2$$

Maximum power that can be extracted from an ideal turbine with no channel constraints was found by Lanchester (1915) and a few years later by Betz (1920). Based on conservation of mass and momentum on the streamtube (Control Volume 2) in Figure 2.1, maximum power is achieved when induction factor is 1/3. In this case, $\eta_{e,max}$ is 16/27 or 0.59 which means only 59% of the kinetic power of the flow with no constraint can be extracted by the turbine. The derivation for this theory can be found in [8].

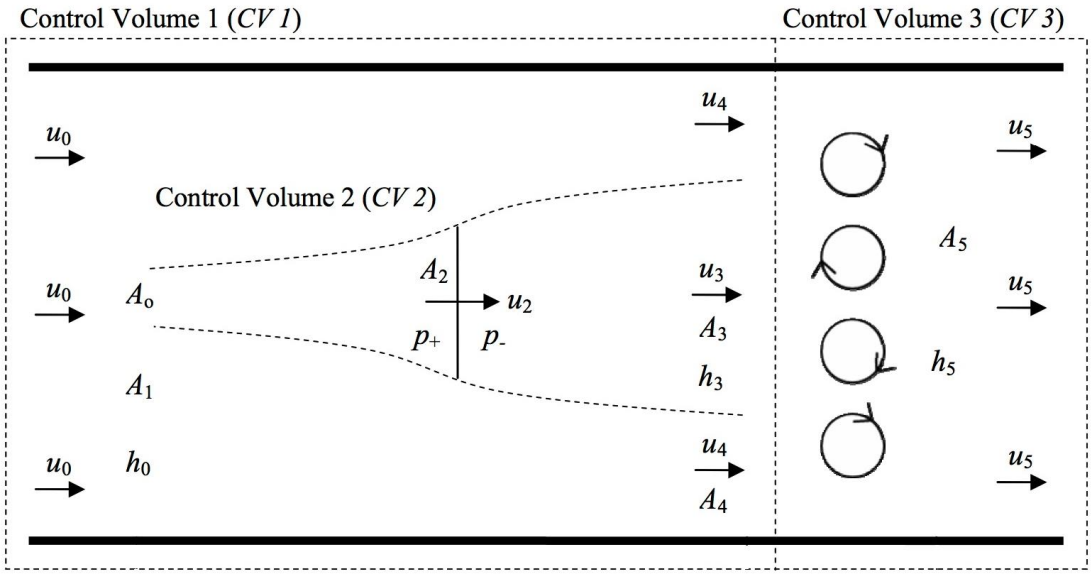

Figure 2.1- Schematic of actuator disc theory (top view)[11].

Garrett et al. [10] used control volume analysis for turbines in a constrained channel. Considering conservation of mass, momentum, and energy within CV 1, CV 2, and CV 3 in Figure 2.1, they found out that maximum efficiency of an array of turbines in confined channels is higher than the Lanchester-Betz efficiency. In this method, maximum extraction efficiency, $\eta_{e,max}$, is achieved when $\frac{u_3}{u_0} = \frac{1}{3}$ and its value is $(1-\varepsilon)^{-2}$ times greater than the Lanchester-Betz classical limit. ε is the blockage ratio and is defined as the cross-sectional area of the turbines over the cross-sectional area of the channel where discs are located at as in Equation 2.4 Based on this relation, if blockage ratio goes to zero, Equation 2.3 reduces to Lanchester-Betz limit.

$$\eta_{e,max} = \frac{16}{27}(1-\varepsilon)^{-2} \qquad 2.3$$

$$\varepsilon = \frac{A_{c,turbines}}{A_{c,channel}} \qquad 2.4$$

If turbines are operating at maximum efficiency, Corten [12]and Garrett [10]concluded that 2/3 of the total power dissipated from the flow is extracted by the turbines or in other words $\frac{P_{extracted}}{P_{dissipated}} = \frac{2}{3}$. The rest of power is dissipated into heat by means of turbulent mixing and viscous shear as heat [12], [10]. This one-dimensional model is only valid for small Froude numbers and blockage ratios. Therefore, surface deformation due to power extraction of turbines was ignored.

To address this shortcoming, Whelan et al. [13] developed a similar analysis to analyze the effects of free-surface proximity on the flow field around hydrokinetic turbines while taking into account the blockage ratio. Conservation of mass, momentum and Bernoulli equations were used for CV 1 and CV 2 in Figure 2.1 to find out velocity and depth at desired location of the channel. Combining all these equations into a quadratic polynomial which was in terms of Fr, ε, $\frac{u_3}{u_0}$, $\frac{u_4}{u_0}$. Figure 2.2 shows the method of root selection for this polynomial at certain Froude number and blockage ratio. At a given $\frac{u_3}{u_0}$, any value of $\frac{u_4}{u_0} < 1$ gives a non-physical solution since it implies flow speeding up in the wake of the turbines. It can also be seen that if normalized wake velocity reaches a certain value, in this case, 0.46, then it is possible that wake bypass reaches supercritical condition where it would have to go through a very dissipative process such as a hydraulic jump to reach downstream condition.

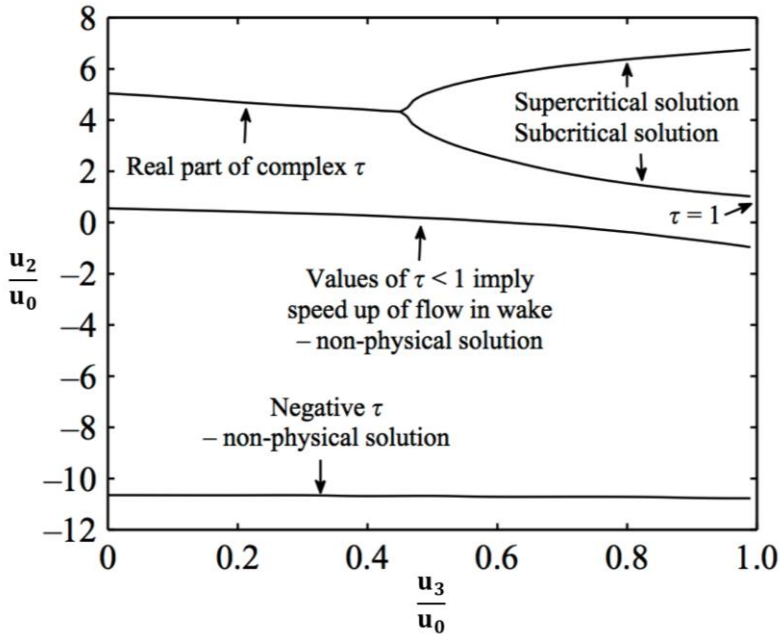

Figure 2.2- Method for root selection for the case Fr=0.14 and ε=0.64 [13]

In this analysis, extraction efficiency was solved by Whelan and was presented in Equation 2.5.

$$C_p = \eta_e = \frac{u_2}{u_0}\left[\left(\frac{u_4}{u_0}\right)^2 - \left(\frac{u_3}{u_0}\right)^2\right] \qquad 2.5$$

η_e is plotted with respect to induction factor at several blockage ratios, ε, in Figure 2.3. As blockage ratio increases, more power is expected to be extracted from the flow. Also, at a given blockage ratio, extraction efficiency is higher for flow with higher Froude number. In this graph, lines of η_e are discontinuous for $\varepsilon > 0.3$, since wake bypass flow reached supercritical condition.

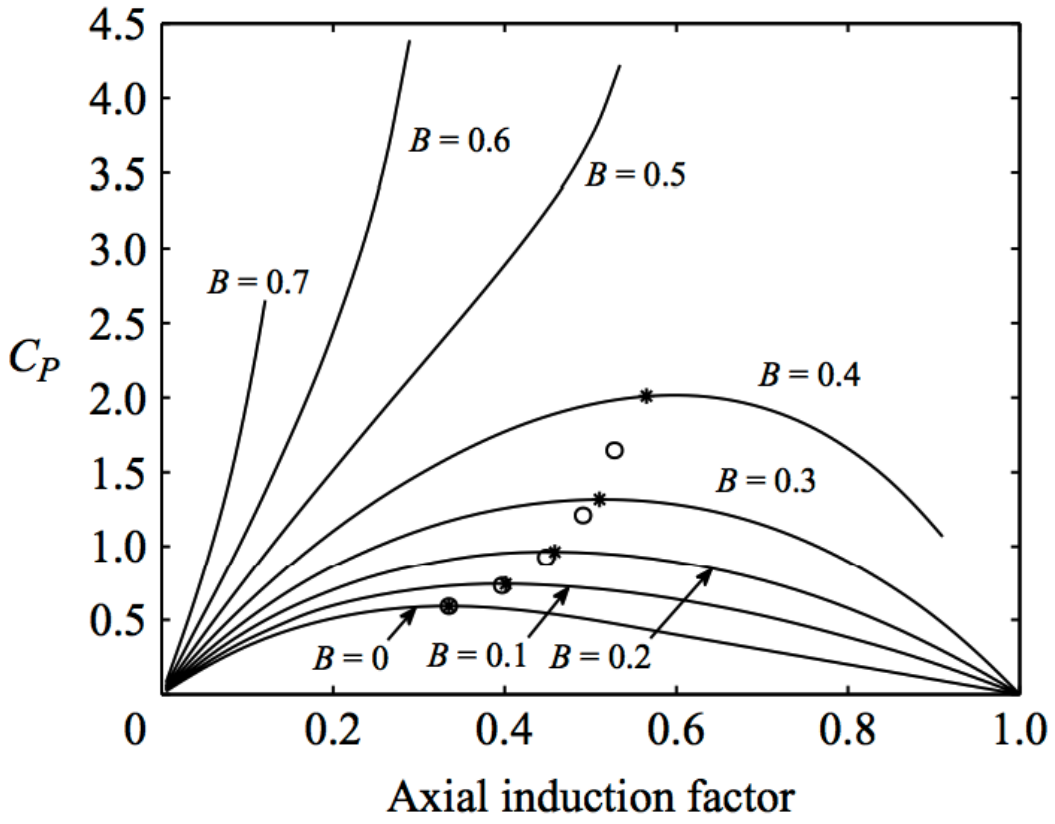

Figure 2.3- The effect of blockage ratio on extraction coefficient at Fr=0.22 (-*- denotes maxima at Fr=0.22 and –o- denotes maxima at Fr=0) where B is blockage ratio[13].

Whelan et al. [13] performed 2 sets of experiments with a 2 bladed turbine which was 0.54m in diameter with NACA 6412 airfoil with twist varying from 33.3 to 5 degrees from root to tip. This rotor was tested at a water flume with blockage ratio of 0.64 and a wind tunnel with blockage of 0.05 at several Tip Speed Ratios (TSR), which is the ratio between rotational speed of the turbine over upstream flow velocity, u_0). This is referred to as blocked and unblocked case respectively in Figure 2.4 [13]. As it was expected, higher blockage resulted in higher power coefficient. This figure also shows the maximum C_p found from one-dimensional theory mentioned above (Referred to "Inviscid max C_p" since it was assumed that fluid is ideal with no viscosity in one-dimensional analysis). It is interesting to note that in both cases ratio of maximum C_p measured over inviscid maximum C_p found by one-dimensional theory was about 60% [13].

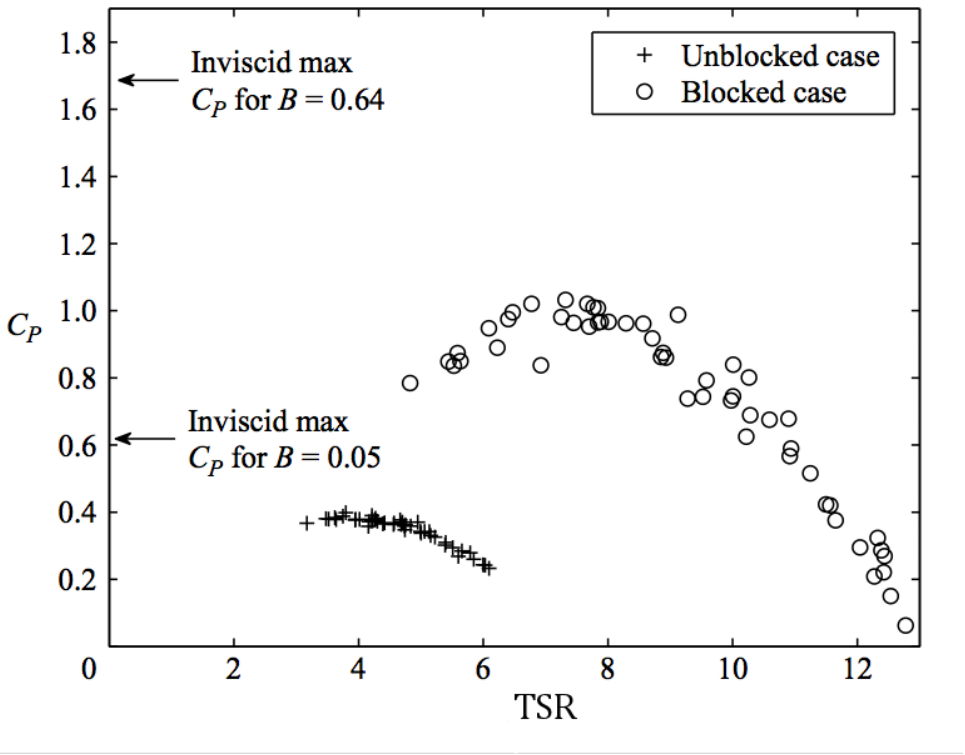

Figure 2.4- Power coefficient vs TSR for Blocked case (BR=0.64) and Unblocked case (BR=0.05) [13].

Whelan's work did not include the analysis of the mixing region. In 2009, Polagye [11] completed this analysis by including conservation of mass, momentum and energy in CV 3 and determined the ratio of extracted over dissipated power [11].

$$\frac{P_{extracted}}{P_{dissipated}} = \frac{u_2}{u_0}\left[\frac{\varepsilon\left(u_4^2 - \left(\frac{u_3}{u_0}\right)^2 u_0^2\right)}{(u_0^2 - u_5^2) + 2g(h_0 - h_5)}\right] \qquad 2.6$$

Based on this analysis, as blockage ratio is increased, higher values of extraction coefficient are found, while, more power is dissipated from the flow due to mixing of the high speed flow region with slower section in the very far wake region. This is shown in Figure 2.5

along with the effect of Froude number on extraction and dissipation coefficient. For small Fr or ε, simplified results of Garrett et al. agreed fairly well with the more detailed analysis of Polagye [11], [10].

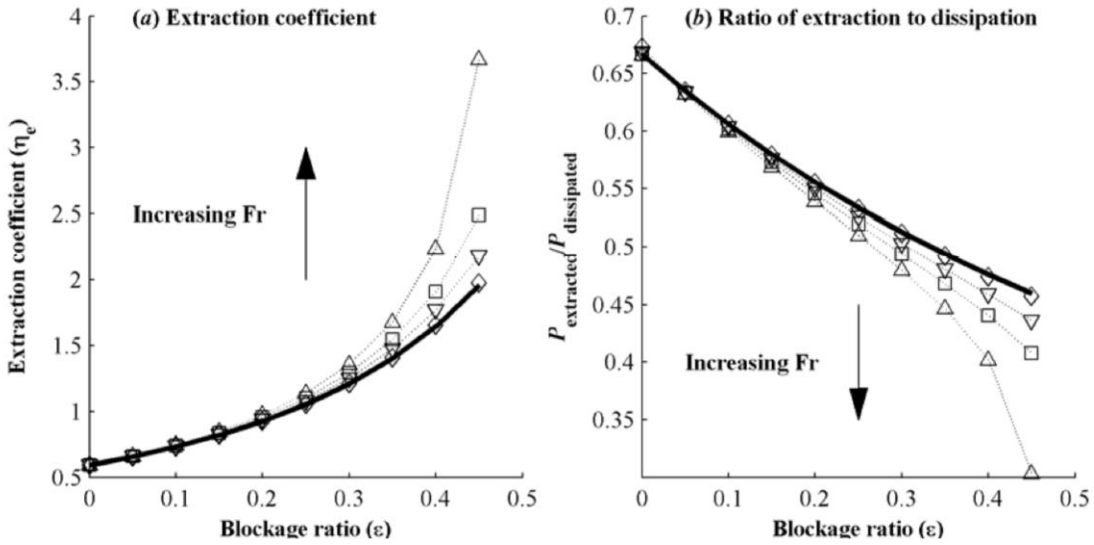

Figure 2.5-Measures of turbine performance at various blockage ratio and Froude number for turbines operating at the theoretical maximum efficiency ($\frac{u_3}{u_0} = \frac{1}{3}$). Solid lines represent Garret and Cummins' analytical result [11], [10]

2.1.2 Numerical Modeling

The numerical ADM model has widely been used to predict the performance of ship propellers or wind turbines. In this approach, Computational Fluid Dynamic (CFD) software such as Fluent and CFX are used to solve RANS equations for the flow field parameters such as pressure and velocity. The turbine is represented by a porous media of the same diameter, referred to as an actuator disc. A momentum sink term is assigned to the cells within this disc, which depends on the axial force of the turbine and consequently the resistance coefficient applied to the disc as flow passes the turbine. This momentum

term is then added to the momentum equations of the Navier-Stokes equations in the solver [9].

It is worth noting that the computational time for this model is low compared to other CFD models that include the actual blades of the rotor for the following reasons [14]:

1. ADM assumes that flow is in steady state since the disc is stationary and is not rotating.
2. The rotor is defined as a disc; therefore, no mesh refinement is needed at the rotor to capture the boundary layer and separation on the blades.

The RANS-ADM has been used in many studies. MacLeod et al. [15] performed a 3 dimensional simulation of an actuator disc in a channel to study wake effects in tidal current turbine farms. In this simulation, the free slip condition was used for the top wall (i.e., free surface was not tracked) and blockage ratio was negligible. Ambient turbulence intensity and axial force coefficient of the flow were varied in order to explore their effects on the centerline velocity deficit. Results showed that as ambient turbulence intensity increased, higher rate of wake recovery was observed. Along with this result, higher axial force resulted in lower wake velocities [15].

Harrison et al. [9] also proved that higher ambient turbulence intensities caused the wake to dissipate faster. They simulated an actuator disc in a channel using the commercial CFD code, Ansys CFX 11, and used experimental work done by Bahaj [16] to validate the numerical simulations. In this numerical analysis, the free surface was tracked using the Volume of Fluid (VOF) model and momentum sink was found from Equation2.7.

$$Momentum\ Sink = \frac{\mathrm{K}}{\Delta \mathrm{x}} \frac{\rho}{2} U_d^2 \qquad 2.7$$

Where $\frac{\mathrm{K}}{\Delta \mathrm{x}}$ is the resistance coefficient (where unit is $\frac{1}{\mathrm{m}}$), which is a function of the pressure drop across the disc and consequently the axial force coefficient of the actuator disc, C_t. This model utilized the $k-\omega$ SST (Sear Stress Transport) model along with RANS mass and momentum equations to solve for the flow field.

The experimental work [16] and [17] used the gravity fed flume at University of Southampton where a disc with drilled holes was inserted in the flow to represent the actuator disk. Axial force was measured using a load cell and velocity was recorded at several locations downstream of the disc using an Acoustic Doppler Velocimeter (ADV). Both numerical and experimental results confirmed that the near wake region (distance less than 5 diameter behind the disc) is most affected by changing the axial force coefficient (or porosity of the disc). As shown in Figure 2.6, as resistance of the disc was increased, the more the flow diverted around it, rather than going through. Based on conservation of mass, the wake must expand further when the initial velocity behind the disc is lower. This caused velocity of the flow passing through the disc to slow down (higher velocity deficit in near wake region). Therefore, expansion of the wake entrained energy more quickly and therefore the near wake became shorter.

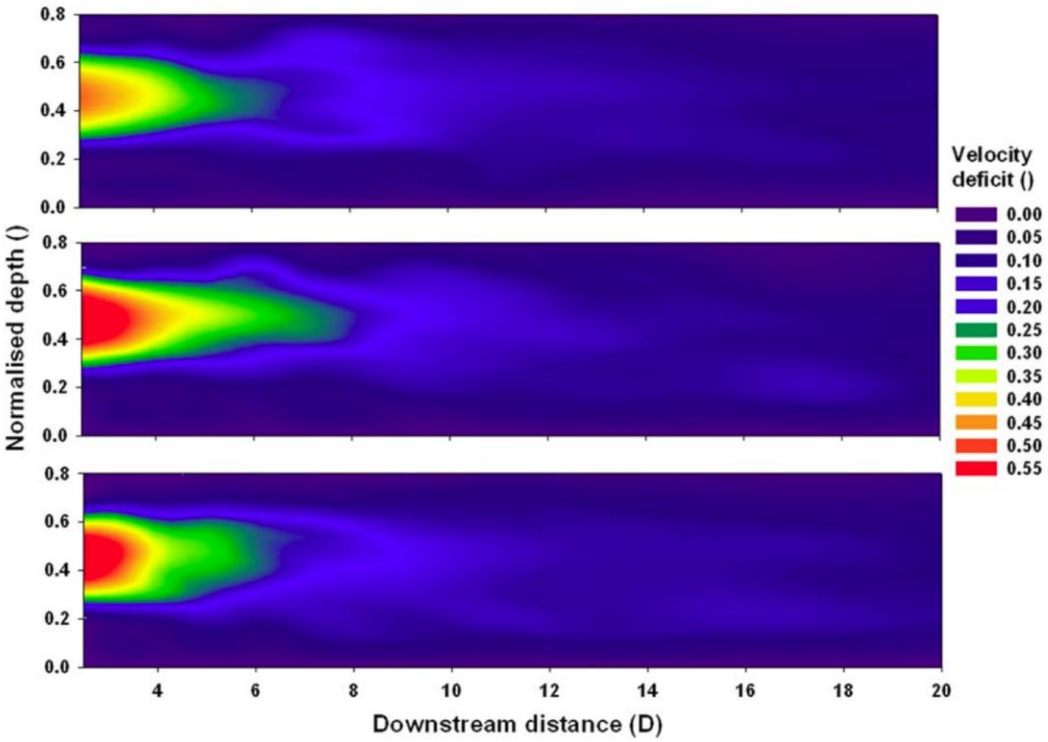

Figure 2.6- ADV captured center plane velocity deficit for varying rotor disc axial force coefficient. C_t=0.61 (top), C_t=0.86 (center) , and C_t=0.94 (bottom) [17].

The results also show that experimental and numerically modeled disc have similar characteristics. Figure 2.7 shows the comparison between numerical and experimental normalized velocity and turbulence intensity along the centerline of the channel behind the disc. Turbulence in the near wake region (4 diameters) is not well matched between the experiments and the CFD model. This is expected since the CFD model mathematically extracts momentum from the flow resulting in reduced velocity. However, the experimental disc extracts energy from the flow by converting stream-wise momentum into turbulent eddies. [9], [17]. The higher values of turbulence intensities in the near wake region, affect the wake expansion in the far region as seen in Figure 2.7. Normalized

experimental velocity follows the trend of modeled velocity but it has higher values in the wake region.

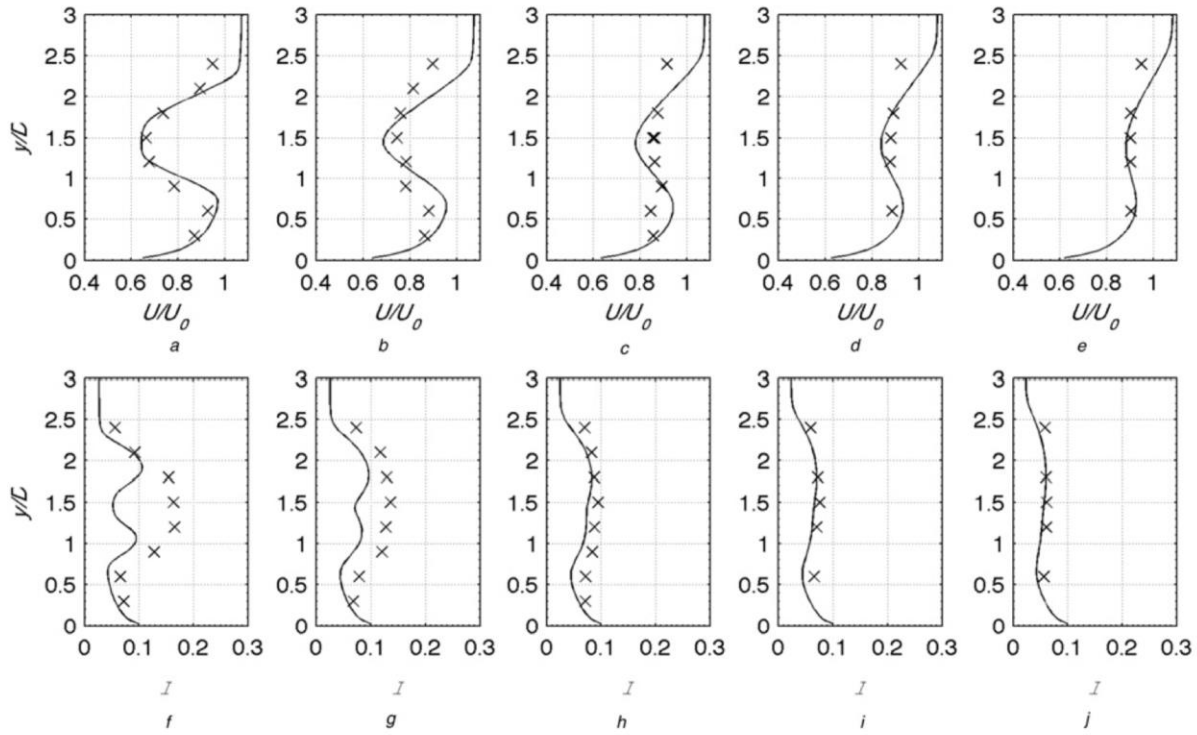

Figure 2.7- Normalized velocity and turbulence intensity through the water column on the center-line behind the actuator disc centered at y/D=1.5 with $C_t = 0.6$. a,f) 4D downstream b,g) 7D downstream c,h) 11D downstream d,i) 15D downstream e,j)20D downstream [9]

In this set of studies, blockage ratio was close to zero and surface deflection due to energy extraction of the disc was only about 0.2% of the water depth. Sun et al. [18] performed 2 dimensional and 3 dimensional RANS-ADM along with experiments to investigate this model's potential in predicting performance of hydrokinetic turbines at considerable blockage. The area of the disc contained 17% of the channel cross section (ε=17%). Figure 2.8 shows how free surface elevation changes due to power extraction of the disc.

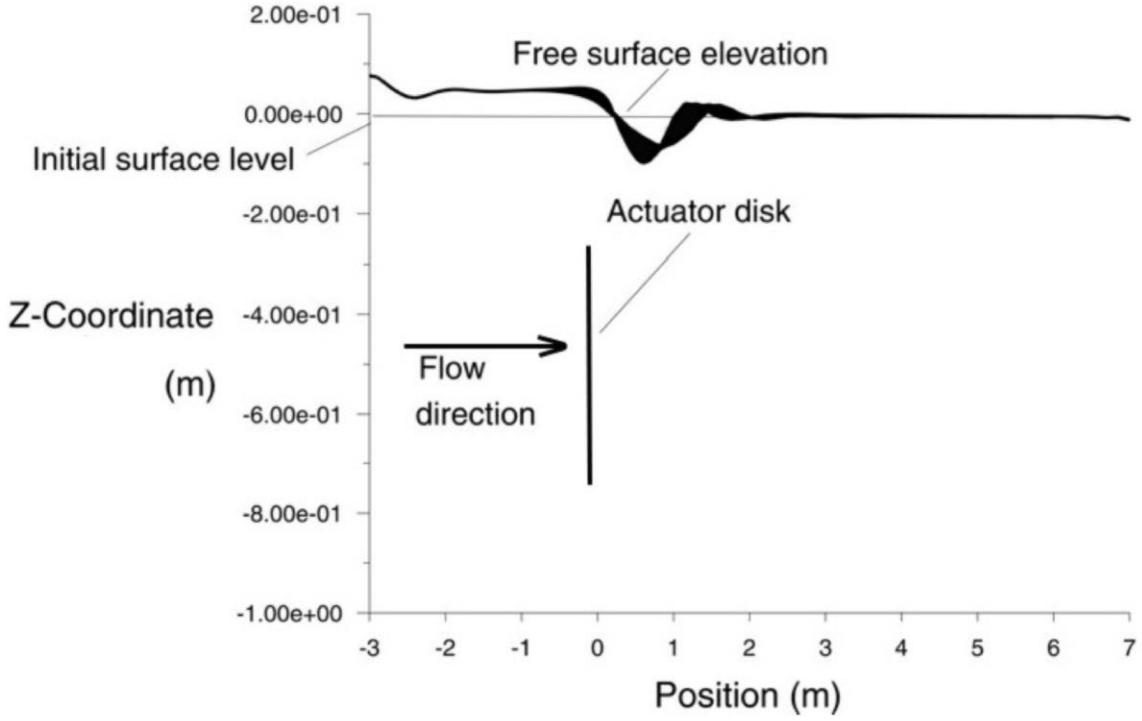

Figure 2.8- Free surface profile at channel center plane [18].

It was found that an increased level of ambient turbulence in the flow results in faster recovery of the wake [19]. Sun [19] also varied the submerged depth of the turbine. It was found that, when the actuator disk was placed closer to the free surface, the downstream wake reached the free surface faster and the decay of centerline velocity deficit in the wake was increased as shown in Figure 2.8 [19]. These results agreed with the findings of [9], [17].

Sun also varied the incoming velocity to explore the effect of Froude number. It turned out that as Froude number was increased, more power was extracted from the flow and wake recovered slower as shown in Figure 2.9. Also, more surface drop after the turbine was observed as Froude number was increased.

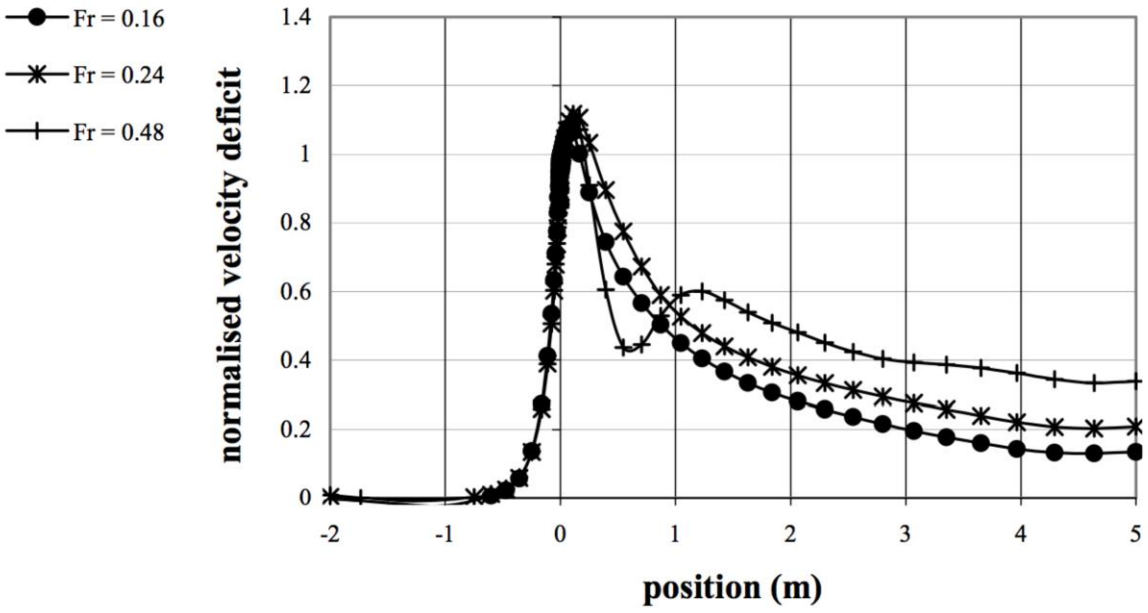

Figure 2.9- Influence of incoming flow Froude number on wake recovery

Nishino et al. [20] used 3 dimensional RANS-ADM simulations to investigate effects of blockage on the power coefficient of turbines. The free surface was not tracked in these simulations (a rigid Lid was used for the top wall boundary condition). Figure 2.10 shows that increase in blockage ratio dramatically increased the power coefficient as expected by the one-dimensional theory. According to this graph, good agreement between the one-dimensional ADM (derived by Garrett et al. [10]) and three-dimensional CFD was found. At a given blockage, if the induction factor was increased (velocity passing through the disc increased, and pressure drop across the disc increased), more useful power was extracted from the flow by the disc as shown in Figure 2.10 [20].

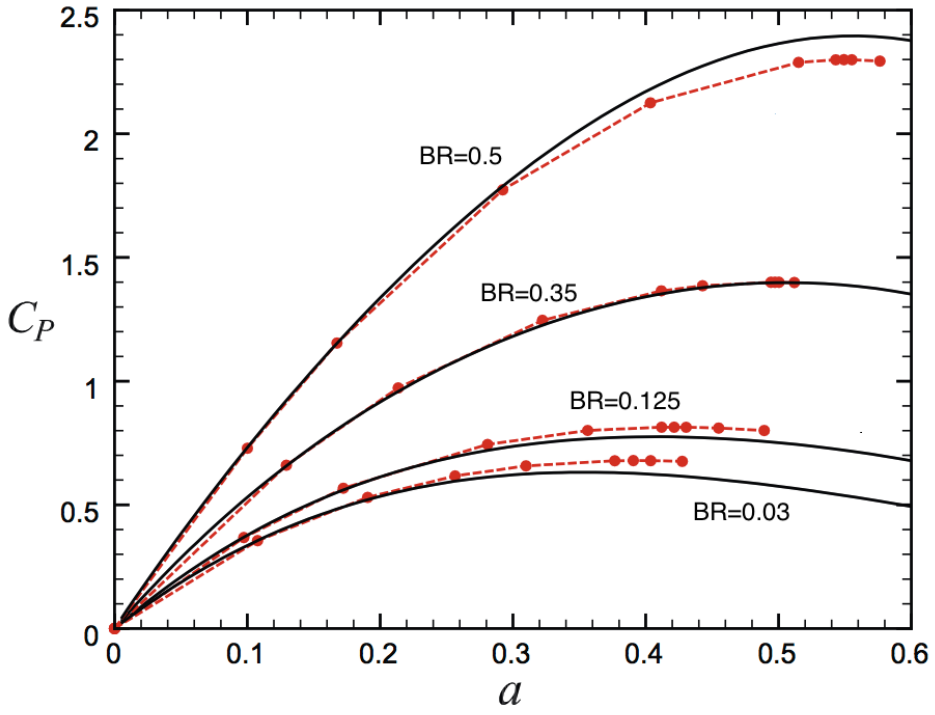

Figure 2.10- Blockage effects on power coefficient as a function of induction factor (solid lines: Linear Momentum Actuator Disc Theory, dashed lines: numerical Actuator Disc Model) [20].

2.2 Blade Element Model (BEM)

As mentioned above, the Actuator Disc Model has some shortcomings. An improved model is the Blade Element Model (BEM) which calculates forces on the blades based on their geometry and incoming flow field instead of just defining resistance across the rotor as in ADM. BEM uses Blade Element Theory (BET) which has been used for over 100 years to determine the behavior of propellers and over 40 years to analyze performance of turbines. This theory involves breaking the blade into small sections along the length of the blade and determining aerodynamic forces on each section. These forces are then integrated along the entire blade area to find axial force, tangential force, and torque acting on the

turbine. This theory is sometimes combined with linear momentum theory to take into account the induced velocity on the rotor disk known as BEMT.

Whelan et al. [13] used BEMT to create a code that predicts performance of the turbine mentioned in section 2.1.1. In this method, an initial angle of attack was guessed and based on that C_T was calculated. The induction factor was then solved for based on blockage ratio and Froude number. Once this was found, a new value for angle of attack was solved for each section of the blade. This iterative process continued until convergence was achieved. This analysis showed good agreement with the experiments at low TSR as presented in Figure 2.11. As TSR increases, a reversed flow state occurred, known as turbulent wake, where Bernoulli's theorem could not be applied. This was speculated to be one of the reasons for disagreement between BEMT code and experiments at high TSRs [13].

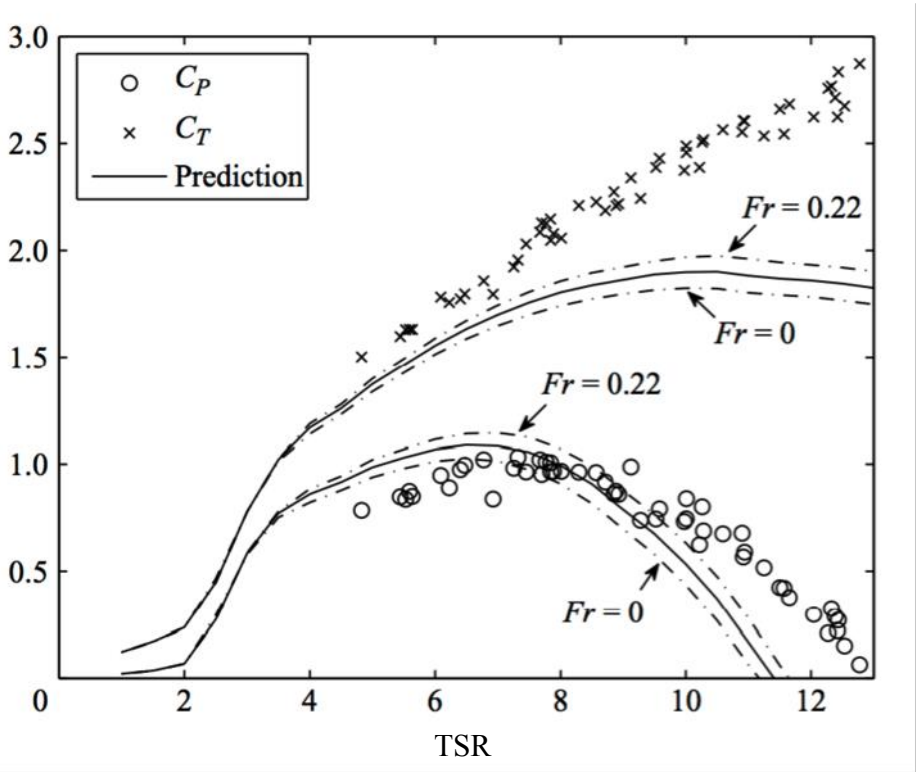

Figure 2.11- Power and axial force coefficient vs TSR at blockage ratio=0.64 [13].

Batten et al. [14] used BEM to simulate a turbine in the flow. In this model, User Defined Functions (UDF) were utilized in ANSYS CFX to calculate the momentum sink terms to feed in the flow solver. RANS equations along with the $k-\varepsilon$ turbulence model were used to calculate the flow field for discretized control volumes. Results of this simulation, which is referred to as "RANS+BE", were compared to Blade Element Momentum Theory (BEMT) (no turbulence and one-dimensional) simulations and experiments done using a towing tank. The turbine used in this work consisted of three blades, which were 0.8 meter in diameter and used NACA 48XX sections.

Figure 2.12 shows the performance of this turbine using RANS+BE, BEMT, and experiments at blockage ratio of 6% and Froude number 0.18. Experimental and BEMT results were corrected for blockage effects. Based on this figure, RANS+BE under-predicted how much of the energy exerted on the turbine was converted to useful power and over-predicted the axial force and loading on the turbine [14]. At TSR>6.5, BEMT deviated from RANS+BE and experimental results. This agreed with the findings of Whelan [13] mentioned above. It should be emphasized that this study was done at low blockage (6%) and free surface was not tracked.

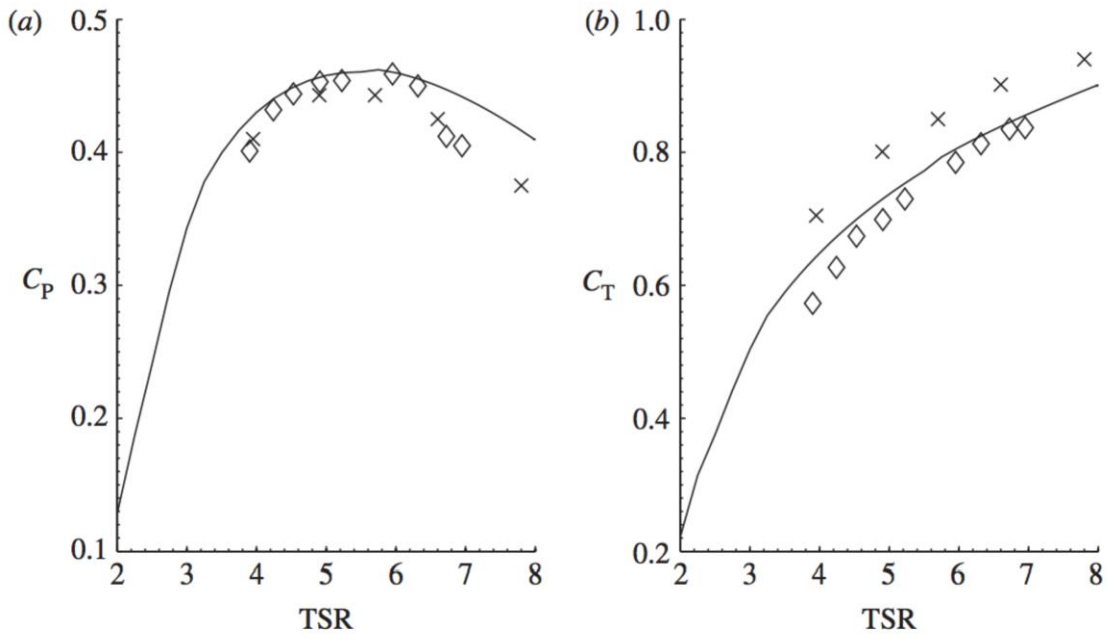

Figure 2.12- Performance of turbine using BEMT (solid line), RANS+BE (crosses), and experiments (diamonds) [14].

In another study, Consul et al. [21] explored the effects of blockage ratio and free stream deformation on the performance of a cross-flow turbine. ANSYS Fluent software was used to run two-dimensional, incompressible, unsteady simulations where a circular rotating mesh represented the turbine. $k-\omega$ turbulence equations were solved along with RANS to simulate the flow.

Consul et al. performed two different sets of simulations in regard to the water-air boundary: 1) Rigid Lid (RL) where the boundary is considered as a symmetry plane 2) deformable free surface using the VOF model. These two cases were simulated at three different blockage ratios: 12.5%, 25%, and 50%, while the upstream Froude number was maintained at 0.082. Figure 2.13 shows higher blockage ratio increased the power

coefficient. At low blockage, RL and VOF results matched closely, however, as blockage increased to 50%, differences in the power coefficient solutions reached about 6.7%. The reason for this difference was attributed to an increase in the stream wise velocity due to an increase in blockage arising from the reduction in flow depth downstream of the rotor, which occurs due to power extraction of the turbine from the flow [21]. Therefore, at high blockage ratios, it was recommended to use the VOF model, however, if blockage was low, RL as the water-air boundary was discussed to be a better option to save computational time and memory due to computationally expensive VOF calculations.

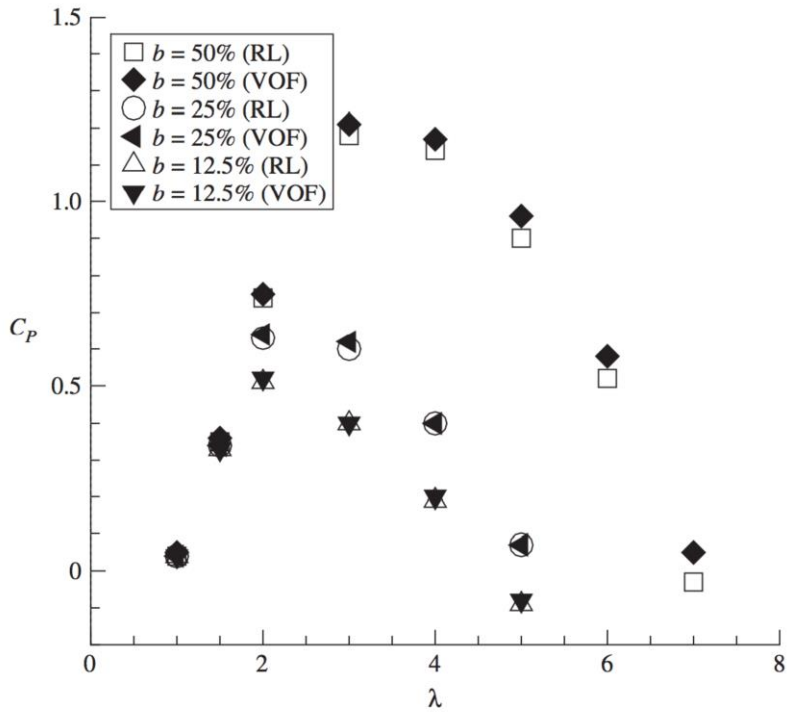

Figure 2.13- Blockage effects on power coefficient (RL: Rigid Lid, VOF: Volume of Fluid) [21].

Javaherchi [22] used published experimental and numerical data for the NREL Phase VI wind turbine to validate and compare three different numerical models such as: Single Reference Frame(SRF), Virtual Blade Model (VBM), and Actuator Disc Model (ADM). All

these models were simulated in ANSYS Fluent using RANS and $k-\omega$ equations. The SRF model was the most accurate model out of all in which the actual geometry of the blades was created. Rotation of the blades was prescribed by periodic boundary conditions. The VBM model was an implementation of the Blade Element Model in CFD. This study showed that VBM was in good agreement with the SRF model and matched other data in literature well although this model did not resolve all details directly downstream of the turbine compared to SRF. Also, it was found that ADM does not capture all flow details in near wake region as was proved in other studies [15], [9], [19]. Javaherchi concluded that VBM was the best model to use in order to investigate the performance of hydrokinetic turbines and the behavior of the far wake region [22].

2.3 Summary and work in this thesis

In this literature review, the followings were found:

1. One-dimensional ADM theory was used to set an upper limit for power extraction from the flow.
2. Increase in blockage had significant effect on performance of hydrokinetic turbines and power dissipated from the flow.
3. Numerical Actuator Disc Model and Blade Element driven models such as Virtual Blade Model were proven to have good agreement with experimental data and therefore could be used for hydrokinetic turbine performance investigations.

Most of the studies mentioned above are applied to tidal hydrokinetic turbines where blockage ratio is not high and effect of free surface is negligible. Same principles can be used to study potential of hydrokinetic turbines in rivers and channels where blockage

ratio is high and free surface deflection is expected to have substantial effects on power extraction by the turbine and head loss of the flow. This thesis studies the potential of hydrokinetic turbines for power generation and flow control in open channel flows such as irrigation canals. Main question to answer is if gates can be replaced by hydrokinetic turbines that can provide certain flow rate to the farms while producing power.

Chapter 3
Actuator Disc Model (ADM)

In this chapter, theoretical and numerical approaches are used to model the HAHT in highly blocked open channel flows. The theoretical method uses a one-dimensional control volume analysis to predict maximum power that an ideal rotor can extract from the flow as useful power and wake mixing at a given Froude number and blockage ratio. This method is then compared to the three-dimensional Actuator Disc Model (ADM) developed in commercial Computational Fluid Dynamic (CFD) code ANSYS Fluent. This model uses a porous disc to represent the HAHT and Reynolds-Average Navier-Stokes (RANS) equations along with the Volume of Fluid (VoF) model to solve for flow field and track the free surface. At the end of this chapter, the theoretical and numerical approaches are compared.

3.1 One-Dimensional Actuator Disc Theory

3.1.1 Unconstrained Channel

A simple method for calculating the limit of power extraction in a fluid is the one-dimensional linear momentum theory, first introduced by Lanchester and Betz in the 1920s [8]. Application of this one-dimensional model is used in an infinite volume of air, where the streamtube is allowed to fully expand, to analyze and design wind turbines. The flow slows down as it approaches the actuator disc. Based on conservation of energy (Bernoulli's equation), the pressure increases from p_2^- to p_2^+. The pressure then drops across the disc and in the rest of the streamtube until it reaches free-stream pressure ($p_3 = p_1$).

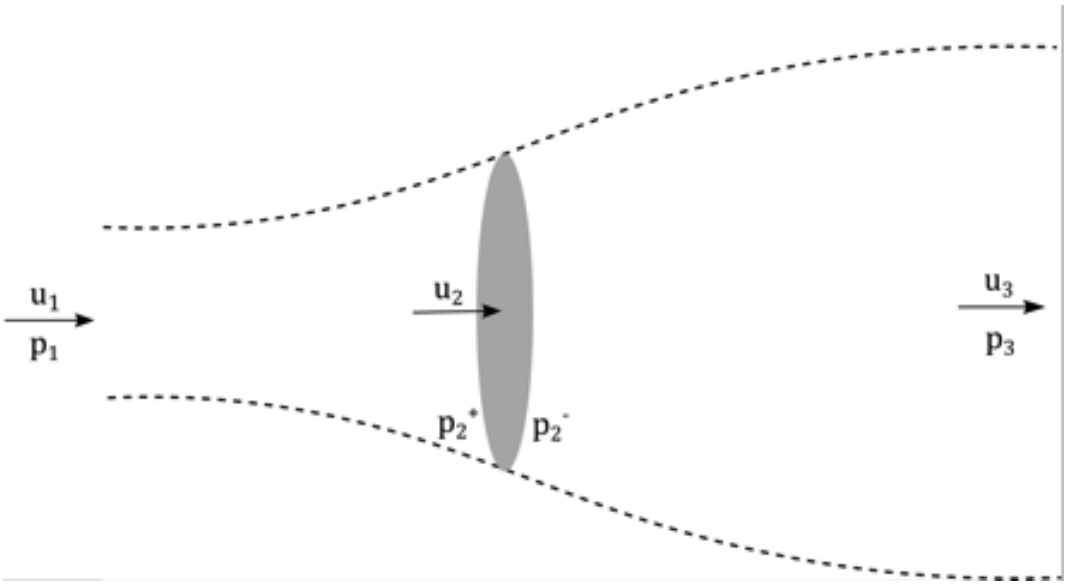

Figure 3.1-Actuator disc model of a turbine in an unconstrained flow

In this approach, the turbine is modeled as an actuator disc where net forces on the blades are uniformly distributed over the area of the disc, A_2. The axial force (thrust) applied to the disc by the flow is proportional to the pressure drop across the disc and is found by

$$\mathrm{F}_A = A_2(p_2^+ - p_2^-) = \rho u_2 A_2(u_1 - u_3) \qquad 3.1$$

Applying Bernoulli equation on two different streamlines from a location far upstream of the actuator disc to the actuator disc and from the actuator disc to a location far downstream along with Equation 2.1 proves that

$$\mathrm{u}_2 = \frac{\mathrm{u}_1 + \mathrm{u}_3}{2} \qquad 3.2$$

The power extracted by the turbine can be found by combining Equation 2.1 and 3.2.

$$\mathrm{P}_{extracted} = F_A u_2 = \frac{1}{2}\rho A_2 {u_0}^3\, 4a(1-a)^2 = \frac{1}{2}\rho A_2 {u_0}^3\, \eta_e \qquad 3.3$$

$$a = \frac{1}{3}$$

Where a is induction factor, which represents fractional decrease in flow velocity between free stream and turbine:

$$\mathrm{a} = \frac{\mathrm{u}_1 - \mathrm{u}_2}{\mathrm{u}_1} \qquad 3.4$$

The theoretical maximum power is extracted when $\mathrm{a} = \frac{1}{3}$. The efficiency associated with this induction factor is referred to as Lanchester-Betz limit and equals $\eta_e = 0.59$.

3.1.2 Constrained Channel

In contrast to wind turbines, the HAHTs operate in open channel flows where flow is constrained by channel bed and walls along with the free surface. As mentioned in the literature review, higher power is expected to be extracted by the turbines as blockage ratio increases. In this section, following from the work of Polagye [11] work was performed to derive the one-dimensional theoretical model in constrained channel. This model is then used to analyze power extracted as useful power and wake loss by an array of three turbines in channels with high blockage ratios. The following assumptions were made in this analysis:

1. By the nature of one-dimensional analysis, the power loss due to wake rotation is ignored.
2. Pressure is assumed to be hydrostatic upstream of the turbine, at the end of expansion region, and at the end of the mixing region.

3. Power dissipation due to drag force of the turbine blades is neglected.
4. Friction losses due to channel walls friction are negligible over the control volume.
5. At the end of the expansion region and beyond, water depth is uniform across the channel.

Three different control volumes are used in order to apply the conservation principles. The goal of this approach is to find velocity and depth at numbered locations of the channel as shown in Figure 3.2.

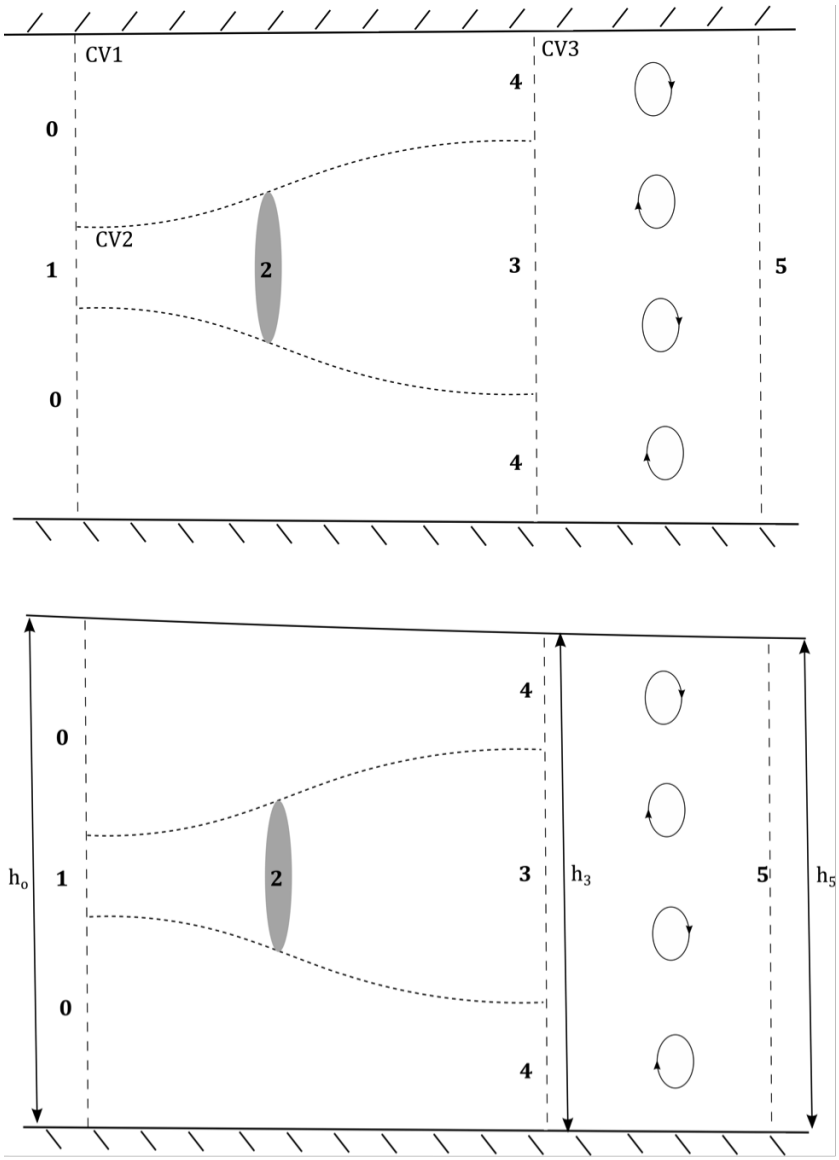

Figure 3.2- One-dimensional Actuator disc model in Open Channel Flow. Top view (top) and Side view in the center of channel (bottom).

Conservation of mass in CV 1 and CV 2 gives Equation 3.5 and 3.6.

$$u_2 A_2 = u_3 A_3 \qquad 3.5$$

Assuming $u_0 = u_1$

$$u_0(A_0 + A_1) = u_3A_3 + u_4A_4 \tag{3.6}$$

The blockage ratio is defined as the cross-sectional area of the actuator disc over the cross-sectional area of the channel as

$$\varepsilon = \frac{A_2}{(A_0 + A_1)} \tag{3.7}$$

Equation 3.6 can be rearranged using the induction factor and the blockage ratio definitions and written after a few steps as

$$\frac{u_4}{u_0} = \frac{1 - (1 - a)\varepsilon}{\frac{h_3}{h_0} - \frac{u_0}{u_3}(1 - a)\varepsilon} \tag{3.8}$$

The water depths are defined as follows: h0 is the total depth of the water at the upstream location (0/1), and h3 is the total depth at the far wake location (3/4). At these locations, as pointed out aboe, the water depth is assumed constant across the channel.

Assuming hydrostatic pressure at the two ends of CV1, conservation of momentum shows that

$$\sum F_x = \left(P_{atm} + \frac{1}{2}\rho g h_0\right)(A_0 + A_1) - \left(P_{atm} + \frac{1}{2}\rho g h_3\right)(A_3 + A_4) - P_{atm}(A_0 + A_1 - A_3 - A_4) - F_A \tag{3.9}$$

The net force in x-direction is

$$\sum F_x = \dot{m}_3u_3 + \dot{m}_4u_4 - (\dot{m}_0 + \dot{m}_1)u_0 \tag{3.10}$$

Equating Equation 3.9 and 3.10, one can solve for axial force, F_A.

$$F_A = \rho {u_0}^2 (A_0 + A_1) - \rho {u_3}^2 A_3 - \rho {u_4}^2 A_4 + \frac{1}{2}\rho g h_0 (A_0 + A_1) - \frac{1}{2}\rho g h_3 (A_3 + A_4) \quad (3.11)$$

Using Bernoulli's equation on a streamline from the upstream location to the actuator disc and a streamline from the disc to the downstream location, one can find the pressure drop across the disc and consequently the axial force:

$$F_A = \Delta \mathrm{p}\, A_2 = \rho g A_2 [h_0 - h_3 + \frac{u_0^2}{2g} - \frac{u_3^2}{2g}] \quad (3.12)$$

Combining Equations 3.11, 3.12 and 3.8, one can write an equation which is in terms of $\frac{u_4}{u_0}$, $\frac{u_3}{u_0}$, Fr_0, $\frac{h_3}{h_0}$, ε, and a.

$$\left(1 - \frac{u_4}{u_0}\right) + (1-a)\varepsilon\left(\frac{u_4}{u_0} - \frac{u_3}{u_0}\right) + \frac{1}{2Fr_0^2}\left[1 - \left(\frac{h_3}{h_0}\right)^2\right] = \frac{\varepsilon}{2}\left[\frac{2}{Fr_0^2}\left(1 - \frac{h_3}{h_0}\right) + 1 - \left(\frac{u_3}{u_0}\right)^2\right] \quad (3.13)$$

This analysis used conservation of mass and momentum in CV1 and CV2 up to now. Next, assuming hydrostatic pressure at locations 0,1,3, and 4, conservation of energy in CV1 is written as

$$(\dot{m}_0 + \dot{m}_1)\left(\frac{\cancel{P_{atm}}}{\cancel{\rho}} + g h_0 + \frac{u_0^2}{2}\right) = \dot{m}_3 \frac{u_3^2}{2} + \dot{m}_4 \frac{u_4^2}{2} + (\dot{m}_3 + \dot{m}_4)\left(\frac{\cancel{P_{atm}}}{\cancel{\rho}} + g h_3\right) + \dot{W} \quad (3.14)$$

The power extracted from the flow due to the axial force at the turbine is found by multiplying 3.12 by u_2:

$$\dot{W} = F_A\, u_2 = \rho A_2 u_2 [g(h_0 - h_3) + \frac{u_0^2}{2} - \frac{u_3^2}{2}] \quad (3.15)$$

Combining Equation 3.14 and 3.15, extraction coefficient can be found as

$$C_p = \eta_e = \frac{\dot{W}}{\frac{1}{2}\rho A_2 u_0^3} = \frac{u_2}{u_0}\left[\left(\frac{u_4}{u_0}\right)^2 - \left(\frac{u_3}{u_0}\right)^2\right] \quad 3.16$$

Substituting Equation 3.15 for power in Equation 3.14 gives the following relation:

$$\frac{u_4}{u_0} = \sqrt{1 + \frac{2}{Fr_0^2}\left(1 - \frac{h_3}{h_0}\right)} \quad 3.17$$

Where Fr_0 is the Froude number, which is the ratio of inertia to gravity forces:

$$Fr_0 = \frac{u_0}{\sqrt{g h_0}} \quad 3.18$$

Equations 3.8, 3.13, 3.17 form a system of three equations and three unknowns that can be solved for dependent variables ($\frac{u_4}{u_0}, \frac{u_3}{u_0}, \frac{h_3}{h_0}$) at given Fr_0, ε, and a.

Once the normalized flow speeds and depths are known for the expansion region, these properties can be found for the location far downstream after mixing region by applying conservation principles at CV3.

Conservation of mass in CV 3 gives

$$u_3 A_3 + u_4 A_4 = u_5 A_5 \quad 3.19$$

Or after rearranging in terms of known properties

$$\left(\frac{u_5}{u_0}\right)\left(\frac{h_5}{h_0}\right) = (1-a)\varepsilon + \left(\frac{u_4}{u_0}\right)\left(\frac{h_3}{h_0} - \frac{u_0}{u_3}(1-a)\varepsilon\right) \quad 3.20$$

Applying conservation of momentum to CV3 gives:

$$\rho {u_5}^2 A_5 - \rho {u_3}^2 A_3 - \rho {u_4}^2 A_4 = \frac{1}{2}\rho g h_3 (A_3 + A_4) - \frac{1}{2}\rho g h_5 A_5 \qquad 3.21$$

Or after rearranging

$$\left(\frac{u_5}{u_0}\right)^2 \left(\frac{h_5}{h_0}\right) + \frac{1}{2Fr_0^2}\left(\frac{h_5}{h_0}\right)^2 = \left(\frac{u_3}{u_0}\right)(1-a)\varepsilon + \left(\frac{u_4}{u_0}\right)^2 \left(\frac{h_3}{h_0} - \frac{u_0}{u_3}(1-a)\varepsilon\right) + \frac{1}{2Fr_0^2}\left(\frac{h_3}{h_0}\right)^2 \qquad 3.22$$

Equation 3.20 and 3.22 are solved simultaneously to find the unknowns ($\frac{h_5}{h_0}$, $\frac{u_5}{u_0}$) at given Fr_0, ε, and a.

3.1.3 Results

In this section, the one-dimensional theory is used to study the effects of blockage ratio on power production and head loss of the flow in the channel. The actual cross-sectional geometry of geometry the channel where the High Hills gates are installed in West Canal is trapezoidal. The equivalent rectangular geometry is used for simplicity of the equations. In the modeling, three turbines, 4m in diameter, are placed in the channels perpendicular to the flow. The width of the channel is decreased to increase the blockage ratio and the incoming velocity. The equivalent channel width is 21m and in the modeling this is reduced to 16m. This increased the blockage ratio from 0.36 to 0.48 while Froude number varied from 0.18 to 0.24. As the blockage ratio reaches 0.48, two different solutions are found. One responds to a subcritical solution shown in red line in Figure 3.3 and the other one is the supercritical solution shown in red dashed line. For the case of the 16m wide channel, an axial induction factor of 0.21, only the subcritical solution occurs, and above a = 0.53, only the supercritical solution is found.

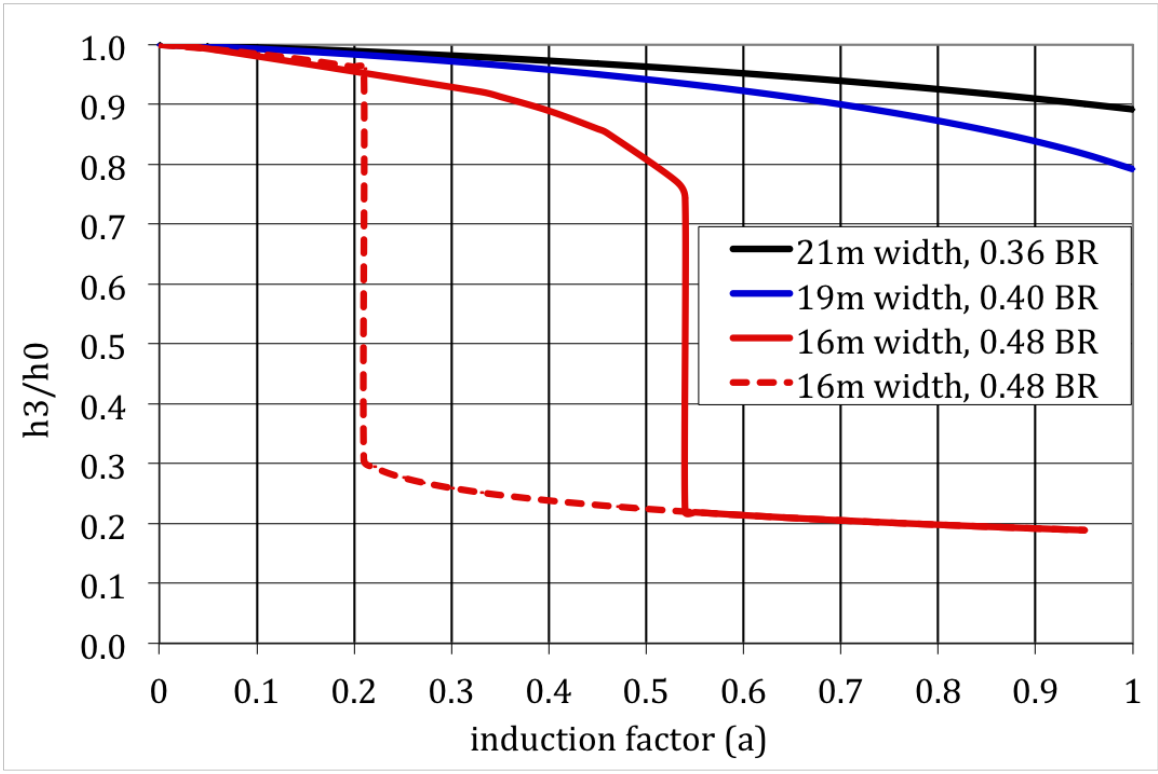

Figure 3.3-Effect of channel constriction on surface drop at the end of the expansion region.

As channel becomes more constricted, surface drop increases behind the turbines at all induction factors. In the supercritical case, flow right behind the turbine accelerates strongly, causing the free surface ($\frac{h_3}{h_0}$) to drop dramatically even at small induction factors as shown in Figure 3.3.

Higher power is extracted at high blockage ratios. For example, at an induction factor of 0.4, useful power extracted by the actuator discs is estimated to be 245kW in the 16 meter wide channel and 60 kW for the induction factor of 0.5 in the 21 wide meter channel. Extraction coefficient or efficiency for these two cases is 2.7 and 1.56 respectively. If flow behind the turbine becomes supercritical in the 16m wide channel, power extracted increases to 1026kW . This extreme increase in power generation in the supercritical case

may appear appealing, however, flow behind the turbines in this situation becomes too harsh due to the high surface drop that may result in exposing the back side of the turbine to air and high flow velocity passing around the turbine. Therefore, in further modeling of high blockage ratio, we choose to stay on the subcritical branch (ie, on the solid red line below a = 0.53).

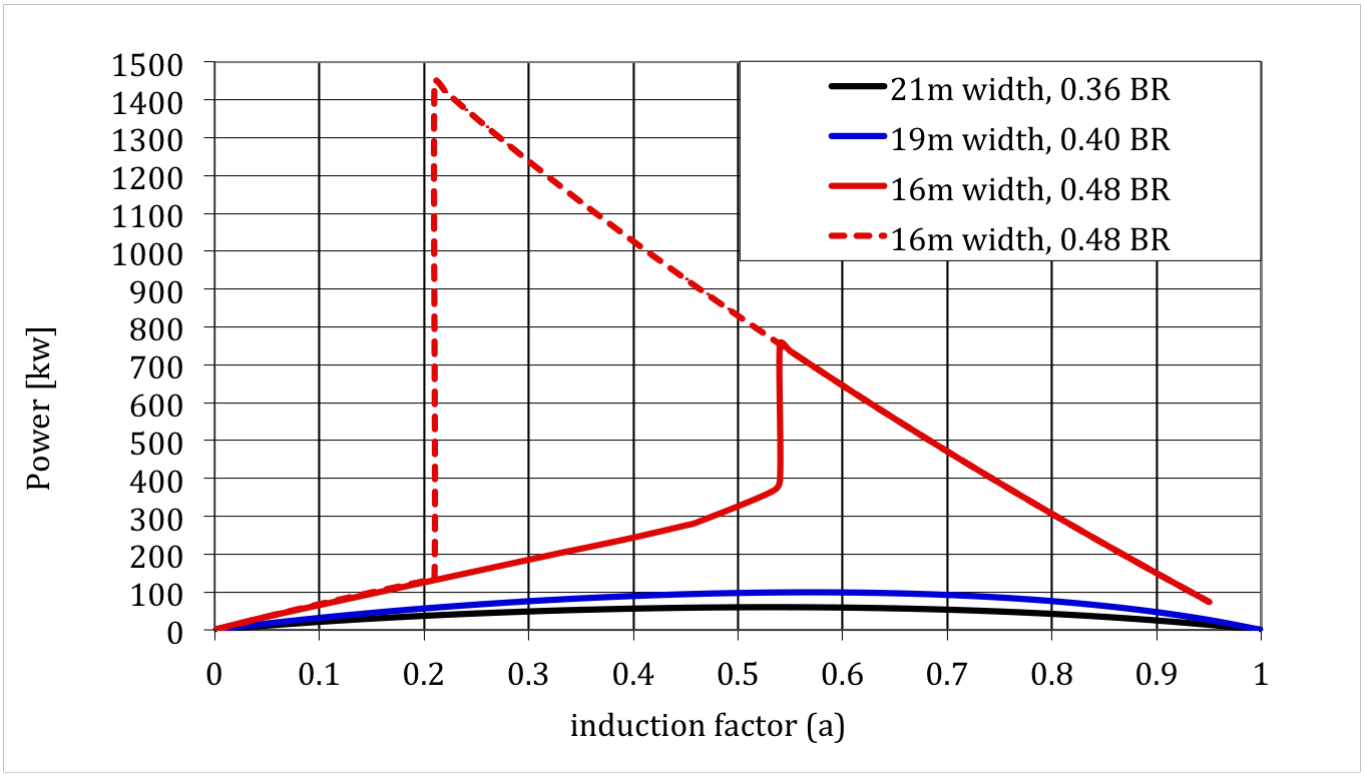

Figure 3.4-Effect of channel constriction on power production

As blockage ratio is increased, the confinement of the channel and free surface became more significant; therefore, flow velocity adjacent to the stream tube increases. This led to higher shear between the wake and fast moving outer flow, creating higher mixing and consequently higher head loss. Figure 3.5 shows the total elevation loss of the flow due to power extraction of the turbines and power loss due to the mixing region.

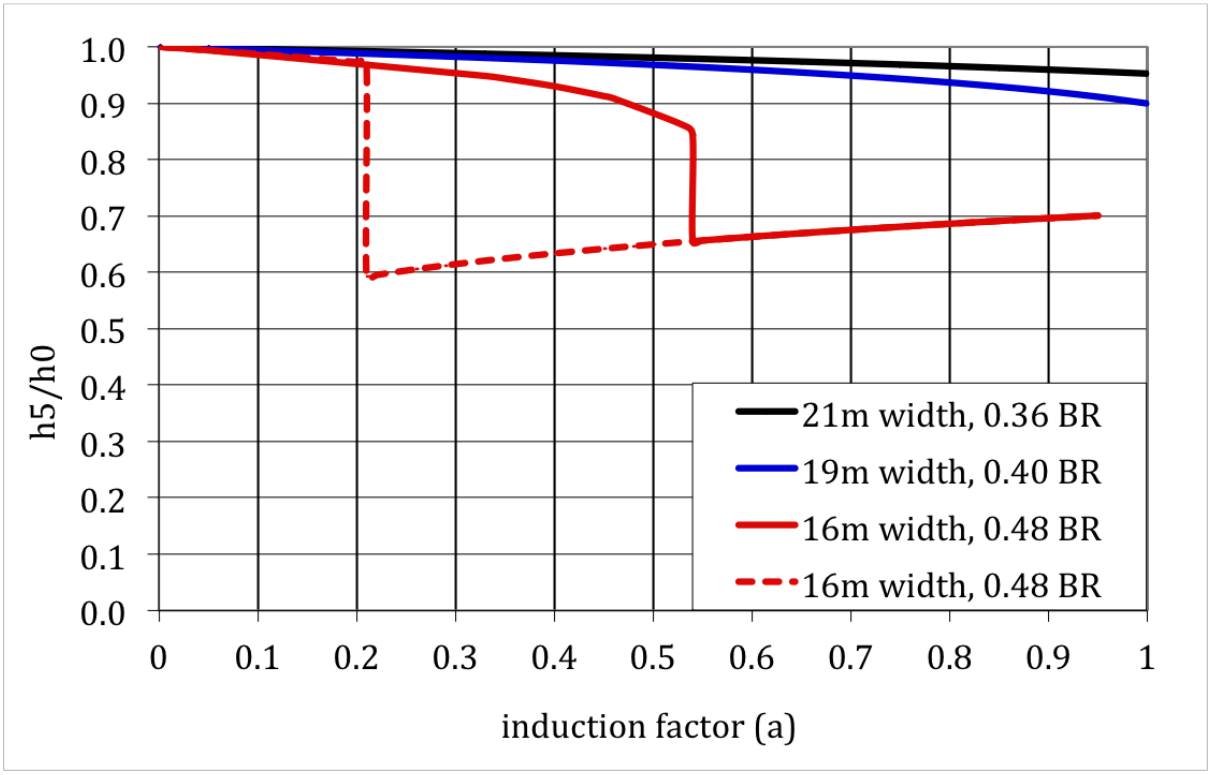

Figure 3.5-Effects of channel constriction on head loss due to power extraction of turbines and power loss of the mixing region.

These results are compared to the 3D numerical modeling of the 21m and 16m wide channels in Section 3.3.

3.2 Numerical Modeling

Fluid flows are described by partial differential equations (PDEs), which represent the conservation laws (conservation of mass, momentum and energy). Computation Fluid Dynamics (CFD) is the art of replacing these equations by algebraic equations that can be solved with computers in order to produce quantitative predictions of flow phenomena [23]. This tool is used to perform "numerical experiments" in a "virtual flow laboratory" that reduces full-scale testing costs.

The CFD software used in this thesis is ANSYS Fluent 14.0. The fluent solver uses the finite volume approach to integrate the PDEs over individual control volumes of the computational domain. Then, linearized equations are solved to find dependent variables such as velocity and pressure throughout the domain. This process continues until the solution is converged within an allowable error threshold.

3.2.1 Governing Equations

Most laminar incompressible flow characteristics can be solved using conservation of mass and Navier-Stokes equations:

$$\frac{\partial \rho}{\partial t} + \nabla . (\rho \vec{u}) = 0 \qquad 3.23$$

$$\frac{\partial}{\partial t}(\rho u_i) + \frac{\partial}{\partial x_i}.(\rho u_i u_j) = -\frac{\partial p}{\partial x_i} + \frac{\partial}{\partial x_j}.\left[\mu\left(\frac{\partial u_i}{\partial x_j} + \frac{\partial u_j}{\partial x_i}\right) - \frac{2}{3}\delta_{ij}\frac{\partial u_l}{\partial ul}\right] + \rho\vec{g} + S_i \qquad 3.24$$

In Equation 3.24, u_i is the velocity vector, δ_{ij} is kronecker delta, μ is the dynamic viscosity, and S_i is the source term.

But, not all flows are considered laminar. Open channel flows are turbulent motions that satisfy Equation 3.23 and 3.24 instantaneously. It takes large computation time and resources to capture velocity fluctuation and diffusion in turbulent flows at small scales. To reduce this requirement, Fluent solves a closed system of time-averaged equations consisting of Reynolds-Average Navier-Stokes (RANS) equations to find the flow field variables such as velocity and pressure. The RANS equations are derived by substituting Reynolds Decomposition for velocity and pressure for incompressible flows, into the conservation of mass and momentum equations. Resulting equations are then time-averaged. RANS equations are presented in tensor notations in the single equation below.

$$\frac{\partial}{\partial t}(\rho u_i) + \frac{\partial}{\partial x_i}.(\rho u_i u_j) = -\frac{\partial p}{\partial x_i} + \frac{\partial}{\partial x_j}.\left[\mu\left(\frac{\partial u_i}{\partial x_j} + \frac{\partial u_j}{\partial x_i}\right) - \frac{2}{3}\delta_{ij}\frac{\partial u_l}{\partial ul}\right] + \rho\vec{g} + S_i + \frac{\partial}{\partial x_j}(-\rho\overline{u_i' u_j'}) \quad 3.25$$

Where u_i from now on are time averaged velocity in this equation. This equation has an extra term compare to the Navier-Stokes equations, $-\rho\overline{u_i' u_j'}$, which is referred to as Reynolds stress tensor and represents the turbulence transport effects on the mean flow. By introducing the Reynolds stress tensor, more unknowns are added to the equations. In order to close the problem, it is necessary to introduce additional equations to express the Reynolds stress in terms of flow properties such as velocity.

Fluent offers a number of turbulence closure models. These models are based on the Boussinesq hypothesis that relates the Reynolds stresses to the mean velocity gradients.

$$-\rho\overline{u_i' u_j'} = \mu_t\left(\frac{\partial u_i}{\partial x_j} + \frac{\partial u_j}{\partial x_i}\right) - \frac{2}{3}\left(\rho k + \mu_t\frac{\partial u_k}{\partial x_k}\right)\delta_{ij} \quad 3.26$$

In this equation, μ_t is the turbulence viscosity and k is the turbulence kinetic energy. The Boussinesq hypothesis is used in some common turbulence models such as Spalart-Allmaras model, $k-\varepsilon$, and $k-\omega$. The model used in this thesis is $k-\omega$ Shear-Stress Transport (SST) because it's a robust model as well as it is widely used in hydrokinetic turbine CFD simulations. In addition to this, $k-\omega$ SST is known to perform better than the Spalart-Allmaras model and $k-\varepsilon$ in situations with adverse pressure gradients and separated flow [24]. In this model, turbulence kinetic energy, k, and specific dissipation rate, ω are obtained from the following transport equations:

$$\frac{\partial}{\partial t}(\rho k) + \frac{\partial}{\partial x_i}.(\rho k u_i) = \frac{\partial}{\partial x_j}\left(\Gamma_k \frac{\partial k}{\partial x_j}\right) + G_k - Y_k + S_k \qquad 3.27$$

and

$$\frac{\partial}{\partial t}(\rho \omega) + \frac{\partial}{\partial x_i}.(\rho \omega u_i) = \frac{\partial}{\partial x_j}\left(\Gamma_\omega \frac{\partial \omega}{\partial x_j}\right) + G_\omega - Y_\omega + D_\omega + S_\omega \qquad 3.28$$

In these equations, Γ_k and Γ_ω are effective diffusivities of k and ω, G_k and G_ω represent the generation of turbulence kinetic energy and specific dissipation rate respectively. Y_k and $Y_\omega$represent the dissipation of k and ω, and finally S_k and S_ω are source terms. D_ω is the cross-diffusion term. This model is explained in full details in the theory guide of ANSYS Fluent [25].

3.2.2 Solver Settings

The Fluent finite volume solver takes the following steps to numerically solve the flow field:

1) The domain is divided into discrete control volumes using a grid (mesh)
2) Governing equations are integrated over the individual control volumes to construct algebraic equations for the dependent variables (unknowns) such as velocity, pressure.
3) The discretized equations are linearized and the system of linearized equations is solved to yield updated values of the dependent variables.

3.2.2.1 Numerical solver choice

The pressure-based numerical solver is used in the simulations rather than the density-based solver since open channel flows deal with low speed incompressible flows. In this

method, a pressure equation is derived from the continuity and momentum equations such that the velocity field, corrected by the pressure, satisfies the continuity equation [25].

A coupled algorithm is used in the pressure-based numerical solver, which solves system of momentum and pressure-based continuity equations simultaneously. This method is known to improve convergence speed compared to a segregated algorithm. However, it uses more memory since the system of equations needs to be stored in every iteration.

The linearized equations for each cell can be shown in a simplified manner as:

$$a_p \phi = \sum_{nb} a_{nb} \phi_{nb} + b \qquad 3.29$$

Where subscript nb refers to neighboring cell, ϕ is the scalar variable at cell center, b is the net flow rate into the cell, a_p and a_{nb} are the linearized coefficients for ϕ and ϕ_{nb} respectively.

The conservative pseudo Transient under-relaxation method is used for time stepping. This approach is supposed to reduce the time it takes the solver to achieve convergence by adding a damping term to the linearized equations as in Equation 3.30.

$$\underbrace{\rho_p \Delta V_p \frac{\emptyset - \emptyset_{old}}{\Delta t}}_{damping\ term} + a_p \phi = \sum_{nb} a_{nb} \phi_{nb} + b \qquad 3.30$$

In this equation, ρ_p is the cell density, ΔV_p is the volume of the cell, and Δt is the pseudo time step defined as $\Delta t = \min(\Delta t_{convection}, \Delta t_{dynamic}, \Delta t_{gravitational}, \Delta t_{viscous}, \dots)$. Refer to Fluent manual for more details [25].

3.2.2.2 Volume of Fluid (VOF) model

The Volume of Fluid (VOF) model is applied to the solver in order to track the free surface deflection. This model is used for multiphase flows where the position of the interface is of interest. In this technique RANS equations are solved and the volume fraction of each phase in the fluid is tracked throughout the domain. Volume fraction of each phase is represented by α_q, where q is the desired phase.

Conservation of mass can be written in terms of volume fraction as

$$\frac{\partial}{\partial t}(\alpha_q \rho_q) + \nabla.(\alpha_q \rho_q \overrightarrow{v_q}) \quad 3.31$$

RANS equations, Equation 3.25, along with turbulence equations are solved by having density and viscosity in term of volume fraction of each phase in cells.

$$\rho = \sum \alpha_q \rho_q \quad 3.32$$

$$\mu = \sum \alpha_q \mu_q \quad 3.33$$

In the case of open channel flow, density of each phase is found as

$$\rho = \alpha_{water} \rho_{water} + (1 - \alpha_{air}) \rho_{air} \quad 3.34$$

Therefore, volume fraction of 1 represent a cell filled with water whereas volume fraction of 0 means pure air. The free surface is defined where volume fraction is 0.5.

3.2.2.3 Solution initialization

Hybrid initialization is used to create a velocity field in the computational domain and a pressure field that smoothly connect high and low-pressure values. In this method, Laplace equation is solved with appropriate boundary condition to create the velocity field. An

additional Laplace equation is solved to produce initial pressure values for all cells. Volume fraction is patched to the secondary phase, which is the heavier fluid (water), in the section of the domain containing water.

3.2.2.4 Summary of solver settings

The summary of the solver settings is presented in Table 3.1.

Table 3.1- Solver settings

Solver	Coupled pressure-based Steady Open Channel Flow
Multiphase flow	Volume of Fraction (2 phases) Primary phase: air Implicit scheme/Open Channel Flow Body Force Formulation: Implicit
Viscous Model	$k-\omega$ SST Model Constants: default
Solution Methods	Pressure-Velocity Coupling: Coupled with VF Pseudo Transient
Spatial Discretization	Gradient: Least Squares Cell Based Pressure: PRESTO! Momentum: 2nd Order Upwind

	Volume Fraction: QUICK Turbulent Kinetic Energy: 2nd Order Upwind Specific Dissipation Rate: 2nd Order Upwind
Pseudo Transient Explicit Relaxation Factors	Pressure: 0.5 Momentum: 0.5 Density: 1 Body Forces: 1 Turbulent Kinetic Energy: 0.75 Specific Dissipation Rate: 0.75 Turbulent Viscosity: 1

3.2.3 Meshing

The geometry of the computational domain is first determined from the actual channel geometry provided from [26]. The actual channel width is 21m; however, a constricted case is also considered where channel width is assumed to be 16m. It is decided to place three turbines; each 4 meters in diameter on one transect perpendicular to the flow. This provides two cases with blockage ratios of 0.36 and 0.48 respectively. Spacing between the turbines is kept at one meter in both cases. The outer turbines are 1 meter from the side-walls of the channel in the 16 meter wide channel and are 3.5 meters from the walls for the 21 meter channel.

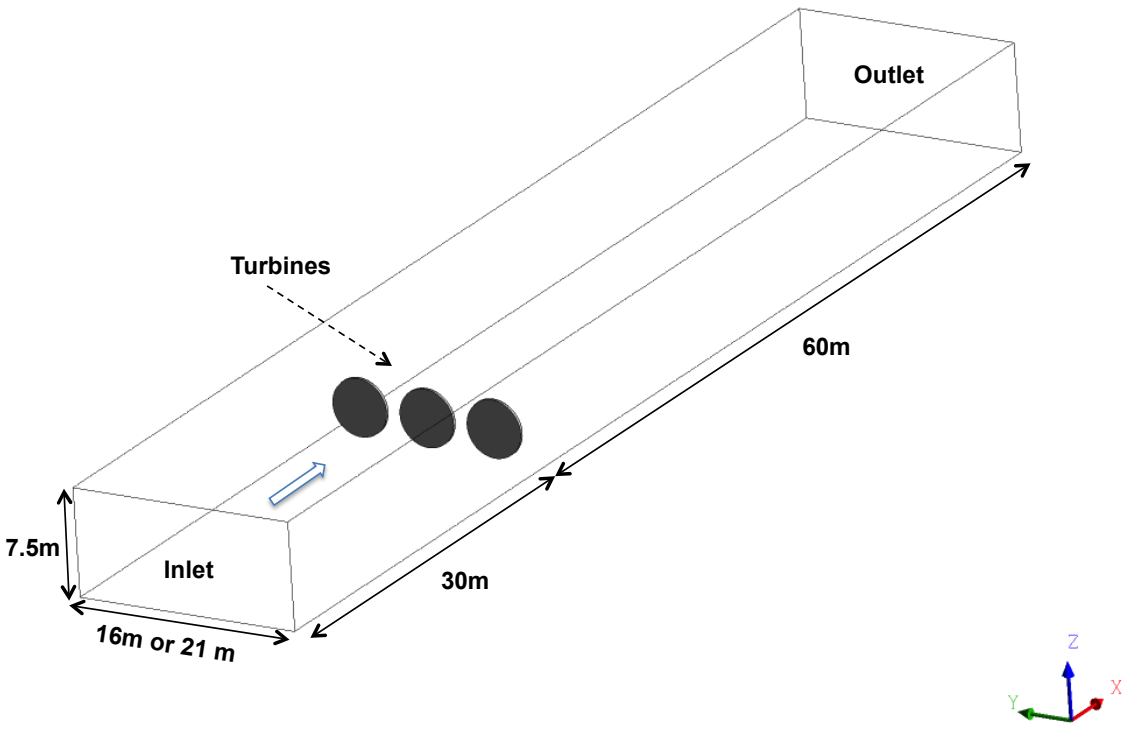

Figure 3.6- Geometry of computational domain

This domain is then spatially discretized to smaller hexahedral control volumes. Meshing is performed in GAMBIT software. Nodes are placed every 20cm along the edges of the channel. An unstructured quad (pave) mesh is then created on the cross-sectional area where turbines are placed. This mesh was then extruded to create the 3D mesh of the channel.

This grid is refined near the free surface in order to capture free surface deflections that occur due to power extraction of the turbines and avoid numerical instability for volume fraction. Therefore, once a stable and converged solution is found, the mesh is refined where volume fraction varies between 0.4 and 0.6. This procedure is continued until the

solution is independent of the mesh resolution. The final mesh consists of 3.3 million hexahedral cells for the 16m wide channel and 4.2 million cells for the 21m wide channel. Figure 3.7 shows the mesh at the cross-section of the channel where turbines are placed in the 16m wide channel.

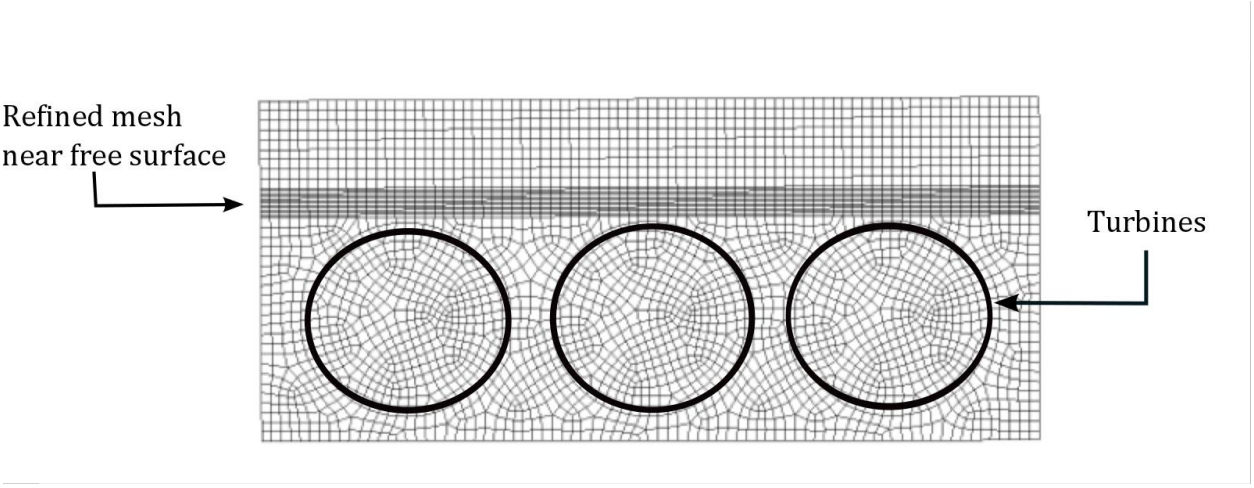

Figure 3.7- Cross-sectional area of the mesh

Quality of the mesh plays an important role in accuracy and stability of the solution. One of the indicators of a good mesh is orthogonal quality, which varies between 0 and 1, where values close to 0 correspond to low quality. This value was 0.8 for both channels' mesh, which indicates that the domains are well discretized.

3.2.4 ADM numerical settings

3.2.4.1 Boundary Condition

The boundary conditions used in the simulations for the 16m and 21m channels are summarized in Table 3.2. It should be noted that mass flow rate is intended to be kept constant in the channels, therefore, inlet depth is lower for the 16m wide channel compared to the 21m channel.

Table 3.2-Boundary condition used in ADM for 21m and 16m wide channels respectively.

Inlet	Mass flow rate	Water: 132,850 [kg/s] Air: 50 [kg/s] Free Surface Level: 5m, 4.937m Turbulence intensity, I: 1% Hydraulic Diameter: 8m, 7.545m
Outlet	Pressure	Free surface Level: 5m, 4.937m Turbulence Intensity, I: 1% Hydraulic Diameter: 8m, 7.545m
Channel bed and walls	No slip	
Top wall	Symmetry	

Turbulence at the inlet and outlet is defined by introducing turbulence intensity, I, and hydraulic diameter, D_H. These terms define k and ω at the boundaries. Turbulence intensity is defined as the ratio of the root-mean-square of the velocity fluctuations, u', to the mean flow velocity. Hydraulic diameter is defined as four times the cross-sectional area of the channel over its wetted perimeter. Knowing these two parameters, Fluent solves for k and ω at the boundaries from the following equations:

$$k = \frac{3}{2}(u_{ave}\, I)^2 \tag{3.35}$$

$$\omega = \frac{k^{\frac{1}{2}}}{C_\mu^{\frac{1}{4}} l} \tag{3.36}$$

In these equations, C_μ is an empirical constant specified in the turbulence model (about 0.09) and l is the turbulence length scale which deals with size of the turbulent eddies entering and exiting the domain. This length scale is 0.53m for the 16m wide channel and 0.56m in the 21m wide channel.

$$l = 0.07\, D_H \tag{3.37}$$

Turbulent intensity is usually determined from experiments to feed into the CFD for inlet boundary conditions. However, since no turbulence measurement was taken at the channel, a low turbulent intensity of 1% is picked for the inlet. As mentioned in the literature review, higher values of ambient turbulence intensity result in faster wake recovery. By choosing the low turbulence intensity level at the inlet, results from the simulations represent the slowest wake recovery expected. It is assumed that far downstream of the turbines, the flow recovers to the original state; therefore, turbulence intensity was chosen to be about 1% at the outlet.

$$I = 1\%$$

3.2.4.2 Porous media

Porous medias are treated by adding a momentum sink term to the RANS equations as mentioned in Section 2.1.2. This sink term consists of a viscous loss term (Darcy's law) and an inertial loss term as in 3.38.

$$S = \frac{\Delta p}{\Delta t} = -\left(\underbrace{\frac{\mu}{\alpha} u_2}_{Viscous\ loss} + \underbrace{C_2 \frac{1}{2} \rho u_2^2}_{Inertial\ loss} \right) \tag{3.38}$$

In this equation, α is the permeability of the porous media, and C_2 is the inertial resistance. This momentum sink contributes to the pressure drop across the porous media proportional to fluid velocity in the cell:

$$S = \frac{\Delta p}{\Delta t} \qquad 3.39$$

Where Δt is the thickness of the porous media and in this case is set to 0.2m.

Permeability and inertial resistance constants are usually found experimentally [19]. However, for the purpose of this thesis, it is assumed that permeability of the disc is very low, thus, $\frac{1}{\alpha} = 0$ which agrees well with Sun [19]. One-dimensional theory is used to determine C_2 for both channel widths. Given an induction factor, pressure drop across the disc is found using one-dimensional theory. This pressure drop and u_2, calculated from the chosen induction factor, are then used to calculate C_2 from Equation 3.38. This provides a method for comparing the one-dimensional theory to the three dimensional ADM model.

Table 3.3- Inertial coefficient for the porous media

Channel width	a	Δp [kPa]	u_0 [m/s]	C_2 [1/m]
21m	0.5	2.5	1.268	62.3
16m (subcritical)	0.4	6.8	1.685	66.65
16m (supercritical)	0.6	25.4	1.685	560

3.2.5 Validation

As mentioned in literature review, Sun [19] used ANSYS Fluent 12.0 to perform numerical modeling using a porous media to represent a HAHT . Sun validated the numerical results

with experimental data achieved using porous discs. Good agreement was found between numerical and experimental results as discussed in details in [19]. In order to validate the numerical settings used in this thesis, same case as Sun's simulation was created in ANSYS Fluent 14.0.

There were a couple of differences in the kind of solver and the outlet boundary condition between Sun's thesis and this thesis. In this thesis, the Coupled pseudo-transient solver is utilized which is expected to converge faster compared to the solver Sun used (SIMPLE solver). Sun applied a User Defined Function (UDF) to create a gauge pressure boundary condition at the outlet in Fluent 12.0. However, Fluent 14.0 provides an option to automatically provide the free-surface level at the outlet without using a UDF. In order to validate the solver settings and the outlet boundary condition used in this thesis, Sun's case is recreated with an outlet free surface defined at the same depth, 10% more, and 10% less than the inlet free surface depth. Figure 3.8 shows that the case with similar free-surface depth at inlet and outlet has the highest accuracy compared to Sun's case. Relative percent difference between the cases run with ANSYS Fluent 14.0 and Sun's case is presented in Table 3.4. Based on this table, the power generated by turbine and surface drop across the porous media was accurately modeled using the new settings.

Table 3.4- Relative percentage difference between the simulations ran with solver settings used in this thesis (Coupled and pseudo transient with output pressure boundary condition defined using a surface level) to the Sun's published data (SIMPLE solver with pressure boundary condition to calculate the outlet gauge pressure)

	Power Generated [%]	**Surface Drop [%]**
Recreation of Sun's data with new solver settings	0.3	1.7
10% increase in outlet free-surface	19.0	32.3
10% decrease in outlet free-surface	22.2	52.1

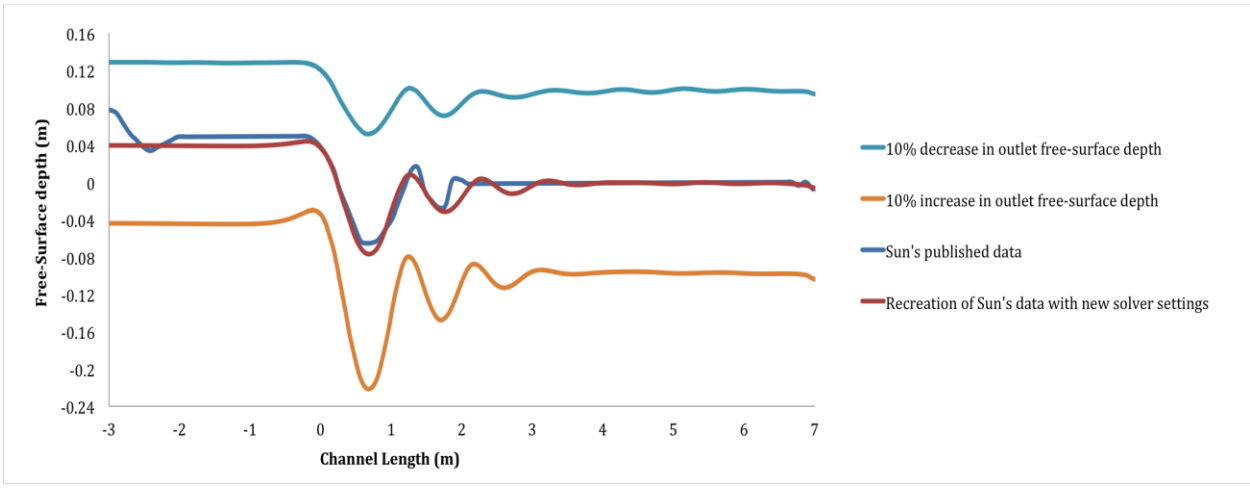

Figure 3.8- Comparison between free surface level of Sun's validated data and the recreated cases using the new solver settings used in this thesis (Initial free surface level was located at z=0).

Using the pseudo-transient Coupled solver has a few advantages over the SIMPLE solver. The number of iterations to achieve convergence at 1e-4 for all residuals and 1e-6 for mass flow rate is reduced by a factor of 8. This was achieved while real time convergence is lowered 5 times compared to Sun's solver settings using the same boundary conditions and mesh resolution.

3.2.6 CFD Results

3.2.6.1 Velocity Field and Surface Elevation

As mentioned above, three different cases corresponding to blockage ratios of 0.36 (21m wide channel) and 0.48 (16m wide channel) are considered for numerical simulation. Figure 3.9 shows the top-view of velocity plots that corresponds to the subcritical solutions of the 16m and 21m wide channels. These plots are made on a plane parallel to the channel bed passing through the center of the actuator discs.

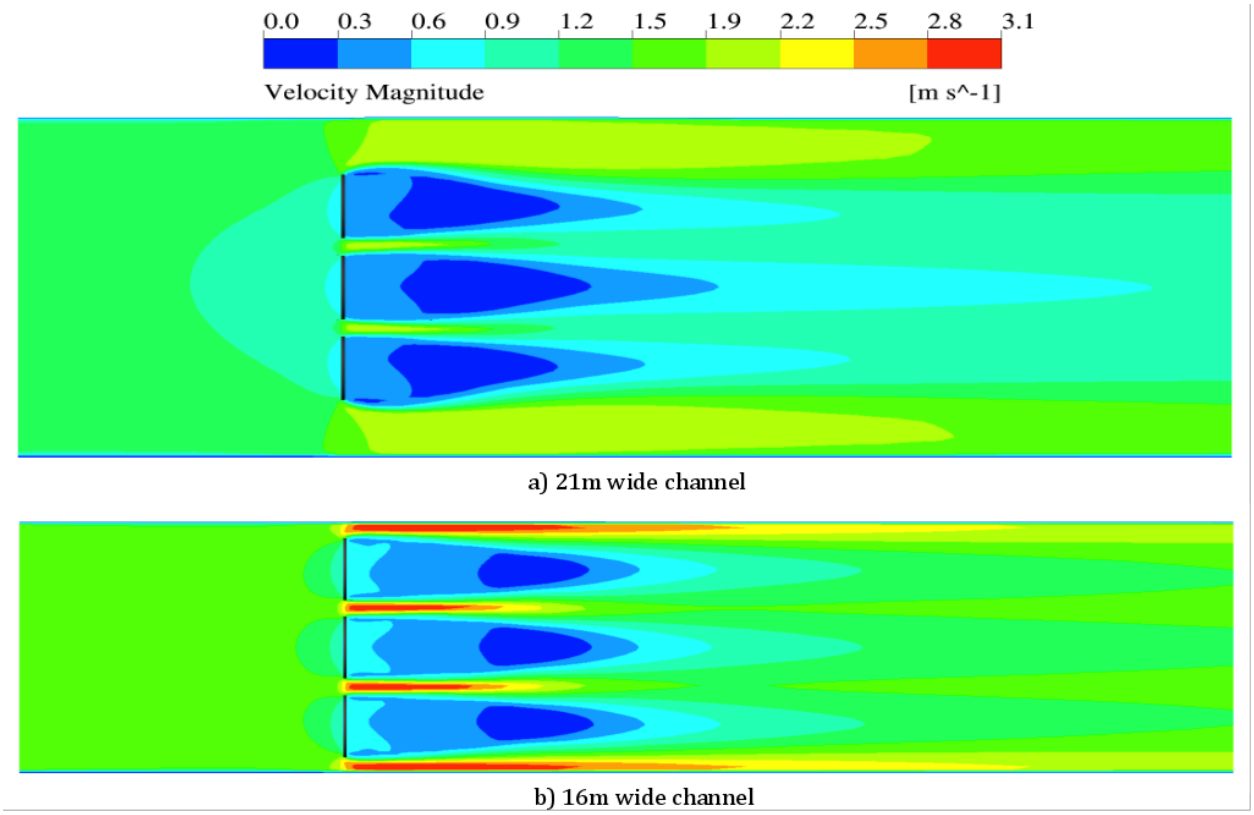

Figure 3.9- Top view of velocity magnitude plots on a plane parallel to the channel bed passing through the center of discs. a) 21m wide channel, BR=0.36, Fr=0.18 b) 16m wide channel (subcritical), BR=0.48, Fr=0.24

In these plots, the velocity of the flow increases as it passes around the actuator discs and slows down as it mixes with the wake. The velocity increase is about 50% higher in the 16m wide channel compared to the 21m wide channel. The wake regions of the actuator discs extend 6 and 10 diameters downstream of the discs for the 16m wide channel and 21m wide channel respectively. Therefore, the wake recovers faster in the case with high blockage ratio (and Froude number) than the other case. This may be due to higher velocity of fluid in the channel and higher bypass flow velocity.

In Figure 3.9a, wake of the actuator discs near the walls appear to recover faster than the middle actuator disc. However, Figure 3.9b shows about the same lengths for wake region. This may be due to higher velocity of the flow and similar spacing between the turbines and the channel walls (1 m) in the 16m wide channel case.

Flow is locally induced at every individual turbine for both cases. However, the lower blockage case shows an array induced velocity in addition to the velocity induction at individual turbines. In this case, an array turbine wake is seen in Figure 3.9a. However, this phenomenon is not observed in the case with BR=0.48. This is shown in Figure 3.10.

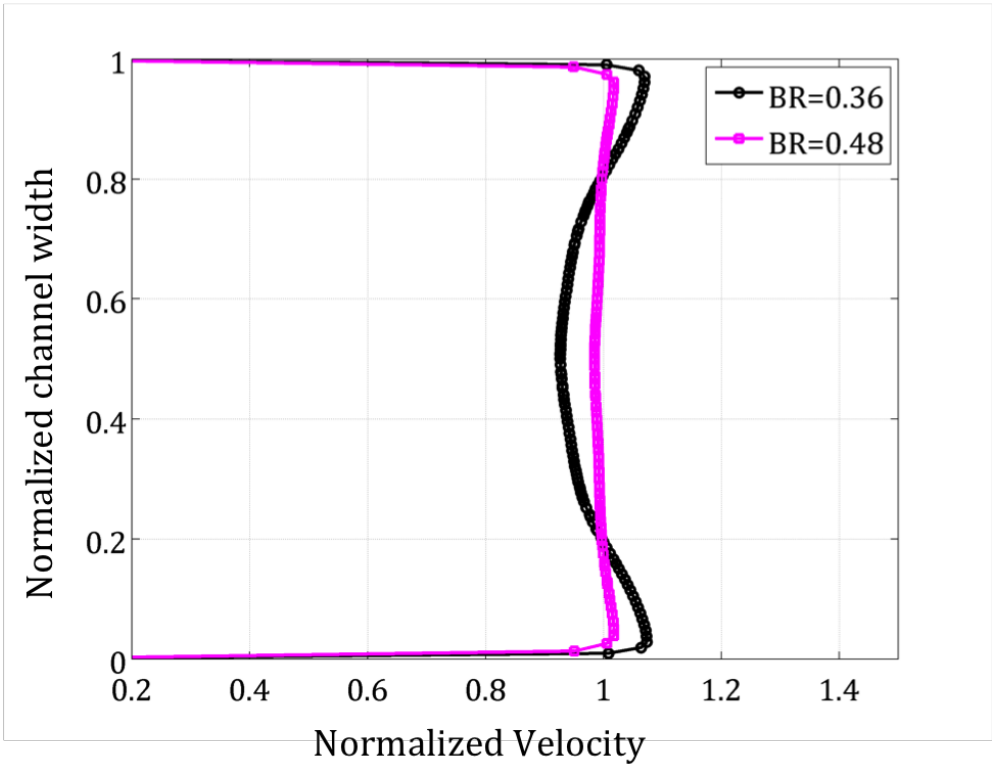

Figure 3.10- Normalized velocity versus the normalized channel width 1D upstream of the turbines.

In order to investigate the wake recovery, velocity magnitude is normalized by upstream velocity and plotted against normalized depth by upstream depth 5 diameters (5D)

upstream, 5D, 10D, and 15D downstream of the middle turbine for the 21m wide channel and the 16m wide channel (subcritical) in Figure 3.11. Based on this figure, the normalized free-surface velocity at 5D downstream of the middle turbine reaches the free stream velocity for the 16m wide channel whereas the normalized velocity is about 0.5 for the 21m wide channel. In the case of the 16m wide channel, velocity recovers to about 97% of the upstream magnitude 15D downstream of the middle turbine.

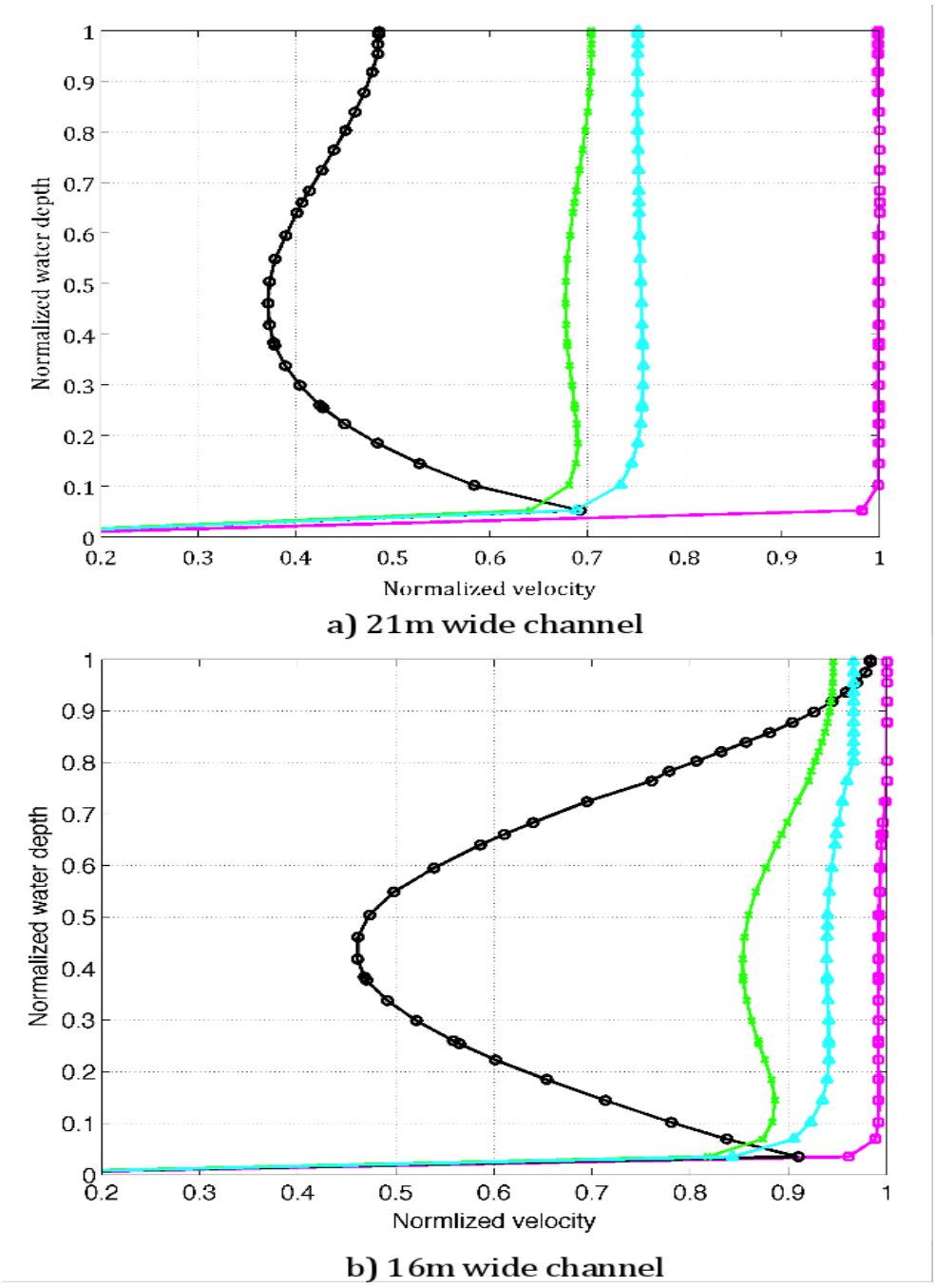

Figure 3.11-Normalized depth versus normalized velocity 5D upstream, 5D, 10D and 15D downstream of the middle turbine for a) 16m wide channel and b) 21m wide channel. The turbine axis is located at normalized depth of 0.5.

The dynamic pressure plots of the vertical plane passing through the center of the middle turbine are presented in Figure 3.12. Dynamic pressure, q, is the kinetic energy per unit volume of the fluid and is defined as

$$q = \frac{1}{2}\rho u^2 \tag{3.40}$$

When dealing with open channel flows, it is difficult to distinguish velocities of each phase. Using dynamic pressure, it's easier to visualize how fast each fluid moves, since velocity is squared in its definition, and to distinguish the free surface, due to dependency on density. Since incoming velocity of water is higher by 33% in the 16m wide channel case and dynamic pressure is related to velocity squared, two different scales are used in Figure 3.12.

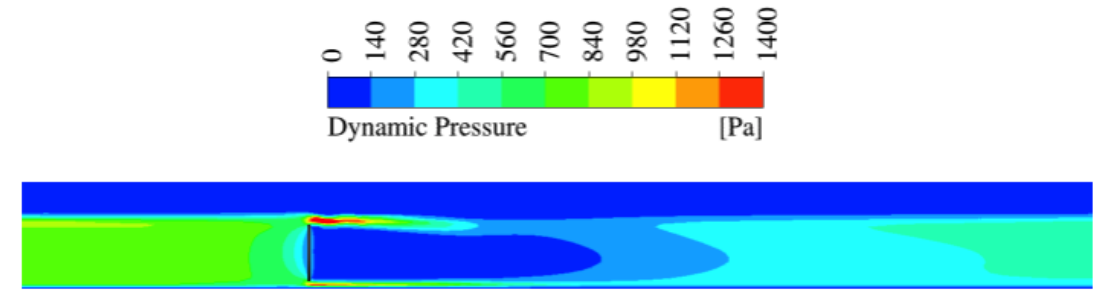

a) 21m wide channel

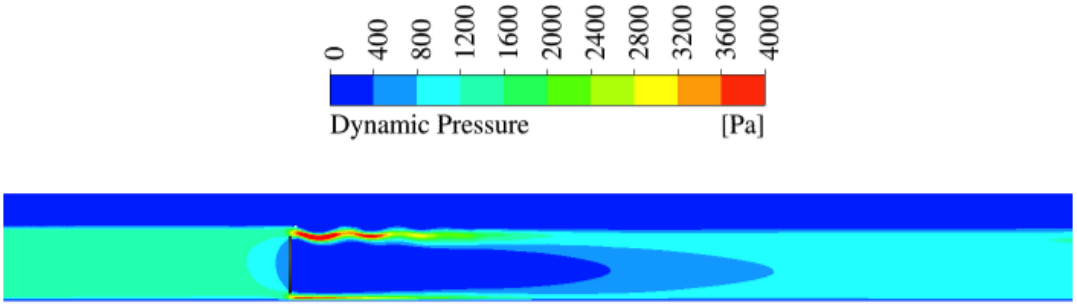

b) 16m wide channel

Figure 3.12-Dynamic pressure plot of a vertical plane passing through the center of middle turbine.

In order to better and more accurately visualize the free surface, normalized water depth is calculated along the channel for the subcritical and supercritical cases. This plot is made where volume fraction of fluid is equal to 0.5 on a plane vertical to the channel, passing through the center of the middle turbine.

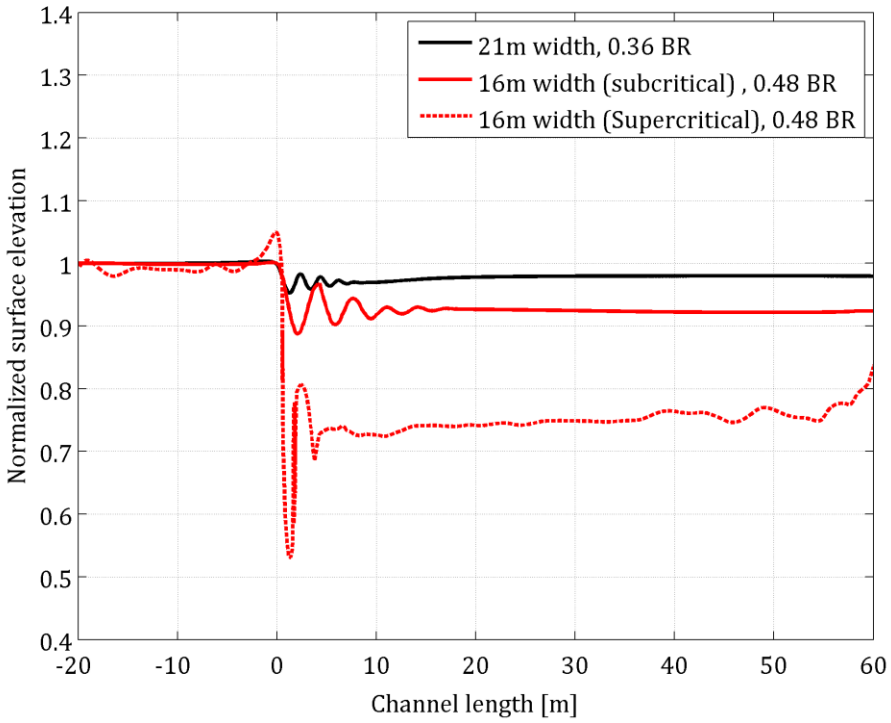

Figure 3.13- Normalized surface elevation plot along the channel length for the middle turbine in the 21m and 16m wide channels.

Based on this figure, as blockage ratio increases, the surface drop behind the actuator discs increases. Also, higher head loss is observed for the higher blockage ratio. This is due to higher power extraction of the turbines and the higher rates of mixing between high speed flow passing around the turbines and the turbine wakes.

A nearly converged solution is found for the supercritical case using the numerical settings used in this thesis. The velocity plot of the free-surface is shown in Figure 3.14. Water elevation behind the turbine drops dramatically and velocity increases. This causes the flow to go through a hydraulic jump in order to reach the downstream subcritical water level. In such a high velocity and surface drop behind the turbines, it may not be advisable to run HAHTs.

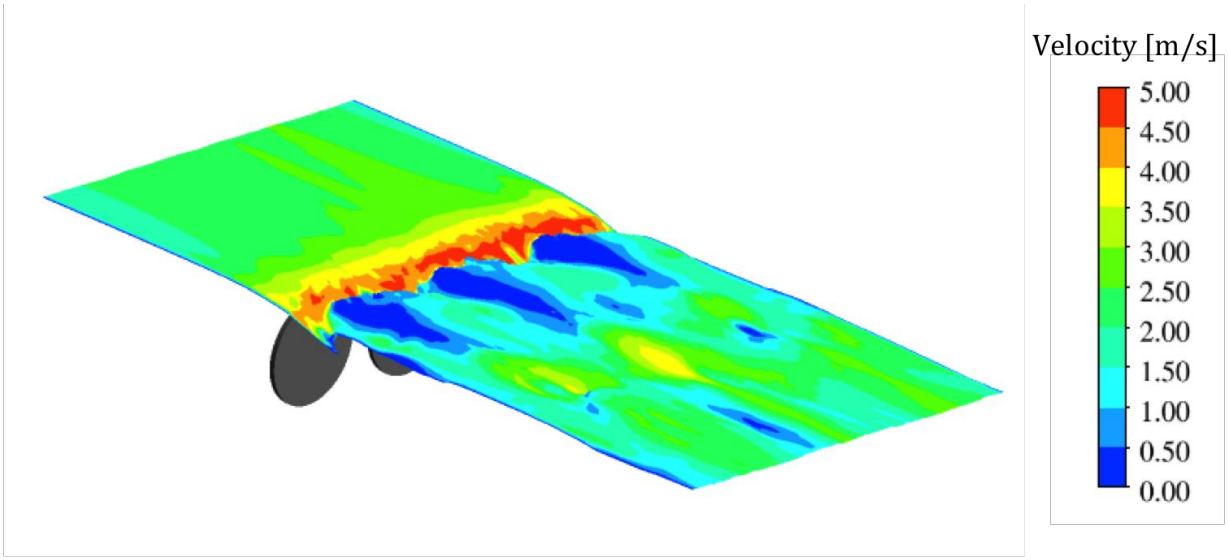

Figure 3.14- Velocity plot along the channel length for the supercritical case in 16m wide channel.

3.2.6.2 ADM without tracking the free surface

Tracking the free surface using the VOF model is important in predicting the power extraction of turbines in high blockage ratios. The ADM is used to investigate the effect of disregarding the free surface on performance prediction of the turbines. Therefore, VoF model is neglected in Fluent and the region corresponding to air is subtracted from the grid to maintain the desired blockage ratio. The top boundary condition is set to a wall with momentum shear of zero (free slip condition).

Power extraction by turbines is under predicted when the free surface is not included in the simulation. The under prediction of extraction efficiency increases, as blockage ratio is raised (i.e. power is under predicted by 12% when BR=0.48 and 7% when BR=0.36). Therefore, it is important to use the VoF model to track the

3.3 Comparison between 1D theory and CFD

Comparison is made between the results obtained from numerical modeling to the one-dimensional theory in order to investigate the differences between the models. Table 3.5 shows some important results obtained from the one-dimensional theory and three-dimensional CFD solutions for the normalized velocity at the actuator disc, $\frac{u_2}{u_0}$, normalized minimum depth behind turbine $\frac{h_3}{h_0}$, and normalized far wake depth, $\frac{h_5}{h_0}$. In order to compare three-dimensional CFD analysis to the one- dimensional theory, u_2 is integrated over the actuator disc area, u_5 is integrated over the cross-sectional area of a plane perpendicular to the channel bed at the outlet, h_3 and h_5 are averaged across the channel where volume fraction is 0.5 where lowest surface drop was observed and the outlet respectively.

Table 3.5- Comparison between CFD solution and 1D theory for 16m wide and 21m wide channel cases.

	21m wide channel (BR=0.36) $a = 0.5$		**16m wide channel (BR=0.48)** $a = 0.4$	
	1D theory	**CFD**	**1D theory**	**CFD**
$\frac{u_2}{u_0}$	0.5	0.487	0.6	0.587
$\frac{h_3}{h_0}$	0.963	0.964	0.89	0.884
$\frac{h_5}{h_0}$	0.98	0.982	0.93	0.955
Δp $[kpa]$	2.5	2.1	6.4	4.5
C_p	1.558	1.32	2.70	1.96
η_d	1.128	1.2	2.22	1.86

According to this table, both methods are in general agreement. Pressure drop in both cases is lower in the CFD solution than the 1D theory. This may be due to the increase in water level due to blockage in the computation domain and consequently decrease of flow velocity as it approaches the discs. As blockage ratio increases, these effects become more pronounced. In both cases, head loss by the CFD is higher than by the one-dimensional theory. This is expected due to assumptions made in the 1D theory such as dealing with ideal instead of viscous fluid and neglecting the power dissipated by the circulation region of the wake.

Chapter 4
Virtual Blade Model (VBM)

4.1 Numerical Modeling

A method for analyzing the aerodynamic interactions between multiple rotors and a fluid is the Virtual Blade Model introduced by Zori et al. and Yang et al. in 1995 [27]. This approach uses a momentum source term that implicitly represents the rotor. Therefore, blades are taken into account in the simulation without being physically present in the computational domain. This simplification reduces the computational memory and time required to perform the analysis compared to the simulations where the actual rotating blades are modeled, due to number of mesh cells, which would be required to resolve the blades.

In 2005, Ruith et al. implemented VBM in ANSYS Fluent to simulate flows for a rotor in a fluid [8]. This method utilizes Blade Element Theory (BET), explained in Section 4.1.1, to solve for the magnitude of the momentum source term in the RANS equations based on local angel of attack and velocity at the rotor for each iteration. Velocity field is then determined for the rest of the domain using the RANS equations. Iteration is continued until solution is converged.

4.1.1 Theory

The Virtual Blade Model (VBM) employs the Blade Element Theory (BET) to analyze the aerodynamic forces applied to the blades of a turbine, as a function of blade geometry and the incoming velocity field. When using this method, the blade is divided into N sections (maximum number of sections is 20) or elements as shown in Figure 4.1. Lift and drag

forces are calculated for each of these elements and integrated along the entire blade area. In order to calculate these forces, the user is required to input the following quantities:

1. The geometry of the blade, including the chord length and twist angle of each of the different N sections.
2. Rotational speed of the turbine in terms of Tip Speed Ratio (TSR) and local pitch angle.
3. Lift and drag coefficients, defined in terms of the angle of attack in a look up table imported in VBM.

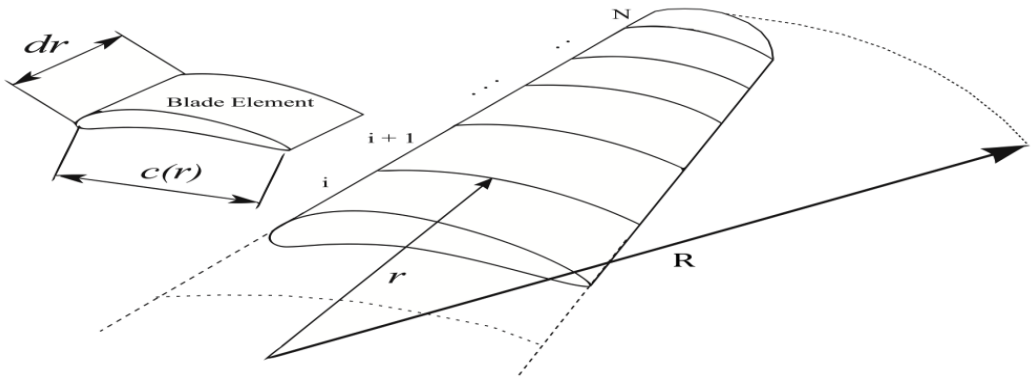

Figure 4.1- Blade elements along the blade

Using geometry of the airfoil shown in Figure 4.2, lift and drag forces which are vertical and tangential forces with respect to the airfoil are calculated for each blade element using Equation 4.1 [8].

$$dF_{L,D} = C_{L,D}\frac{1}{2}\rho c\, V^2 dr \qquad 4.1$$

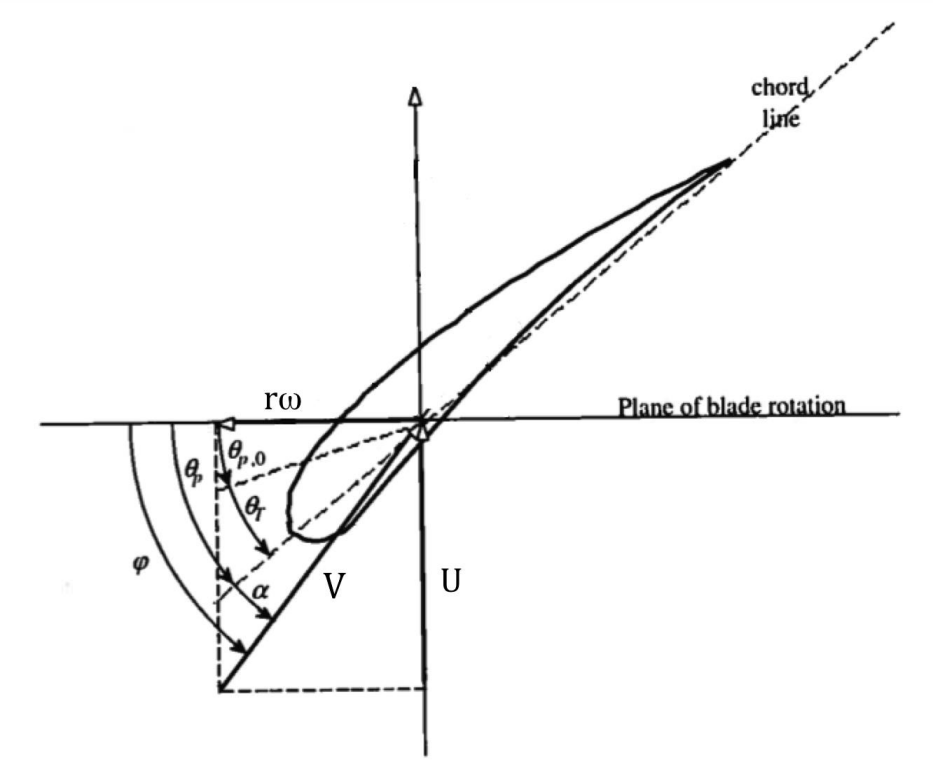

Figure 4.2- Airfoil geometry

Where $dF_{L,D}$ is the local incremental lift or drag force on the blade element, c is the cord length, and V is the relative velocity found by Equation 4.7. Assuming constant rotational speed, these forces can be geometrically averaged over one revolution or 2π radians. Therefore, on a per cell basis, the lift and drag forces can be found using Equation 4.2.

$$F_{L,D,cell} = \beta \int_0^R dF_{L,D} = \frac{\beta d\emptyset}{2\pi}\, dF_{L,D} \qquad 4.2$$

In this equation, β is the number of blades of the rotor and $\emptyset$ is the azimuthal coordinate.

The lift and drag forces can then be converted to tangential and normal forces within the element plane using Equations 4.3 and 4.4.

$$F_{n,cell} = F_{L,cell}cos\varphi + F_{D,cell}sin\varphi \tag{4.3}$$

$$F_{t,cell} = F_{L,cell}sin\varphi - F_{D,cell}cos\varphi \tag{4.4}$$

These forces are then converted to Cartesian components $\vec{F}_i$ using Equation 4.5 [28].

$$\vec{F}_i = \begin{pmatrix} cos\alpha & -sin\alpha & 0 \\ sin\alpha & cos\alpha & 0 \\ 0 & 0 & 1 \end{pmatrix} \begin{pmatrix} F_{t,cell}\, sin\emptyset \\ F_{n,cell} \\ F_{t,cell}\, cos\emptyset \end{pmatrix} \tag{4.5}$$

Where $\vec{F}_i$ is the force of fluid acting on the blade element, therefore, $-\vec{F}_i$ is the force vector acting on the fluid, which is used in Equation 4.6 to calculate the momentum source term fed into the solver. In this equation, V_{cell} is the volume of the grid cell.

$$S_i = \frac{-\vec{F}_i}{V_{cell}} \tag{4.6}$$

This time-averaged momentum source is added to the RANS equations of the rotor region, which is discussed in detail in Section 3.2.1. The Flow field is then updated by solving conservation of mass and momentum equations for velocity and pressure. This process continues until the solution is converged.

Power extracted from the turbines is found by multiplying the time-averaged torque by rotational speed of the turbine.

4.1.2 VBM Numerical Settings

The VBM is implemented by compiling User Defined Function (UDF) files in Fluent. All solver settings and flow inputs for this simulation are the same as the ADM settings outlined in Section 3.2, with the exceptions of the VBM solver settings and momentum source input. Table 6 shows the inputs used for the VBM model setting. The UDF files are uploaded in "Cell Zone Conditions" in FLUENT for x,y,z momentum sources to calculate the momentum source terms. Refer to the VBM tutorial for detailed explanation of steps to setup the model [27].

Table 6- VBM Rotor Inputs

Number of Rotor Zones	3
Number of Blades	4
Rotor Radius [m]	2
Rotor Speed [rpm]	Varies based on TSR
Tip Effect [%]	96
Rotor Disc Pitch Angle [deg]	90
Bank Angle [deg]	0
Rotor 1 Coordinate	[0,3,2.5]
Rotor 2 Coordinate	[0,8,2.5]
Rotor 3 Coordinate	[0,13,2.5]

The reference coordinate system for the VBM simulation is based on the rotor disc configuration shown in Figure 4.3. In this configuration, flow is assumed to be in the positive x direction, and the rotor is assumed to rotate in the counterclockwise direction parallel to the xy plane. In order to match this configuration with the imported mesh coordinate system, the Rotor Disc Pitch Angle was set to 90 degrees and the Rotor

Disc Bank Angle was set to 0. These angles are not related to the blade characteristics such as twist or pitch angle, which are defined in Section 4.2.2.

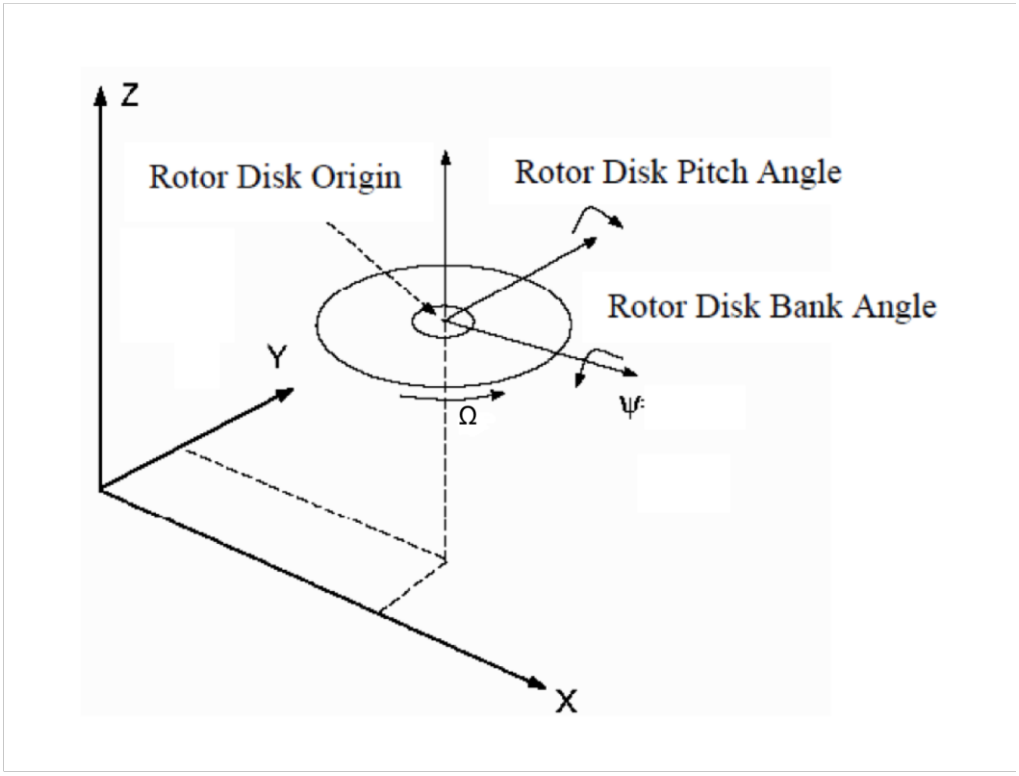

Figure 4.3-Reference Rotor Disc Configuration in VBM.

In this model, the tip effect is set to 96%, which means only 96% of blade span's lift force is taken into account and the remaining (tip region) lift force is set to 0. Alternatively, drag force is assumed to be present along the entire blade. Therefore, flow is assumed to recirculate around the region surrounding the last 4% of the blade's surface area.

4.1.3 Meshing

The same method as the one discussed in Section 3.2.3 is utilized to generate the mesh used in the VBM simulations. The only difference between the grids is the existence of a

cylinder, 0.4m in radius and 0.2m in thickness, to represent the hub of each turbine in the VBM grid. The hub is treated as an actuator disc with the inertial resistance of $C_2 = 20$.

4.2 Rotor Design

4.2.1 Airfoil Selection

Designing a HAHT utilizes a number of different basic concepts from wind turbine design. Particular differences are the Reynolds number, the stall characteristics, and the possible occurrence of cavitation [29]. The blade of a horizontal axis hydrokinetic turbine can be divided into sections along the blade, as shown in Figure 4.4.

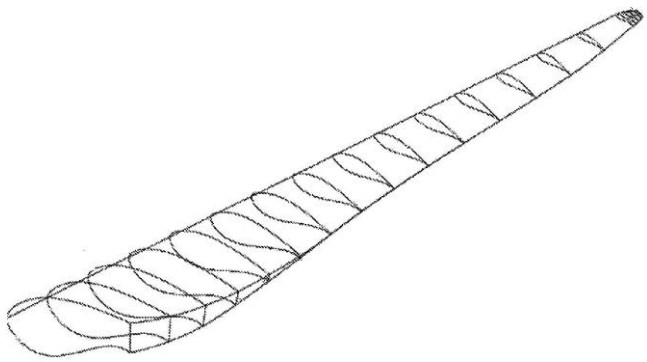

Figure 4.4- Blade Sections

The cross-section of each blade section shown in Figure 4.4 represents the airfoil design used to define the blade's geometry within the section. When a rotating airfoil is placed within a flow field with velocity U, its interaction can be visualized using Figure 4.2. In this plot, V is the relative velocity calculated using Equation 4.7 and ω is the angular velocity of turbine. Angle of attack (α) is defined as the angle between chord line and the relative velocity, angle of relative wind (φ) is the angle between relative wind and plane of blade

rotation, θ_p is section pitch angle, θ_t is section twist angle, and $\theta_{p,0}$ is the blade pitch angle at the tip.

$$V = \sqrt{U^2 + (r\omega)^2} \tag{4.7}$$

Prior to selecting an airfoil, it is important to consider hydrodynamic parameters such as lift (C_l), drag (C_d), pitch angle (θ_p), the pressure coefficient (C_p), and cavitation inception. For the case of a HAHT, it is desirable to have a high lift to drag ratio along the blade in order to maintain a high efficiency, while delaying cavitation inception as much as possible. One of the airfoils that has been used for marine turbines and is referenced in many publications is NACA 63-815. This airfoil is a modified version of NACA 63-215 with four times the camber shown in Figure 4.5. This provides for a better pressure distribution around the airfoil with respect to cavitation [30]. Increasing the camber, or the curvature, of the airfoil, reduces the minimum pressure coefficient for a given angle of attack, which is desired to delay cavitation inception, which is discussed in detail in Section 4.2.3.

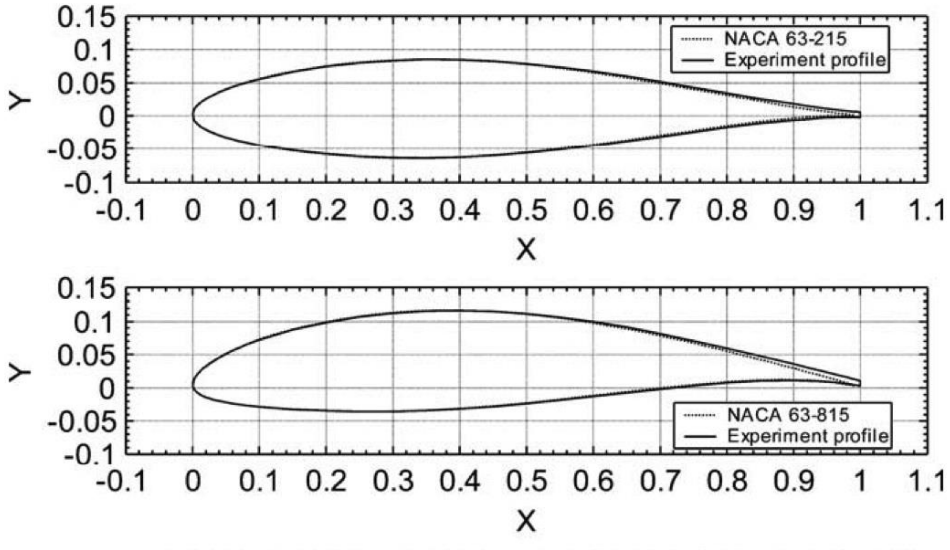

Figure 4.5- NACA 63-215 and NACA 63-215 profiles [30]

The hydrodynamic characteristics of airfoils are represented by non-dimensional lift, drag and pressure coefficients. These coefficients can be found from Equation 2.1, 4.9, and 4.10.

$$C_l = \frac{Lift\ Force\ per\ unit\ length}{Dynamic\ Force\ per\ unit\ length} = \frac{\frac{L}{l}}{\frac{1}{2}\rho U^2 c} \quad 4.8$$

$$C_d = \frac{Drag\ Force\ per\ unit\ length}{Dynamic\ Force\ per\ unit\ length} = \frac{\frac{D}{l}}{\frac{1}{2}\rho U^2 c} \quad 4.9$$

$$C_p = \frac{Static\ Pressure}{Dynamic\ pressure} = \frac{P_L - P_\infty}{\frac{1}{2}\rho U^2} \quad 4.10$$

Where L is lift force, D is drag force, l is characteristics length, P_L is the local pressure, P_∞ is ambient pressure, c is the chord length, U is the flow velocity, and ρ is the fluid density [8].

When fluid flows at an angle relative to an airfoil, it creates pressure fields on the top and bottom surfaces of the airfoil as shown in Figure 4.6. This pressure difference creates a lift force, L, which is the net normal force perpendicular to the relative wind vector. Alternatively, drag force, D, is the sum of the net force parallel to the relative wind vector and the friction forces acting in the parallel direction. These forces can be non-dimensionalized by dividing by the dynamic pressure as demonstrated in Equation 2.1, 4.9.

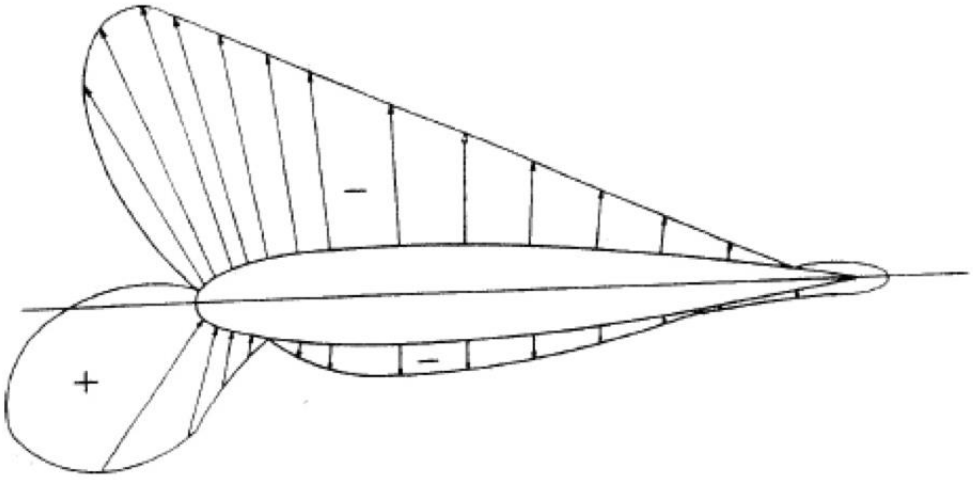

Figure 4.6- Pressure distribution around an airfoil

Bahaj et al. used cavitation tunnel experiments and XFoil simulations to determine the 2-dimentional lift, drag, and pressure coefficients for the NACA 63-815 airfoil as a function of angle of attack. Good agreement between experimental result and numerical simulations was found [30].The Lift, drag and pressure coefficients found experimentally by Bahaj are used in this thesis for cavitation analysis. Figure 4.7 shows the relation between lift coefficients and the angle of attack (α) of the NACA 63-815 airfoil. These results demonstrate that, unlike a symmetric airfoil, this cambered airfoil creates lift when the angle of attack is less than or equal to zero.

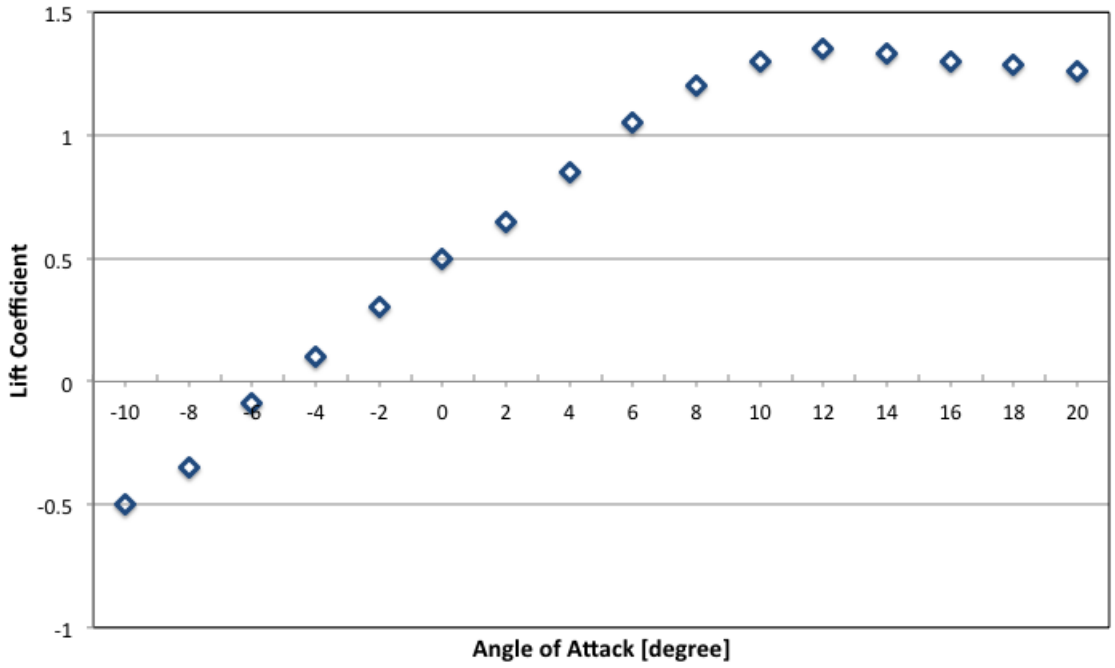

Figure 4.7- Lift coefficient versus angle of attack for NACA 63-815 airfoil [30].

When the angle of attack exceeds a certain critical value (12 degrees in this case), the airfoil stalls and the boundary layer on the upper surface begins to separate from the airfoil. This results in the formation of a recirculation region, above the airfoil, which reduces lift and increases the drag coefficients [8]. Figure 4.8 shows the relation between drag coefficient and angle of attack. These results demonstrate that, after separation occurs (above angle of attack of 12), the drag coefficient increases at a faster rate as the angle of attack continues to rise.

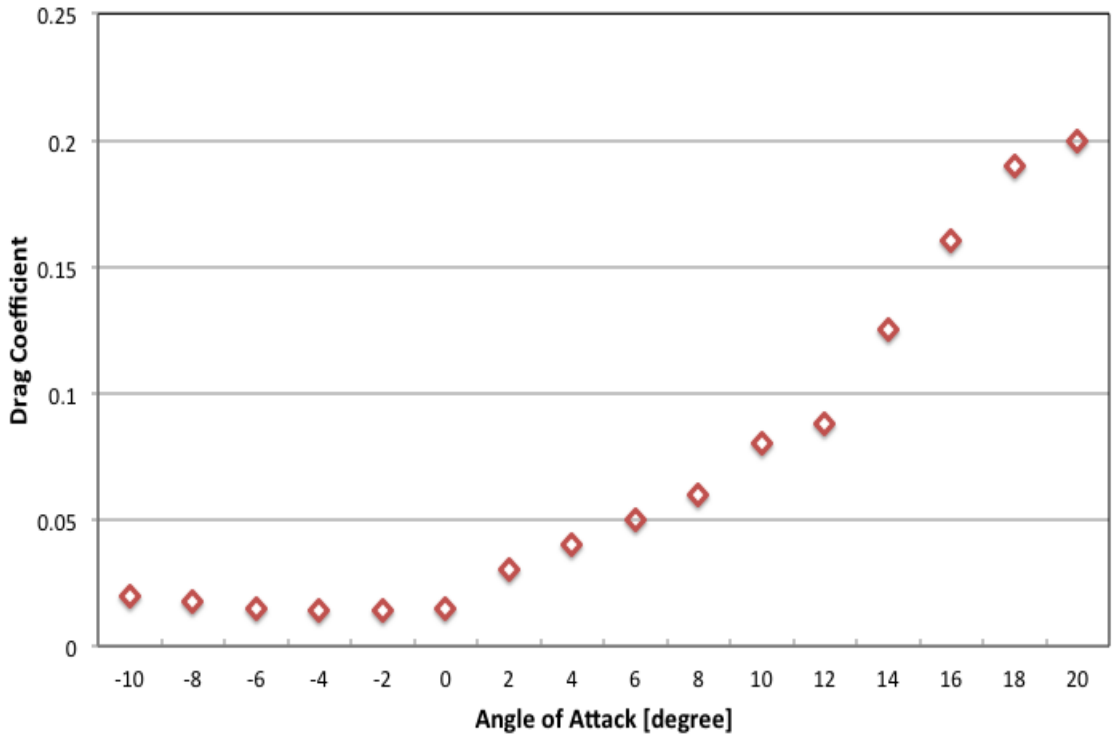

Figure 4.8- Drag coefficient versus angle of attack [30].

The pressure coefficient of a airfoil determines its performance with regard to cavitation. This coefficient is found at a given point by subtracting the local pressure from the ambient pressure, and dividing the result by the dynamic pressure, as shown in Equation 4.10. Bahaj et al. [30] provided plots of pressure coefficient around the airfoil for the following angles of attack: -5.2, -1.2, 2.8, 6.8, and 10.8. In this data, the negative minimum pressure coefficient ($-C_p$) is plotted for each of these angles of attack (Figure 4.9). This parameter plays an important role in cavitation analysis explained in the Section 4.2.3.

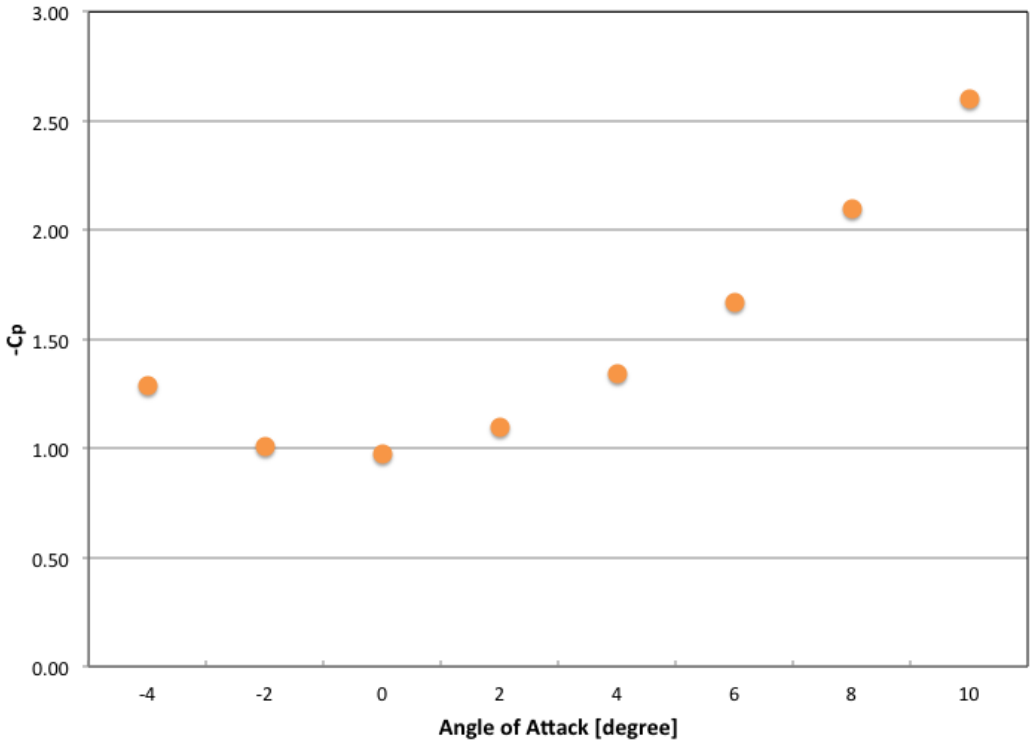

Figure 4.9- Maximum negative pressure coefficient versus angle of attack [30].

4.2.2 Blade Geometry

The Virtual Blade Model, VBM, is used in this section to assist with blade design. Initially, non-dimensional blade geometry, such as was published by Bahaj et al. [30], was used for cavitation analysis and VBM simulations [30]. However, running the VBM model with this geometry resulted in insufficient power for a turbine consisting of 3 blades. Following this discovery, a spreadsheet BET calculation was used in an iterative manner to find twist angles along the blade that produced maximum possible power. However, the calculated chord distribution for this analysis was found to be unrealistic (c >1m); therefore, several different chord distributions were developed and tested with VBM. Figure 4.10 shows three of the designs considered for the chord distribution.

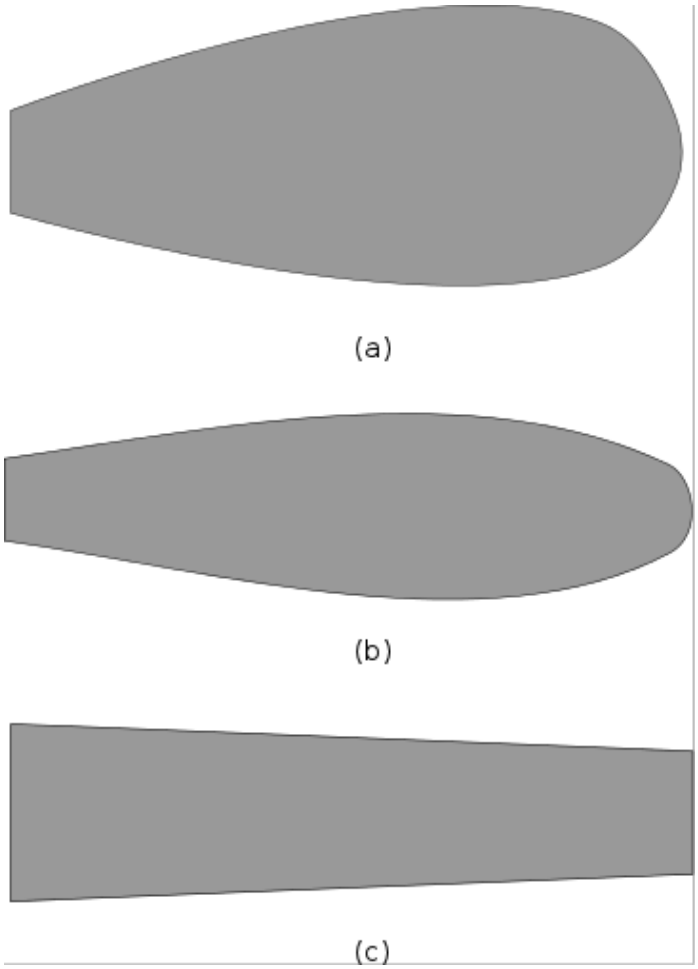

Figure 4.10- Chord distribution configurations

After running VBM simulations, it was discovered that Configuration (a) caused the flow to become restricted (choke), configuration (b) produced insufficient power, and configuration (c) gave the highest power production. Therefore, the chord distribution shown in Figure 4.10 (c) is chosen for the blades. Table 4.7 presents the non-dimensional design parameters, such as chord length and twist angle of the blade in configuration (c). The radius of the blade is 2 meters, and the chord varies from 0.5 meters at the root to 0.41 meters at the tip.

An attempt was made to optimize the turbine's design by varying the twist angle along the blade to achieve angle of attack that produces a high lift coefficient (α=7degrees). However, since flow is highly affected by the blockage, there is always a high range of angles of attack from root to tip. Therefore, no other design was found to produce significantly higher power than the one mentioned in Table 4.7.

Table 4.7- Blade Geometry

$\frac{r}{R}$	$\frac{c}{R}$	**Twist** (θ)
0.2	0.2500	27.0
0.3	0.2400	19.0
0.4	0.2350	11.1
0.5	0.2300	8.9
0.6	0.2250	7.0
0.7	0.2200	6.0
0.8	0.2100	3.0
0.9	0.2050	1.0
1.0	0.2050	0.6

4.2.3 Cavitation Analysis

Cavitation is the formation of vapor bubbles within a flowing fluid, and occurs when the pressure of the fluid falls below the vapor pressure. When this occurs, the vapor bubbles collapse and produce a shock wave. From an aerodynamic point of view, cavitation is undesirable since these strong shock waves can damage any moving object within the cavitation region [31]. Figure 4.11(a) shows the formation of vapor bubbles on the surface of an airfoil within a cavitation tunnel, and Figure 4.11 (b) shows the damage to a ship propeller due to cavitation. When cavitation occurs in the presence of an airfoil, it decreases the lift force acting on the airfoil, and increases the drag force. Therefore, it is essential to assure that the turbine operates in a cavitation-free environment.

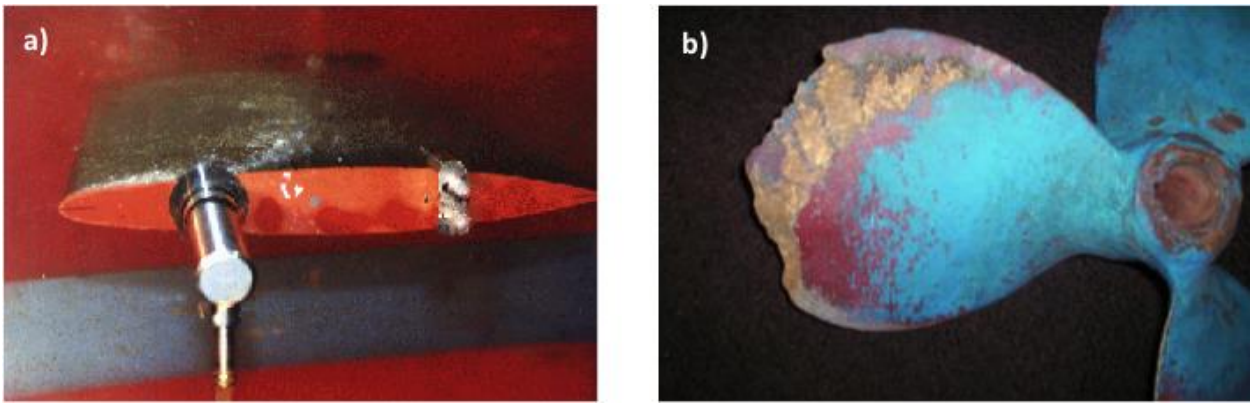

Figure 4.11- a) Bubble formation due to cavitation on a airfoil in a flume b) Damage due to cavitation on a ship propeller [32].

The cavitation inception depends upon several parameters, including the airfoil's depth of emersion, h, the relative velocity, V, and the vapor pressure, P_v. The extent to which this phenomenon occurs is quantified by a cavitation number, which can be calculated using Equation 4.11. Cavitation inception can be predicted from the pressure distribution on the airfoil since cavitation occurs when $P_L = P_v$. Upon combining Equations 4.10 and 4.11, the onset of cavitation is found to occur when the minimum negative pressure coefficient is equal to or higher than σ [29].

$$\sigma = \frac{P_{atm} + \rho g h - P_v}{\frac{1}{2}\rho V^2} \qquad 4.11$$

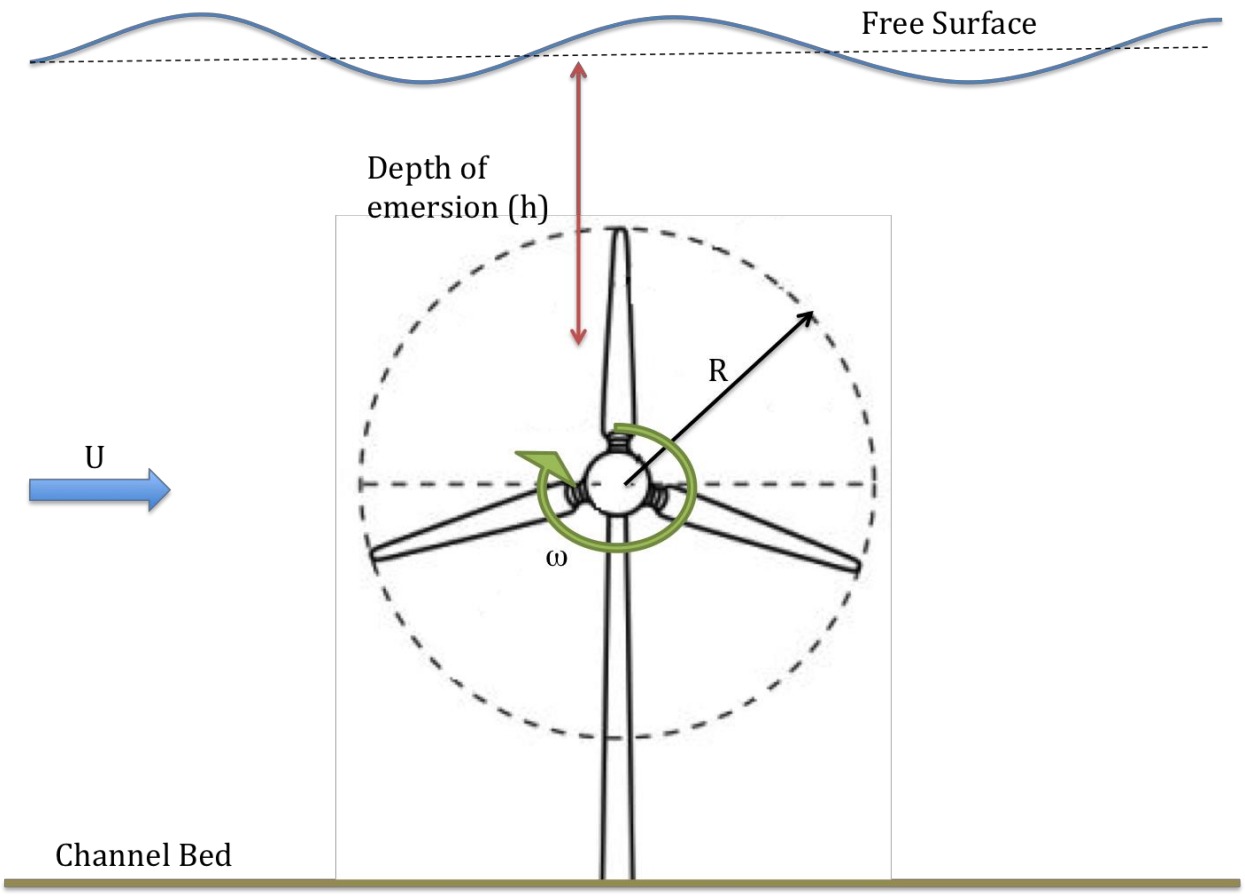

Figure 4.12- Schematic of cavitation variables

Considering that turbines operate in channels with high blockage ratios, where the free surface is near the turbine blades, it is important to perform cavitation analysis in order to understand the limits of turbine operating conditions. The Tip Speed Ratio (TSR) determines the local velocity at each blade section, which is correlated with cavitation inception. TSR is the ratio between rotational speed of the tip of the blade over the incoming velocity and is calculated using Equation 4.12.

$$TSR = \lambda = \frac{R\omega}{U} \qquad 4.12$$

where ω is the rotational speed of the turbine in $\frac{rad}{s}$.

At any given TSR, the local Reynolds number is calculated using Equation 4.13 to determine the range of Reynolds numbers at which each blade section operates. Figure 4.13 shows that the Reynolds number varies from 1e+6 to 5.3e+6 for TSR=2 to 6 for the blade selected. The published Reynolds number for the NACA 63-815 airfoil is 0.8e+6. Therefore, CFD simulations for NACA 63-815 are run to determine the lift and drag coefficients as well as the Reynolds number dependence on lift and drag coefficients. Within TSR of 1e+6 to 5.3e+6 no Reynolds number dependence was observed before stall.

$$Re = \frac{Vc}{\vartheta} \tag{4.13}$$

In this equation, ϑ is the kinematic viscosity of water and relative velocity, V, is calculated using Equation 4.7.

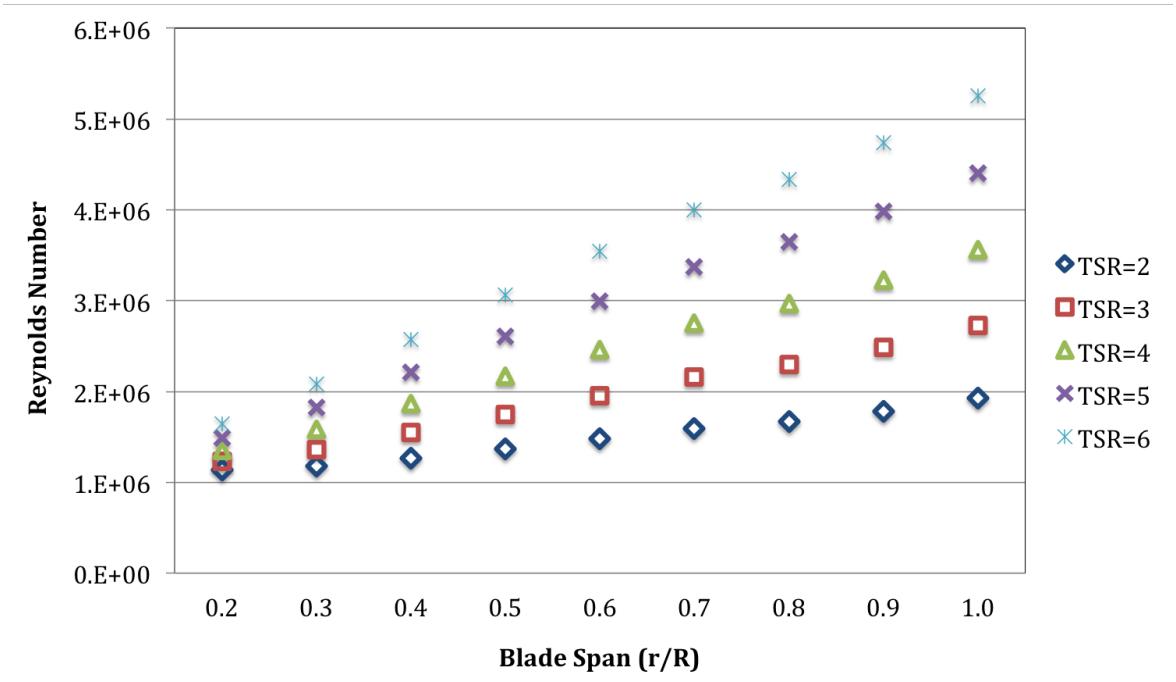

Figure 4.13- Reynolds number along blade span at different Tip Speed Ratios

Assuming that the airfoil characteristics do not show any Reynolds number dependence, experimental data at Re=0.8e+6 from Bahaj et al. [30] are used to predict cavitation inception. Based on weather data for Ephrata, WA, the highest average water temperature reaches about 30 ℃ in the months of June and July [33]. As temperature increases, the density of water decreases and the vapor pressure increases which accelerate the cavitation inception. Cavitation analysis for the worst case scenario, in which water temperatures reaches 30 ℃, are performed using Equation 4.11 and the values listed in Table 4.8

Table 4.8- Properties used in cavitation analysis at $T = 30$℃

ρ	995.7	$\frac{kg}{m^3}$
ϑ	$0.8\,e-6$	$\frac{m^2}{s}$
P_{atm}	101320	pa
P_v	4266	pa

At the tip of the turbine, the water velocity is 1.685 $\frac{m}{s}$, upstream water depth is 4.937 m, and depth of emersion is 0.437 m. The cavitation number is calculated along the span of the blade for several TSRs as presented in Figure 4.14. These calculations led to the observation that cavitation number is lowest at the tip, and thus, this region is more susceptible to cavitate. The depth of emersion increases from tip to root and the local velocity decreases, which delays cavitation inception.

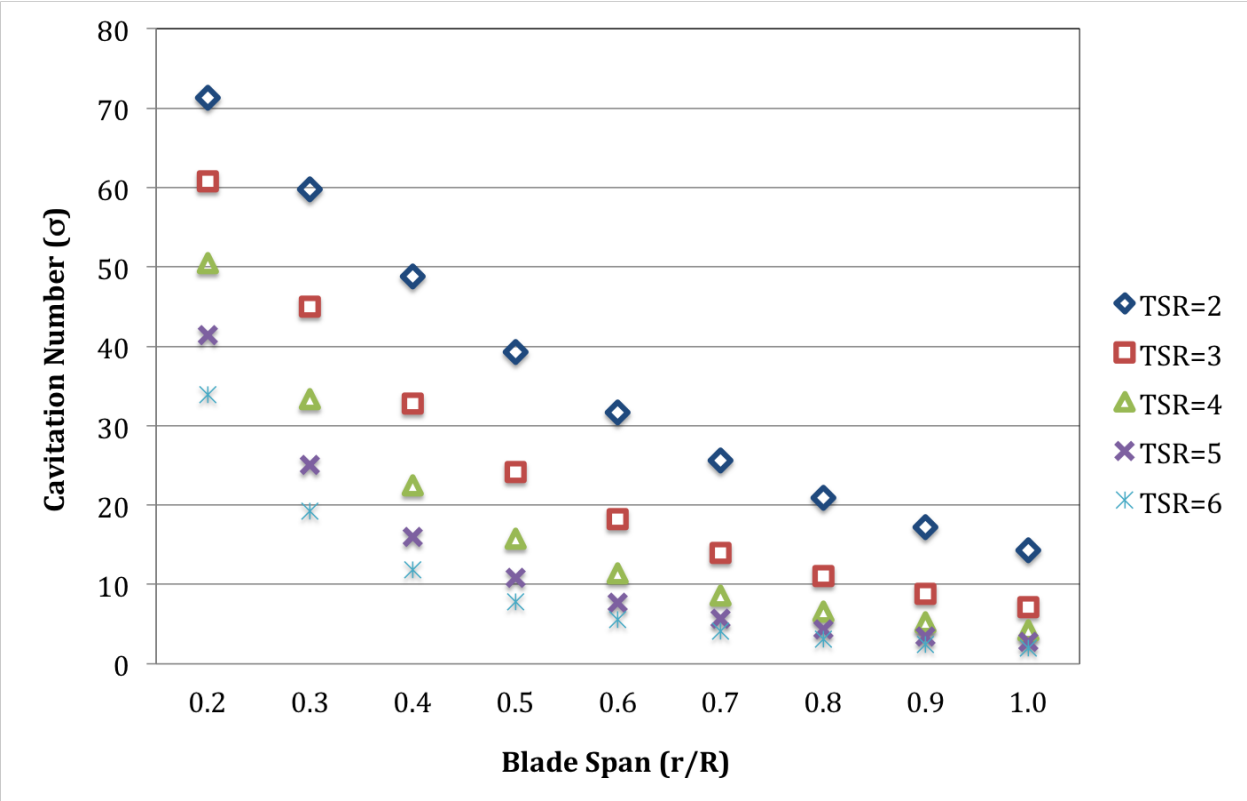

Figure 4.14- Cavitation number versus the span of the blade positioned perpendicular to surface

4.2.4 Operating Limits

Based on Figure 4.14, it is reasonable to assume that should cavitation occur at a particular TSR, it will occur within the tip section of the blade. The cavitation number at the tip of the blade is found for several different angles of attack. The relative angle and relative velocity are found using Equation 4.14 and 4.15 respectively using airfoil geometry shown in Figure 4.2.

$$\varphi = \alpha + \theta_p \tag{4.14}$$

$$V = \frac{R\omega}{\cos(\varphi)} \tag{4.15}$$

As TSR increases, cavitation number decreases and gets closer to the minimum pressure coefficient, which increases the chance of cavitation. At a TSR of 6, cavitation numbers at different angles of attack are close to the $-C_p$ curve and cavitation is expected for $\alpha > 6$ degrees. Based on Figure 4.15, if the angle of attack at the tip reaches above 10 degrees at a TSR of 5, cavitation is likely to occur.

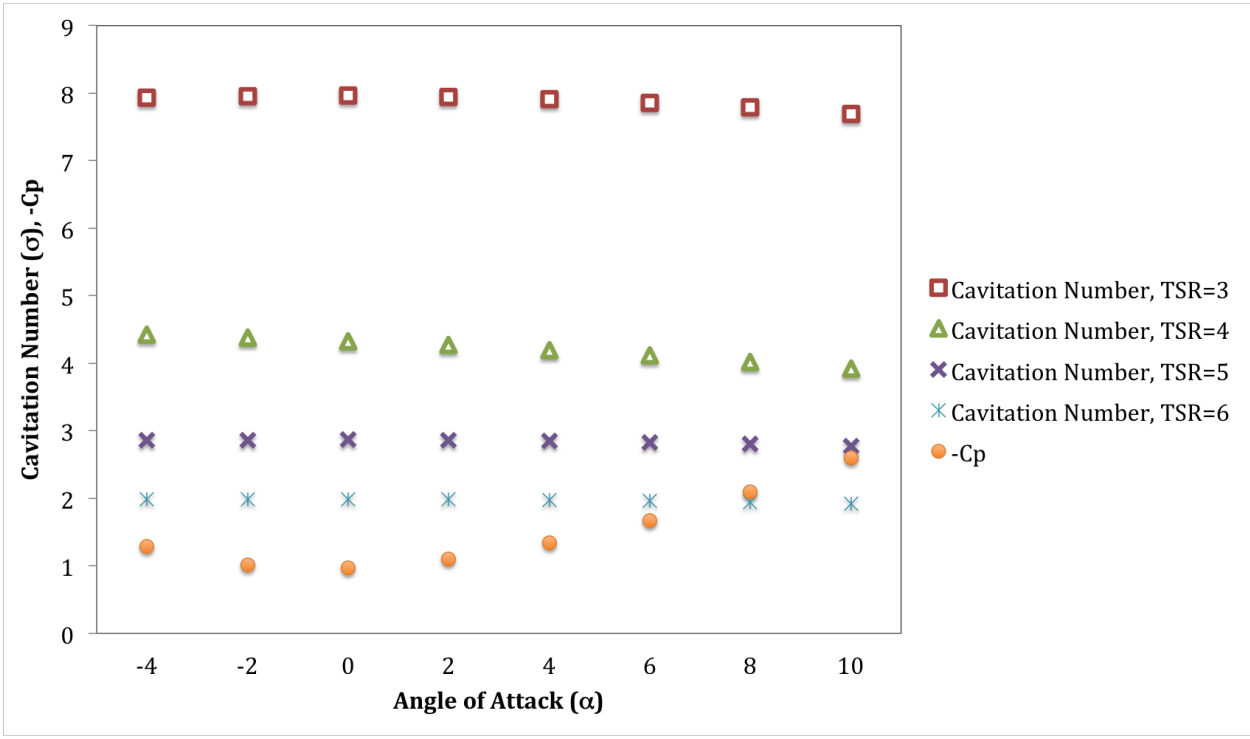

Figure 4.15- Cavitation Number and minimum negative pressure coefficient versus angle of attack (at $\theta_p = 0$).

Once the operating range of TSRs is found, it is necessary to determine how much pitch angle could be applied to the blade at the tip, $\theta_p = 0$, before cavitation occurs. Table 4.9 presents the allowable blade pitch angle at the tip at angles of attack between -4 and 10 degrees. Here, green indicated allowable angles, while red indicates the anticipation of cavitation at a TSR of 5.

Table 4.9- Cavitation number at several angles of attack and pitch angle for TSR=5 while twist at the tip is 0.6 degrees.

$\alpha/\theta_{p,0}$	**-5**	**0**	**5**	**10**
-4	2.79	2.86	2.83	2.78
-2	2.82	2.87	2.80	2.74
0	2.84	2.87	2.77	2.69
2	2.86	2.86	2.73	2.64
4	2.86	2.85	2.68	2.58
6	2.87	2.83	2.63	2.51
8	2.86	2.80	2.58	2.44
10	2.85	2.77	2.51	2.37

4.3 VBM Results

Since the 16 meter wide channel with the blockage ratio of 0.48 provides for a higher power extraction of turbines and head loss from the flow compared to the 21m wide channel, VBM simulations are only run for the 16m wide channel. TSRs of 3.5 and 5 are used in these simulations while varying blade pitch angle at the tip from -5 to 10. Power extraction by turbines, power dissipation from the flow due to extracted power and wake loss, and surface drop behind the turbines are analyzed for all these cases.

4.3.1 Flow field and surface elevation

As mentioned in Section 4.2.2, the turbine is optimized at TSR=5 and $\theta_{p,0} = 0$. The plots shown in this section are going to present only the optimized case.

Figure 4.16 shows the top view of the velocity contour for the optimized case. This figure shows that velocity at the tip location behind the turbine is lower than velocity behind the other sections. This is due to higher local velocity, V, at the tip and consequently higher power extraction by these sections.

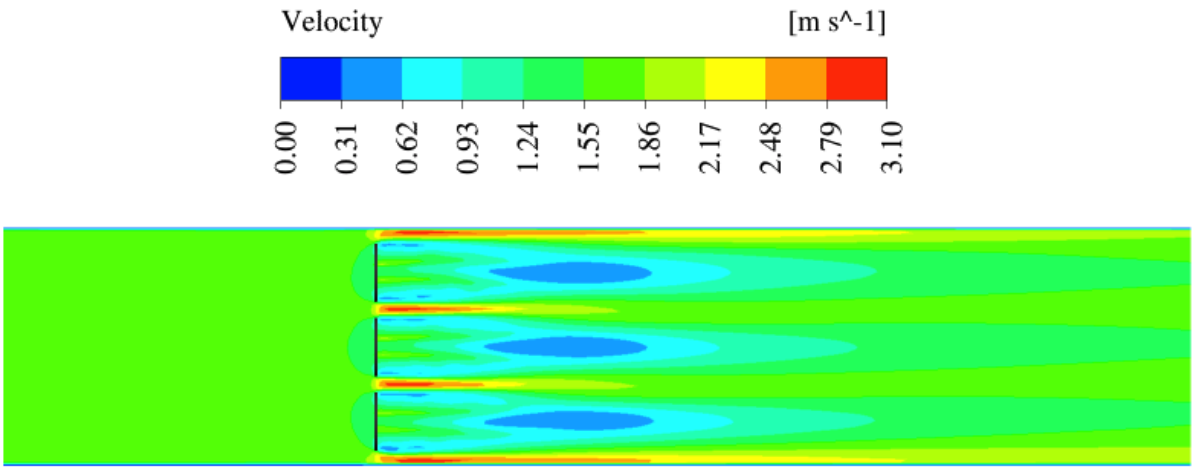

Figure 4.16- Top view velocity contour plot of the optimized turbine design (TSR=5 and $\theta_{p,0} = 0$) at the plane passing through the center of turbine.

Normalized depth is plotted in Figure 4.17 versus normalized velocity at 5D upstream, and at 5D, 10D, and 15D downstream of the middle turbine in the 16m wide channel using VBM. The blockage effects is observed more near the channel bed than the free surface. Flow velocity is about 1.17 times faster than the free stream velocity near the channel bed 5D downstream of the turbine. This value is about 0.92 when ADM is used. The rotational velocity produced by the VBM may have caused this difference in the normalized velocity downstream of the turbine near the channel bed.

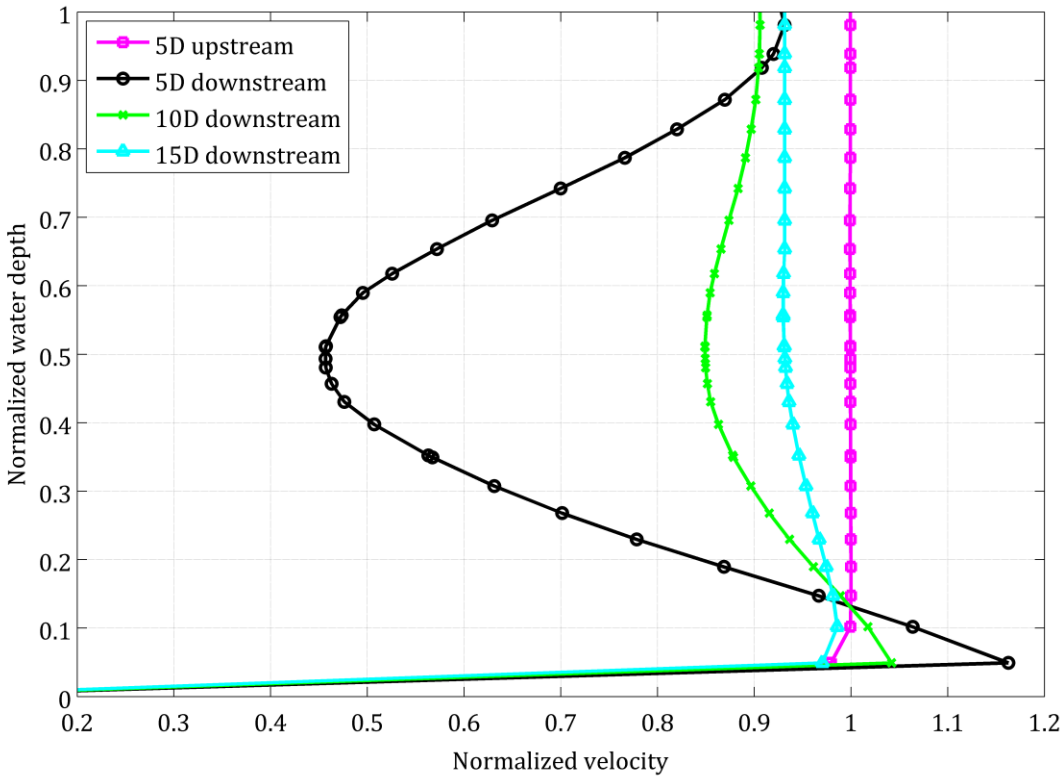

Figure 4.17- Normalized depth vs normalized depth 5D upstream, 5D, 10D, and 15D downstream of the turbines.

The dynamic pressure plot provided in Figure 4.18 shows that the wake of the turbine is affected by the elevation drop at the free surface.

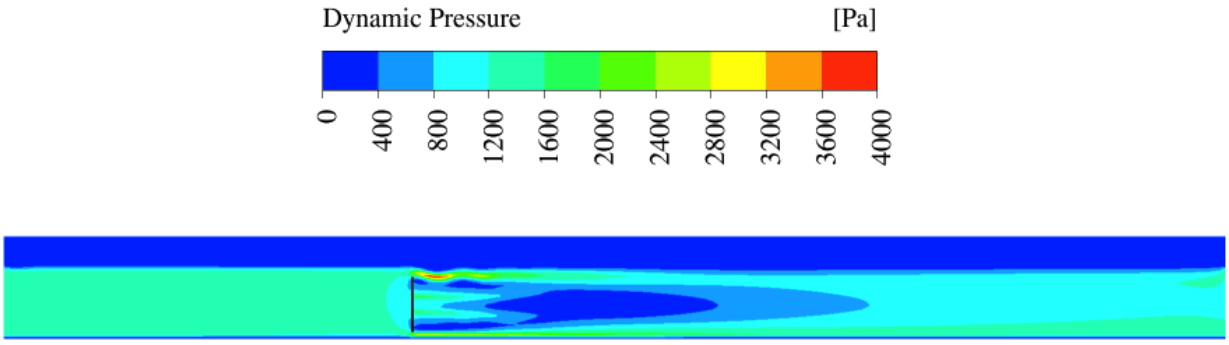

Figure 4.18-Dynamic pressure plot using VBM for the optimized case.

Normalized minimum surface elevation behind the turbine ($\frac{h_3}{h_0}$) and normalized surface elevation 15D downstream of the turbines ($\frac{h_5}{h_0}$) are plotted over a range of blade pitch angle at the tip in Figure 4.19 for TSR of 5 and 3.5. Higher surface drop and head loss are observed in most operating conditions for a TSR of 5 compared to a TSR of 3.5. The flow depth decreases between 2% to 4% of its initial depth when the turbines operate at conditions mentioned in this figure.

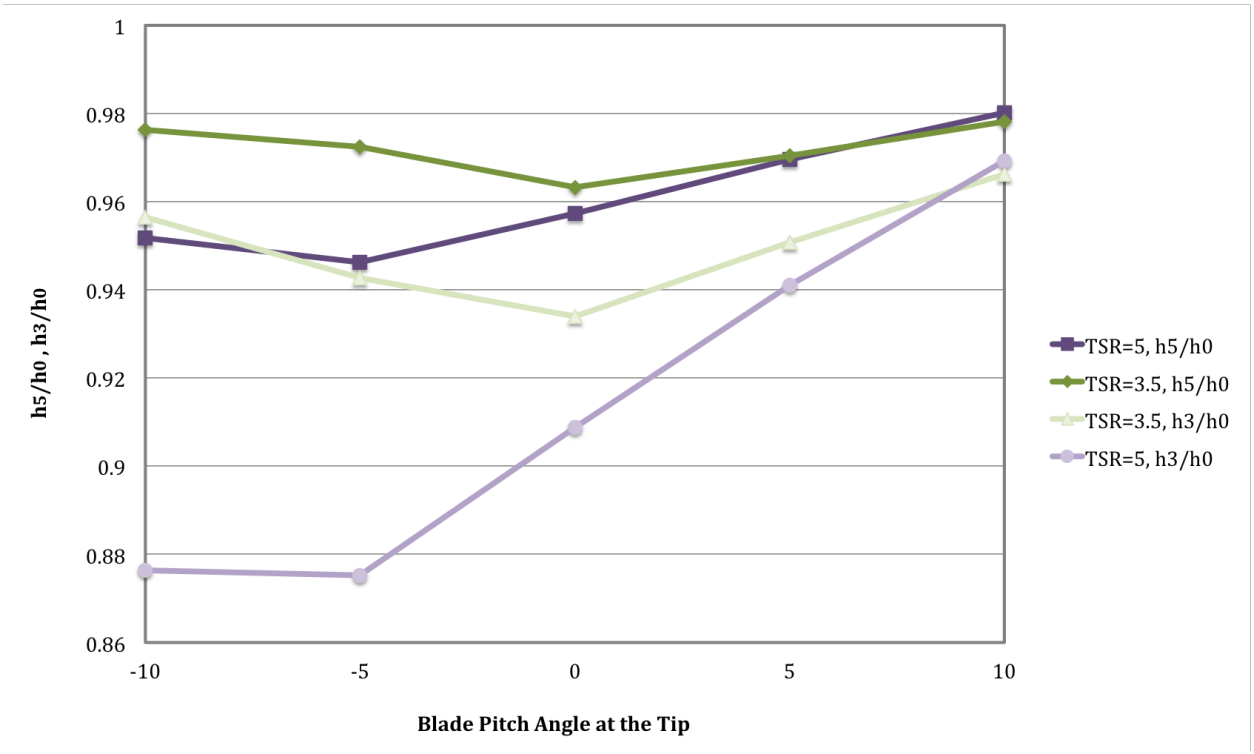

Figure 4.19- Normalized surface elevation behind the turbine at lowest free-surface elevation and at 15D downstream of the turbines at TSR=3.5 and 5.

4.3.2 Power extraction and dissipation

The VBM is capable of reporting power extracted by each of the turbines and the minimum and maximum angles of attack along the blades. Power extraction efficiency for cases with

the two TSRs and various pitch angles are calculated from Equation 4.16. At both TSRs, power coefficient, or power extraction coefficient, is higher than the Lanchester-Betz limit due to the confining effects of the channel and free surface as shown in Figure 4.20.

$$C_p = \eta_e = \frac{\mathrm{P}_{extracted}}{\frac{1}{2}\rho A_t {u_0}^3} \qquad 4.16$$

In this equation, A_t is the area of the turbines. The highest power is produced at the optimized design case (TSR=5 and $\theta_{p,0} = 0$), which is about 94 kW for the array of three turbines. At any blade pitch angle less than 0, the angle of attack on several sections of the turbine blades increases This causes the blades to stall and decreases the power extraction by the turbines. Once $\theta_{p,0}$ is increased from where maximum power is extracted, the angle of attack decreases; therefore, not enough lift force is produced on blades sections. In such a condition, power extraction of the turbines also decreases. The same principle holds when turbines run at TSR=3.5, except maximum power extracted from the turbines is about 75kW at $\theta_{p,0} = 5$.

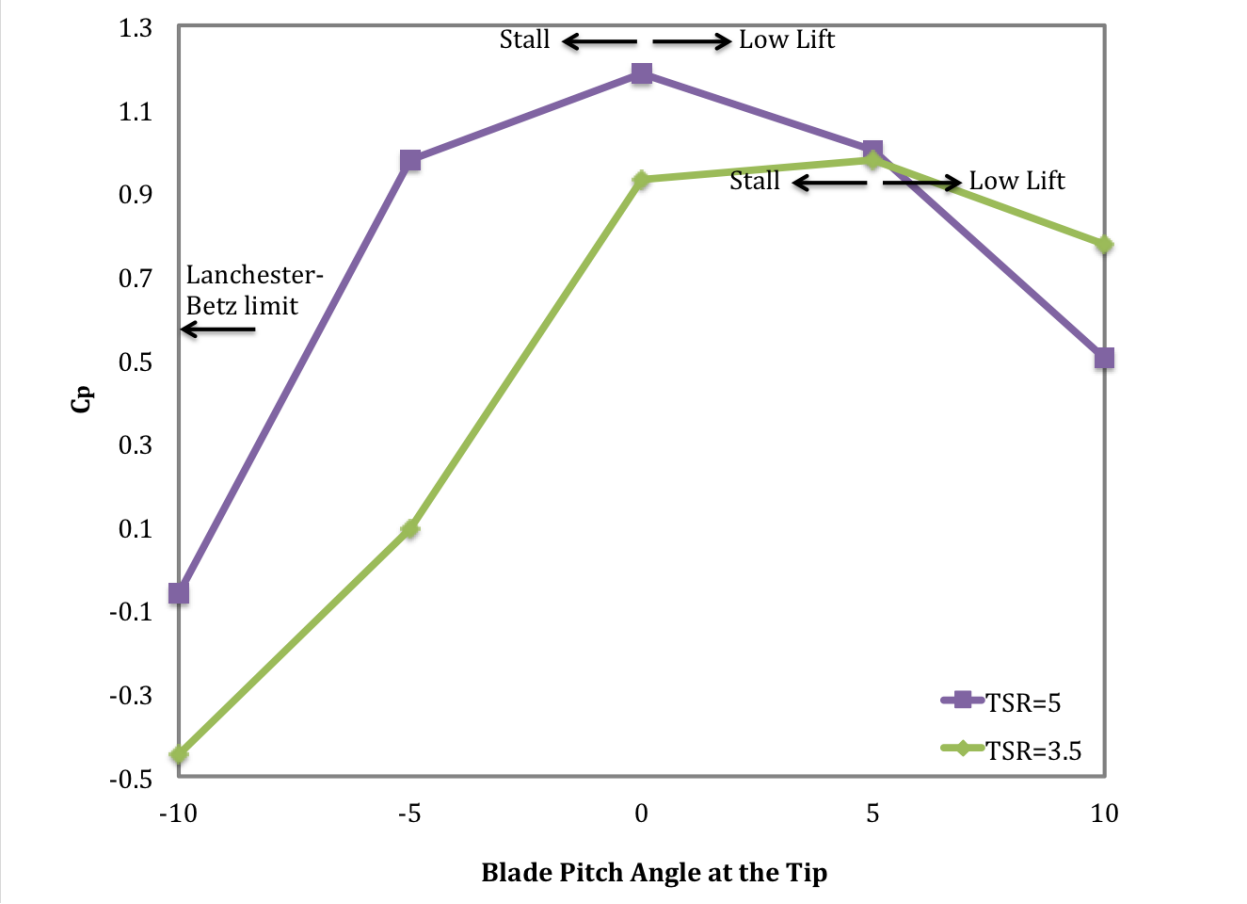

Figure 4.20- Power coefficient at TSR=5 and 3.5.

In order to investigate the total power removed from the flow, the power dissipation efficiency is calculated from Equation 4.17 for all cases as presented in Figure 4.21.

$$\eta_d = \frac{\mathrm{P}_{dissipated}}{\frac{1}{2}\rho A {u_0}^3} \qquad 4.17$$

In this equation, A is the cross-sectional area of the channel and $\mathrm{P}_{dissipated}$ is calculated by subtracting potential and kinetic power of the flow at the outlet from the inlet flow as shown in Equation 4.18.

$$\mathrm{P}_{dissipated} = (\dot{m}gh + \frac{1}{2}\dot{m}u_0^2)_{outlet} - (\dot{m}gh + \frac{1}{2}\dot{m}u_0^2)_{inlet} \qquad 4.18$$

Highest power dissipation is achieved when some sections of the blades stall while other sections produce high lift. Highest power dissipation for the three turbines, is about 360kW at TSR=5 and $\theta_{p,0} = -5$ and 285kW at TSR=3.5 and $\theta_{p,0} = 0$. Therefore, in order to achieve the goal of dissipating 1MW of power, four arrays of three turbines would need to be installed about 15D downstream of each other. Operating the turbines at the different conditions mentioned in this section, could provide control of the flow at the desired flow head.

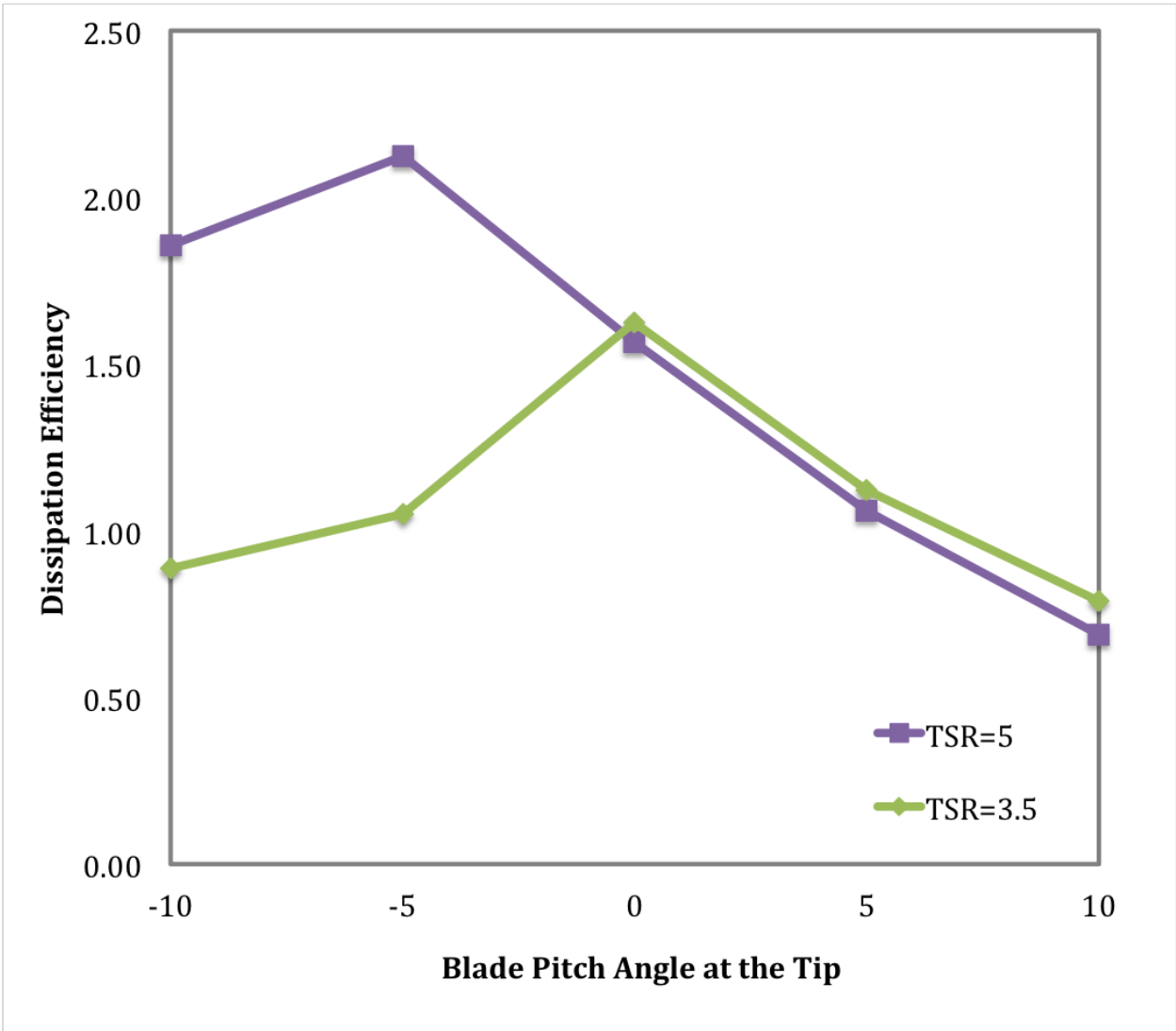

Figure 4.21- Total power dissipation efficiency versus blade pitch at the tip for TSR of 3.5 and 5.

4.4 Comparison between VBM and ADM results

The main difference between the VBM and ADM is the way they are defined as momentum source terms. The ADM uses a porous media with a homogenous force applied to its surface area. The VBM is a more advanced model that takes the geometry of the blade and rotational speed of the rotor into account. To compare VBM to ADM and one-dimensional theory, the VBM is used to calculate parameters such as induction factor and thrust coefficient of the turbines at desired TSR and $\theta_{p,0}$. Thrust coefficient is found using Equation 4.19. Induction factor is used to calculate useful power extraction by turbines and power dissipation from the flow using the one-dimensional theory. Induction factor and thrust coefficient are used to calculate the pressure drop across the discs and consequently the inertial resistance, C_2 for the ADM.

$$c_t = \frac{\text{Thrust}}{\frac{1}{2}\rho A {u_0}^2} \tag{4.19}$$

To compare the power extracted by the turbine and total power removed from the flow, power coefficient and dissipation coefficient are calculated from Equation 4.16 and Equation 4.20 respectively.

$$C_{dissipated} = \frac{\mathrm{P}_{dissipated}}{\frac{1}{2}\rho A_t {u_0}^3} \tag{4.20}$$

In this equation A_t refers to the area of the turbines. It should be emphasized that unlike Section 4.3.2, $P_{dissipated}$ is normalized by the kinetic power crossing the turbine instead of kinetic power of the incoming flow through the inlet of the channel. The reasoning behind this method for normalizing $P_{dissipated}$ is that previous method using Equation 4.17 provides incomparable efficiency to compare to power coefficient since the area used to normalize the power is different for each method.

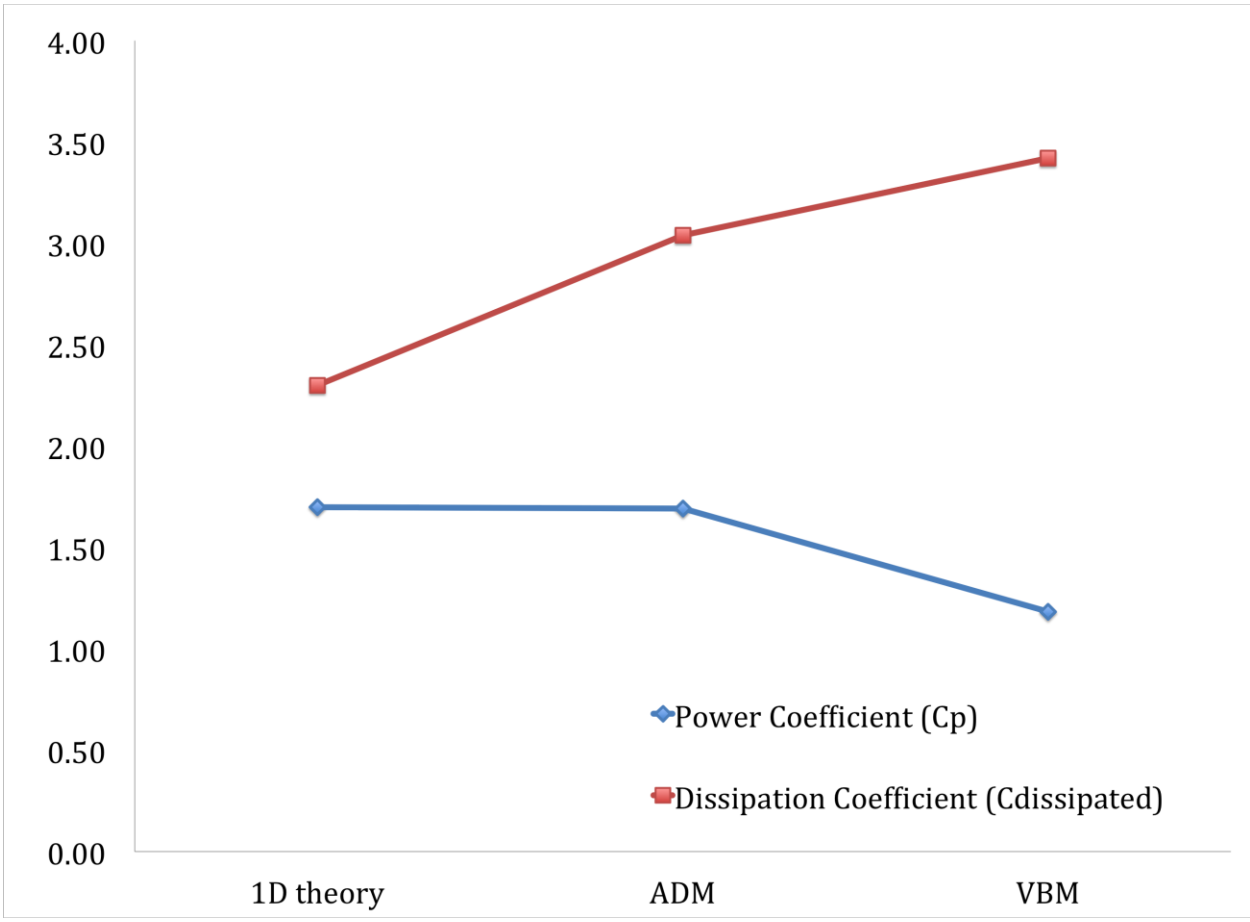

Figure 4.22- Comparison between one-dimensional theory, ADM and VBM for Power Coefficient and Dissipation Coefficient at TSR=5 and $\theta_{p,0} = 0$.

The one-dimensional theory and ADM over predicted the extracted power compared to the VBM as shown in Figure 4.22. Both one-dimensional theory and ADM use the pressure drop

across the turbine to find power extracted by turbines, whereas, power is calculated by the time-average torque multiplied by the rotational speed of the turbines in VBM. The simplification used in calculations of power using one-dimensional and ADM results in about 40% over prediction of power extracted by the turbines. The VBM provides a more realistic power extraction by turbines since it takes into account the hub of the turbine and the tip effects.

The total power dissipated from the flow is under predicted using the one-dimensional theory and ADM compared to VBM. Power extraction using one-dimensional theory is due to useful power extracted by the turbines and power dissipation of the mixing region. ADM includes these losses in addition to wake rotation. The power dissipated using VBM model includes the losses due to useful power extraction of turbines, mixing of wake with bypass flow, drag forces of the turbine, mixing of the rotational flow field generated based on geometry of the turbines in addition to the wake rotation.

Chapter 5
Conclusions

Open Channel Flows such as flows in irrigation canals and constructed channels are good candidates to produce small-scale hydrokinetic power. Traditionally, gates are used to control water flow in such waterways by dissipating kinetic energy of the flow. Horizontal Axis Hydrokinetic Turbines (HAHT) are good candidates to replace these traditional gates to extract power from the flow in terms of useful power and control the flow.

5.1 Summary of models

Theoretical and numerical approaches are used to model HAHTs in open channel flows. The theoretical method uses one-dimensional control volume analysis to predict maximum power that an ideal rotor can extract from the flow as useful power and as wake mixing loss at a given Froude number and blockage ratio. This method is then compared to the three-dimensional Actuator Disc Model (ADM) developed in the commercial Computational Fluid Dynamic (CFD) code ANSYS Fluent. This model uses a porous media to represent the HAHTs and Reynolds-Average Navier-Stokes (RANS) equations along with the Volume of Fluid (VoF) model to solve for the flow field and track the free surface. Then the same computational modeling is implemented with a more advanced model, the Virtual Blade Model (VBM), which uses Blade Element Theory (BET) to consider geometry of the blades and operating conditions such as the Tip Speed Ratio (TSR) and blade pitch angle. This method is used to optimize the turbine geometry for maximum power and to find operating limits to avoid blade cavitation.

5.2 Summary of the blockage effects on the extracted power by turbines

The presence of a free surface and channel walls creates a higher blockage ratio for HAHTs than for turbines in tidal channels. It is found that turbines extract more power as blockage ratio increases using ADM. At a mass flow rate of 132,850 $\frac{kg}{s}$, an array of three turbines, 4 meters in diameter, produces 3 times more power when the blockage ratio is 0.48 and Froude number is 0.24 compared to the case when the blockage ratio is 0.36 and Froude number is 0.18. In this case, extraction efficiency, C_p is 1.5 times higher for the case with higher blockage.

Tracking the free surface using the VOF model is important in predicting power extraction of turbines in high blockage ratios. Power extraction by turbines is under predicted when the free surface is not included in the simulation (by using a lid as the top boundary condition in the computational domain, while maintaining the desired blockage ratio). The under prediction of power extraction increases, as blockage ratio is raised (i.e. power is under predicted by 12% when BR=0.48 and 7% when BR=0.36).

Flow is only locally induced at the turbines for high blockage ratios (i.e. BR=0.48). The lower blockage case (i.e. BR=0.36) shows an array induced velocity in addition to the velocity induction at individual turbines. An array wake is also observed for the lower blockage case.

It is important to study the wake of HAHTs in order to investigate the placement of arrays of turbines in the channel. Wake recovery is faster for the flow when the blockage ratio is high compared to the flow at a lower blockage. This tendency appears to be caused by the

higher velocity through and around the turbines when blockage ratio is high. This enhances the mixing of fast and slow moving flows behind the turbine in near and far wake regions.

5.3 Summary of the blockage effects on the free surface deflection and the total dissipated power from the flow

Turbines extract more power in a channel with higher blockage ratio. Consequently, a higher free surface drop behind the turbines occurs for the flow in a higher blockage ratio flow compare to a lower blockage ratio flow. The flow depth far downstream of the turbines normalized by upstream depth is lower for the higher blockage case (BR=0.48) compared to the lower blockage ratio (BR=0.36).

The total power dissipated from the flow in the one-dimensional and ADM cases is due to the power extraction of the flow by turbines and mixing of the slow moving flow behind the turbine and fast moving water around the turbines, while losses due to wake rotation is neglected. Higher total power is dissipated from the flow at higher blockage ratios. This is due to higher power extraction by the turbines and higher shear between the fast and slow moving water behind the turbines at the higher blockage ratios compared to lower blockage ratios.

5.4 Summary of comparison between three models

The VBM is used to calculate parameters such as induction factor and thrust coefficient of the turbines at desired Tip Speed Ratio (TSR) and blade pitch. These parameters are used to find power extraction and power dissipation coefficients using the one-dimensional theory and ADM and to compare to VBM results.

The one-dimensional theory and ADM over predict the extracted power compared to the VBM. Both one-dimensional theory and ADM use the pressure drop across the turbine to find power extracted by turbines, whereas, power is calculated by the torque multiplied by the rotational speed of the turbines in VBM. The simplification used in calculations of power using one-dimensional and ADM results in about 40% over prediction of power extracted by the turbines.

The total power dissipated from the flow is under predicted using the one-dimensional theory and ADM compared to VBM. This under prediction is due to neglecting the wake rotation of the flow created by the rotational velocity field produced at the turbine.

5.5 Future work

The literature lacks the experimental data for power extraction of HAHTs in high blockage ratio flows. Experiments must be performed using the designed turbine to validate the three-dimensional numerical and one-dimensional theoretical results. A new set of boundary condition must be developed in Fluent so that the inlet water depth can be fixed. This ensures the correct inlet velocity and consequently the correct velocity at the turbines.

Appendix A

A.1 Open Channel Flow Analysis

Open Channel Flow (OCF) is referred to the study of the fluid flow in conveyances where flowing fluid forms a free surface and is driven by gravity. The forces causing and resisting motion along with the inertia must form a balance such that free surface is a streamline along with the pressure is constant and equal to atmospheric pressure [34]. The most important dimensionless number in OCF calculations is Froude number, which is the ratio of inertia to gravity forces and it can be calculated from Equation A.1

$$Fr = \frac{U}{\sqrt{gy}} \tag{A.1}$$

In this equation, U is the free stream velocity, g is the gravitational force, and y is the incoming water depth. The flow is called subcritical if Fr<1 and supercritical if Fr>1. Supercritical condition occurs if flow velocity is higher than the celerity of a small surface disturbance. Therefore, any disturbances can only move downstream. However, flow velocity is lower than wave speed, which implies disturbances can move upstream or downstream.

Supercritical flow is not stable and tends to convert to subcritical. This transition occurs through a hydraulic jump where an abrupt change from high velocity (supercritical regime) to a low velocity (subcritical regime) open channel flow. This process is accompanied by a significant energy loss due to interaction of strong turbulent rollers with free surface leading to air entrainment, vortices, kinetic energy dissipation, and a bubbly two-phase flow structure [7].

Hydraulic jumps are common after hydraulic structures such as gates and stilling basins. Flow properties can be solved using control volume analysis of continuity and momentum balances.

Considering a known gate opening, w, Trunnion pin height of, a=4.57m, gate radius of, r=5.85, the energy dissipated by these gates can be calculated based on upstream flow conditions. Figure 5.1 shows the schematic of a Tainter gate.

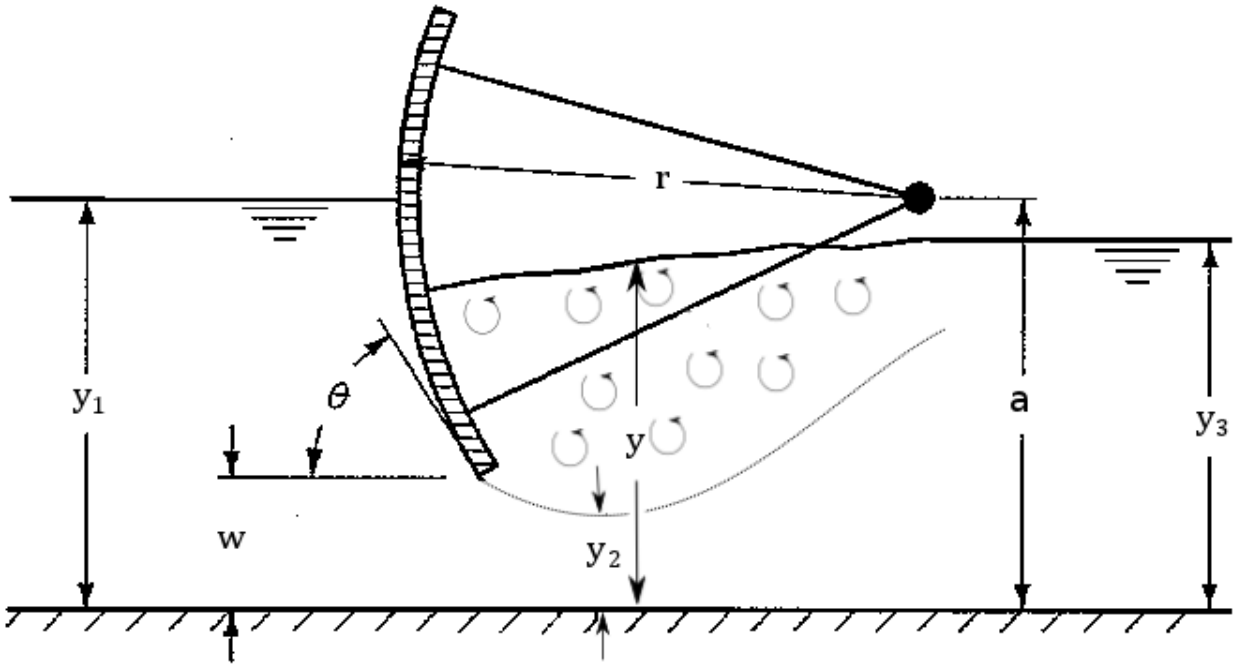

Figure 5.1-Tainter gate

The gate angle, θ, is found from:

$$\theta = \cos^{-1}\left(\frac{a-w}{r}\right)\frac{1}{90} \qquad \text{A.2}$$

The location of the lowest water depth is called Vena Contracta and it can be found using Equation A.3.

$$y_2 = (1 - 0.75\theta + 0.36\theta^2)w \quad \text{A.3}$$

Assuming that the flow pass the gate is submerged, submerged water depth, y can be found using conservation of energy from upstream to the Vena Contracta from Equation A.4 water outflowing the gate with the depth of y_2, and part by stagnant water with depth of y. While there may be some energy loss between sections 1 and 2, much higher energy is dissipated when the flow expands from sections 2 to 3 [35]. Therefore, energy loss is neglected between section 1 and 2.

$$y_1 + \frac{q^2}{2gy_1^2} = y + \frac{q^2}{2gy_2^2} = y + \frac{{u_2}^2}{2g} \quad \text{A.4}$$

Where $q = \frac{Q}{b} = u_1 y_1$ is the discharge per unit width of the channel. Once y_2 and u_2 are known, Froude number can be found at Vena Contracta.

$$Fr_2 = \frac{u_2}{\sqrt{gy}} \quad \text{A.5}$$

If $Fr_2 > 1$, the flow becomes supercritical and would go through a hydraulic jump to become stable. Conservation of momentum from Vena Contracta to the downstream of the gate can be used to solve for y_3.

$$\frac{q^2}{gy_2} + \frac{y^2}{2} = \frac{q^2}{gy_3} + \frac{y_3^2}{2} \quad \text{A.6}$$

Head loss of the flow can be found using the energy balance of the upstream to downstream of the gate as presented in

$$H_L = y_1 - y_3 + \frac{{u_1}^2}{2g} - \frac{{u_3}^2}{2g} \quad \text{A.7}$$

Head loss varies for different gate openings. As gate is lowered, velocity of water at Vena Contracta becomes higher and energy dissipation within the hydraulic jump increases. Power dissipation at different gate openings is provided in Figure 1.4. As an example, gate opening of 2m dissipates about 1MW of power. Even for cases that Fr_2 is less that 1, high power dissipation is observed due to mixing of high speed flow at Vena Contracta and slow moving water around and downstream of the gate.

Bibliography

[1] Kenny, Joan, Barber, Nancy, Hutson, Susan, Linsey, Kristin, Lovelace J., 2009, Estimated Use of Water in the United States in 2005 Circular 1344, Reston, Virginia.

[2] 2000, Irrigation and water resources in Latin America and the Caribbean.

[3] Agency E. E., 2009, Water resources across Europe — confronting water scarcity and drought.

[4] Barton A., "Water in Crisis- Middle East."

[5] 2012, MEMORANDUM OF UNDERSTANDING FOR HYDROPOWER.

[6] "US Bureau of Reclamation/ Columbia Basin Project" [Online]. Available: http://www.usbr.gov/projects/Project.jsp?proj_Name=Columbia Basin Project.

[7] Murzyn, Fredric, Chanson H., 2007, Free Surface, Bubbly Flow and turbulence measurements in hydraulic jumps.

[8] Manwell, J.F, McGowan, J.G, Rogers A. ., 2006, Wind Energy Explained, Wiley, Amherst, USA.

[9] Harrison M. E., Batten W. M. J., Myers L. E., and Bahaj a. S., 2010, "Comparison between CFD simulations and experiments for predicting the far wake of horizontal axis tidal turbines," IET Renewable Power Generation, **4**(6), p. 613.

[10] Garrett C., and Cummins P., 2007, "The efficiency of a turbine in a tidal channel," Journal of Fluid Mechanics, **588**, pp. 243–251.

[11] Polagye B., 2009, "Hydrodynamic Effects of Kinetic Power Extraction by In-Stream Tidal Turbines," University of Washington.

[12] Corten G. P., 2000, "Heat Generation by a Wind Turbine," 14th IEA Symposium on the Aerodynamics of Wind Turbines, pp. 1–8.

[13] Whelan J. I., Graham J. M. R., and Peiró J., 2009, "A free-surface and blockage correction for tidal turbines," Journal of Fluid Mechanics, **624**(March 2009), p. 281.

[14] Batten W. M. J., Harrison M. E., and Bahaj a S., 2013, "Accuracy of the actuator disc-RANS approach for predicting the performance and wake of tidal turbines.," Philosophical transactions. Series A, Mathematical, physical, and engineering sciences, **371**(1985), p. 20120293.

[15] Macleod A. J., 2002, "Wake effects in tidal current turbine farms," Proceedings of MAREC Conference, Newcastle.

[16] Bahaj A. S., Myers L. E., Thomson M. D., and Jorge N., 2007, "Characterising the wake of horizontal axis marine current turbines," Proceedings of the 7th European Wave and Tidal Energy Conference, Porto, Portugal.

[17] Myers L. E., and Bahaj a. S., 2010, "Experimental analysis of the flow field around horizontal axis tidal turbines by use of scale mesh disk rotor simulators," Ocean Engineering, **37**(2-3), pp. 218–227.

[18] Sun X., Chick J. P., and Bryden I. G., 2008, "Laboratory-scale simulation of energy extraction from tidal currents," Renewable Energy, **33**(6), pp. 1267–1274.

[19] Sun X., 2008, "Numerical and Experimental Investigation of Tidal Current Energy Extraction," University of Edinburgh.

[20] Nishino T., and Willden R. H. J., 2012, "Effects of 3-D channel blockage and turbulent wake mixing on the limit of power extraction by tidal turbines," International Journal of Heat and Fluid Flow, **37**, pp. 123–135.

[21] Consul C. A., Willden R. H. J., Mcintosh S. C., and A P. T. R. S., 2013, "Blockage effects on the hydrodynamic performance of a marine cross-flow turbine," Philosophical transactions. Series A, Mathematical, physical, and engineering sciencesransactions of the Royal Society, (January).

[22] Teymour A., and Mozafari J., 2010, "Numerical Modeling of Tidal Turbines : Methodology Development and Potential Physical Environmental Effects," University of Washington.

[23] Kundu, Pijush K. , Cohen I. M., 2007, Fluid Mechanics.

[24] Menter F. R., 1996, "A comparison of some recent eddy viscosity turbulence models," Journal of Fluids Engineering, **118**, p. 514.

[25] "Ansys Fluent 14.0 User's Guide, Chapter 29, Modeling Using the Solver, 2011."

[26] Tyler R. N., 2011, "Investigation into the Flow Control Potential of a Cross-Flow Hydrokinetic Turbine in a Main Canal of the Columbia River Basin Project," University of Washington.

[27] Kumar R., Virtual Blade Model Tutorial.

[28] Kim Y., and Park S., 2009, "Navier-Stokes Simulation of Unsteady Rotor- Airframe Interaction with Momentum Source Method," International Journal of Aeronautical & Space Sciences, **10**(2), pp. 125–133.

[29] Batten W. M. J., Bahaj a. S., Molland a. F., and Chaplin J. R., 2006, "Hydrodynamics of marine current turbines," Renewable Energy, **31**(2), pp. 249–256.

[30] Molland a F., Bahaj a S., Chaplin J. R., and Batten W. M. J., 2004, "Measurements and predictions of forces, pressures and cavitation on 2-D sections suitable for marine current turbines," Proceedings of the Institution of Mechanical Engineers, Part M: Journal of Engineering for the Maritime Environment, **218**(2), pp. 127–138.

[31] Grasso F., 2011, "Design and Optimization of Tidal turbine Airfoil," (July), pp. 27–30.

[32] "Photographs of different types of cavitation" [Online]. Available: http://cavity.ce.utexas.edu/kinnas/cavphotos.html.

[33] "Monthly Average Weather Data" [Online]. Available: http://www.weather.com/weather/wxclimatology/monthly/graph/98823.

[34] Sturm T. W., 2010, Open Channel Hydraulics, McGraw-Hill.

[35] Henderson F. ., 1966, Open Channel Flow.